Friedrich-Alexander-Universität
Faculty of Sciences

Master's Thesis
in Physics

Development of In-situ Calibration Routines and Long-term Monitoring for IceCube Upgrade mDOMs without Artificial Light Sources

Carolin Annika Klein

Supervisor: Prof. Dr. Claudio Kopper

Submission date: 16.12.2025

Abstract

The IceCube Neutrino Observatory has been detecting high-energy neutrinos since 2011. To enhance its sensitivity to lower-energy atmospheric neutrinos, seven strings equipped with newly developed optical modules and calibration devices will be deployed in the Antarctic summer 2025/26. A proper calibration for the photomultiplier tubes (PMTs) and electronics of the optical modules is required to ensure reliable data interpretation. In the scope of this thesis, in-situ calibration routines for multi-PMT Digital Optical Modules (mDOMs) included in the IceCube Upgrade are developed. In contrast to current approaches, these routines do not rely on artificial light sources. Thus, these routines can still be used in case of dysfunctional flasher LEDs. The PMT gain calibration is based on single photoelectron (SPE) charge spectra generated by dark noise in the PMT. Two different fit approaches are evaluated. The obtained calibration results are reproducible and typically deviate less than 5 % from the target gain. Thus, they fulfill the precision requirement defined in this thesis. Smaller systematic deviations between the fit approaches are observed as well as deviations between the dark noise and LED based calibrations. The accuracy of all investigated approaches used in this thesis, including the LED calibration, are to be evaluated in the future. Furthermore, two methods for the discriminator threshold calibration are developed and evaluated. A dark noise based approach achieves the target threshold with good agreement to LED measurements. A long-term monitoring routine using dark noise demonstrates that the gain drifts by less than 1.5 % and the threshold drifts up to 6.9 % over several weeks. Thus, the results of this thesis show that it is possible to calibrate both, gain and threshold without artificial light. Such approaches can also be used for in-situ gain and threshold monitoring during normal detector operating conditions.

Contents

1 Introduction

Humans have always been eager to learn about their environment and the basic laws of physics [1]. Even though science and research have evolved throughout the centuries, many fundamental questions remain unanswered. Questions regarding both the smallest and largest structures in the universe persist [2].

There are many different experiments with the purpose of answering such questions. One of them is the IceCube Neutrino Observatory located at the South Pole [2]. This experiment uses electrically neutral elementary particles, called neutrinos, as messenger particles to learn about both the neutrino itself and its production processes in the Universe. IceCube is an optical neutrino detector that uses a cubic kilometer of Antarctic ice as interaction and detection medium. Charged particles created as a result of neutrino interactions induce Cherenkov radiation in the medium, which is subsequently detected by an array of Digital Optical Modules (DOMs)

To enhance the sensitivity to lower neutrino energies, an extension of the existing IceCube detector, the IceCube Upgrade, will be deployed in the austral summer 2025/26 [3]. The Upgrade will consist of several different kinds of optical modules. One of them is the multi-PMT Digital Optical Module (mDOM) which is especially relevant for this thesis. In contrast to the IceCube DOM that contains only one large PMT, the mDOM comprises 24 smaller PMTs.

As for every other physics experiment, some electronics within the mDOM must be calibrated properly to enable the correct interpretation of the measurement results [4]. For the mDOMs, this includes the calibration of the gain of the photomultiplier and the pulse readout triggering threshold, referred to throughout this thesis as the discriminator threshold.

So far, dedicated LEDs included in the mDOMs are used for the calibration of the electronics during final acceptance testing [5]. This requires fully functioning calibration LEDs. To ensure that an mDOM can still be calibrated in the case of a flasher LED dysfunction, alternative calibration routines that do not rely on artificial light are desirable. In the scope of this thesis, calibration routines for gain and discriminator threshold using PMT dark noise are developed and tested for the mDOM. Furthermore, a discriminator threshold calibration routine using a test pulser is investigated. In addition, the long-term stability of the gain and the discriminator threshold is studied using dark noise. The goal is to help determine a reasonable calibration schedule as unnecessary re-calibrations should be avoided. Finally, such an approach can be used in-situ to verify the accuracy and stability of the current calibration settings. This is the first study of such calibration routines and long-term variations using a fully integrated mDOM.

2 Basic Concepts

In this chapter, the theoretical basics for this thesis are explained. This includes neutrino physics and astronomy, the Cherenkov effect and the functionality of photomultiplier tubes.

2.1 Neutrinos

Neutrinos are elementary particles and are part of the Standard Model of particle physics [6]. The existence of neutrinos was first postulated by Wolfgang Pauli in 1930 [6]. At this time, it was assumed that in β decay, a neutron is transformed into a proton producing a single electron. However, measurements of the energy distribution of the electron showed that this initial assumption was not justified. To ensure energy conservation, Pauli introduced an additional particle, the neutrino, changing the overall functional form of the β^- decay:

$$n \longrightarrow p + e^- + \bar{\nu}_e. \tag{2.1}$$

This is still valid as of today.

Due to this decay scheme, the neutrino has to have certain specific properties to not break any other conservation law [6]. For example, its mass must be small and it is required to not have an electrical charge. This lead Pauli to the assumption that it is impossible to detect such a particle.

Nevertheless as known today, the neutrino does interact via weak interaction and can therefore be detected indirectly using secondary particles [2]. Such interactions are described in Section 2.1.1. Additionally, it will be discussed that the absence of an electrical charge of the neutrino can also be an advantage in the framework of astroparticle physics (cf. Section 2.1.2).

In the Standard Model of particle physics, the mass of a neutrino is assumed to be zero. This assumption is still present, even though it was proven that the neutrino can indeed not be massless [7]. This is due to the observation of neutrino oscillations that will be described briefly in Section 2.1.3. In such an oscillation the neutrino can change its type, or flavor. In total, there are three different neutrino flavors: the electron, muon and tau neutrinos (ν_e, ν_μ, ν_τ). In addition, each neutrino has a corresponding anti-particle: ($\bar{\nu}_e$, $\bar{\nu}_\mu$, $\bar{\nu}_\tau$).

2.1.1 Neutrino Sources, Production and Interaction

In this section, the sources and production mechanisms for neutrinos are described as well as their interactions.

Neutrinos Sources and Production

There are different processes and sources in which neutrinos can be produced [7]. Depending on source and process, the energies of the produced neutrinos can vary and help to distinguish neutrinos of different origins. In Figure 2.1, the expected neutrino fluxes of different sources are shown.

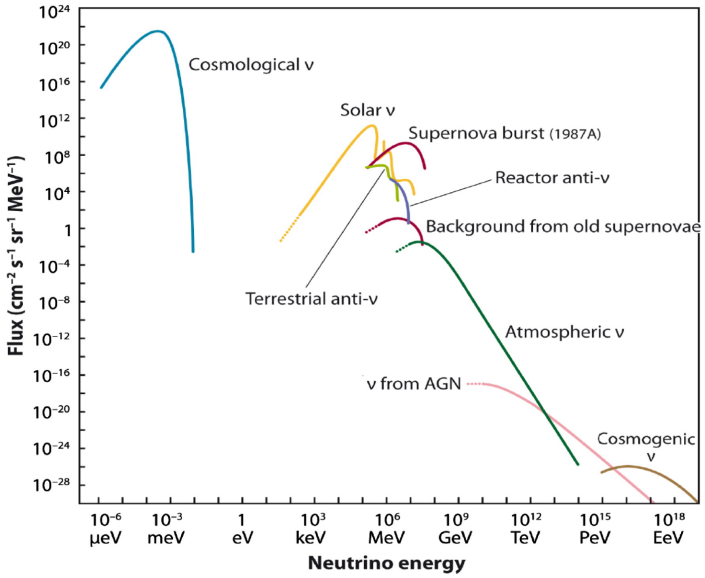

Figure 2.1: Overview of expected neutrino fluxes in different energy regimes of different sources. Figure taken from [7].

Energies, from 100 MeV up to several TeV, are reached for neutrinos produced in the atmosphere. In this scenario, neutrinos are generated as secondary particles when primary cosmic rays, especially protons, interact with the atoms of the atmosphere. Pions and kaons are created that subsequently decay, producing neutrinos [8]. The dominant decay channels for both particles are [9]:

$$\pi^{\pm} \longrightarrow \mu^{\pm} + \overset{(-)}{\nu}_{\mu} \tag{2.2}$$

$$K^{\pm} \longrightarrow \mu^{\pm} + \overset{(-)}{\nu}_{\mu} \tag{2.3}$$

The muons themselves then can decay again into neutrinos:

$$\mu^{\pm} \longrightarrow e^{\pm} + \overset{(-)}{\nu}_{e} + \overset{(-)}{\nu}_{\mu}. \tag{2.4}$$

A neutrino flux that mainly consists of (anti-) ν_μ and sub-dominantly of (anti-) ν_e is expected from the atmosphere [10]. The ratio of the neutrino flavors is energy dependent. At low energies, i.e., at the GeV scale, a flavor ratio of $\overset{(-)}{\nu}_{\mu} : \overset{(-)}{\nu}_{e} \approx 2:1$ is expected. However, the contribution of (anti-) ν_e decreases with increased energy as the muons produced in the atmosphere are more likely to reach the surface of the Earth before they decay. Furthermore,

the creation of (anti-) ν_τ is suppressed for low energies (GeV) due to the mass of the charmed mesons and the τ-lepton required to produce them [11].

Neutrinos produced in astrophysical objects such as active galactic nuclei (AGN) can be even more energetic with energies up to EeV [7]. These neutrinos are often generated by proton interactions. There are two potential main processes, but their relative contribution is still to be determined. Protons can for example interact with other protons in a target gas in the area in or around the astrophysical object. Furthermore, protons can also interact with a radiation (photon) field, forming a delta resonance that subsequently decays into pions. In either case, the resulting pions can then produce neutrinos as described before. Additionally, neutrinos can also be produced in free neutron decays. A goal of current neutrino detectors such as IceCube (cf. Section 3.1) is to determine the production mechanisms of neutrinos in astrophysical sources [12].

Neutrino Interactions

Neutrinos themselves only interact via weak interaction and have relatively low interaction cross sections [7]. In general, one can distinguish two types of neutrino interactions, charged current (CC) mediated by a charged W boson and neutral current (NC) interactions where an uncharged Z boson is involved. The different types of interactions in matter are shown in Figure 2.2.

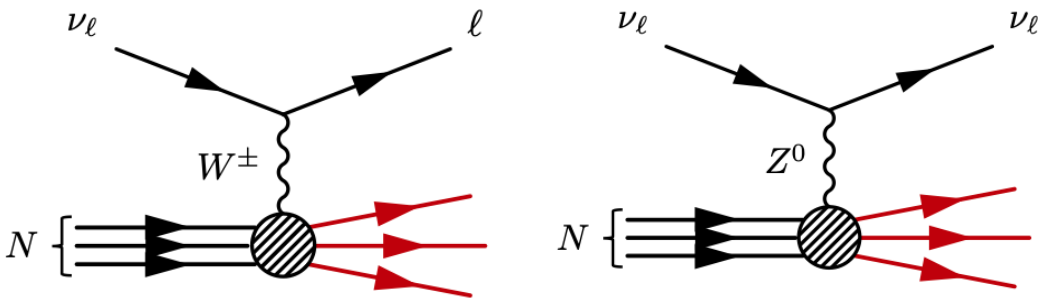

(a) CC interaction (b) NC interaction

Figure 2.2: Diagrams of different deep-inelastic neutrino interaction types in matter. Figure from [13].

In the energy range of interest to IceCube (cf. Section 3.1), neutrinos most often interact with individual quarks inside a nucleus through a process called deep-inelastic scattering [10]. In a CC interaction, the deep-inelastic scattering of an incoming neutrino leads to an outgoing charged lepton of the same flavor as the neutrino and a hadronic cascade [7]. In an NC interaction, both the incoming and the outgoing particles are neutrinos of the same flavor and a hadronic cascade is created.

2.1.2 Neutrino Astronomy

As described above, neutrinos can be produced in different astrophysical scenarios and their properties make them very interesting messenger particles for astronomy [12].

On the one hand, neutrinos are electrically neutral [14]. Therefore, they do not get deflected by magnetic fields on their way through the universe. Thus, the direction of their origin can be inferred back when the incident neutrino direction is observed. The good direction reconstruction possibilities are especially present for muon neutrinos interacting via a CC interaction. For high energies, the angle between the incoming neutrino and the outgoing muon is almost negligible. Additionally, the muon can travel long distances within the detection medium. Thus, the CC muon neutrino interaction is sometimes referred to as the 'golden channel' for neutrino astronomy, allowing to search for point sources.

In addition to the absence of electrical charge, neutrinos have an overall small interaction cross section [14]. Despite making it harder to detect neutrinos, this enables them to escape particularly dense areas where for example γ rays are absorbed. Thus, neutrinos enable the investigation of regions where γ rays cannot be used as messenger particles.

Furthermore, neutrinos are valuable particles for multi messenger astronomy [12]. For example, γ rays can be produced by a decay of a neutral pion ($\pi^0 \longrightarrow \gamma + \gamma$). However, from theoretical models it is likely that not only neutral pions are created but also equal amounts of charged pions. As described before, these charged pions then decay into muons and neutrinos. Therefore, there are models predicting that some γ ray sources are also good candidate neutrino sources. The additional measurement of neutrinos from such a source would help to understand the production mechanisms and local environment in this astrophysical object even better.

Neutrino astronomy is a relatively new branch of astronomy but important observations were possible using for example the IceCube Neutrino Observatory, which is explained in more detail in Section 3.1. For example in 2013, a high-energy astrophysical neutrino flux was discovered by IceCube [15]. Additionally, IceCube observed neutrinos from the galactic plane with a significance of $4.5\,\sigma$ (2023) [16].

2.1.3 Neutrino Oscillations

In the time around the year 1970, the Homestake experiment started its data acquisition to measure solar neutrinos [17]. These neutrinos were detected using the inverse β decay on chlorine atoms:

$$^{37}\mathrm{Cl} + \nu_e \longrightarrow {}^{37}\mathrm{Ar} + e^-. \tag{2.5}$$

The number of observed neutrino interactions was then compared to the expected number of neutrinos derived from the standard solar model. It turned out that only approximately 30 % of the predicted neutrinos were measured in the experiment. Following this result, at least three hypotheses were put forward. Some scientists questioned the results of the Homestake experiment, while some others suspected issues with the standard solar model. The third hypothesis was based on the phenomenon of neutrino oscillations described already in 1957 by B. Pontecorvo. In this scenario, the electron neutrinos oscillate into another neutrino

flavor and will therefore not be detected by inverse β decay and can explain the observed deficit. Later on, experiments such as Kamiokande confirmed the solar neutrino deficit making hypothesis number one unlikely. By detecting neutral current interactions of all flavors, the Sudbury Neutrino Observatory (SNO) experiment demonstrated that the results were indeed compatible with neutrino oscillations [18]. The observation of an atmospheric muon neutrino deficit helped to confirm the neutrino oscillation theory using an additional source and neutrino flavor [19]. With this, a massless neutrino as described in the standard model of particle physics was no longer feasible.

To explain the mechanism behind neutrino oscillations, eigenstates need to be considered [20]. On the one hand, the neutrino is produced and measured in its flavor eigenstate, i.e. it is observed either as a ν_e, ν_μ or ν_τ. On the other hand it propagates in its mass eigenstates ν_1, ν_2 or ν_3 that are different from the flavor eigenstates. The flavor eigenstates can be expressed as linear combinations of the mass eigenstates. In matrix notation, the linear combination is given by a matrix vector product:

$$\begin{pmatrix} \nu_\mathrm{e} \\ \nu_\mu \\ \nu_\tau \end{pmatrix} = \begin{pmatrix} U_\mathrm{e1} & U_\mathrm{e2} & U_\mathrm{e3} \\ U_{\mu 1} & U_{\mu 2} & U_{\mu 3} \\ U_{\tau 1} & U_{\tau 2} & U_{\tau 3} \end{pmatrix} \begin{pmatrix} \nu_1 \\ \nu_2 \\ \nu_3 \end{pmatrix} \tag{2.6}$$

Here, $U_{\alpha i}$ are the matrix elements describing the mixing between flavor state α and mass state i. This mixing matrix is also known as the Pontecorvo–Maki–Nakagawa–Sakata (PMNS) matrix [20].

This 3x3 matrix is assumed to be a unitary matrix [20]. This implies that the 3 neutrino flavors are considered to be a full base. This unitary matrix can be described by 4 independent and free parameters of which typically 3 are interpreted as weak mixing angles θ_{12}, θ_{13} and θ_{23}. In a common parametrization of the PMNS matrix, these angles are defined by 3 Euler angles of a rotation in 3D [20]. The last free parameter is a CP violating phase δ_{CP}. This can be written as:

$$U = \begin{pmatrix} c_{12}c_{13} & s_{12}c_{13} & s_{13}e^{-i\delta_\mathrm{CP}} \\ -s_{12}c_{23} - c_{12}s_{23}s_{13}e^{i\delta_\mathrm{CP}} & c_{12}c_{23} - s_{12}s_{23}s_{13}e^{i\delta_\mathrm{CP}} & s_{23}c_{13} \\ s_{12}s_{23} - c_{12}c_{23}s_{13}e^{i\delta_\mathrm{CP}} & -c_{12}s_{23} - s_{12}c_{23}s_{13}e^{i\delta_\mathrm{CP}} & c_{23}c_{13} \end{pmatrix} \tag{2.7}$$

Here, $c_{ij} = \cos\theta_{ij}$, respectively $s_{ij} = \sin\theta_{ij}$ [20].

The oscillation probability in vacuum $P(\nu_\alpha \to \nu_\beta)$ at a certain distance L from the initial starting point can be calculated [20]. This uses the inner product of the required final state $\langle\nu_\beta|$ and the time evolved state at position L $|\psi(L)\rangle$. The result depends on the entries of the PMNS matrix, i.e. on the respective mixing angles. Furthermore, this probability also depends on the distance L, the energy E and the squared mass difference Δm^2_{ij} of the mass eigenstates. The masses come into play when making use of the relativistic energy-momentum relation in the ultra relativistic limit, i.e. $p >> m$.

The investigation of neutrinos from different sources, i.e. with different initial flavors and energies are of great interest in the field of neutrino physics [20]. Experiments specializing

in the detection of neutrinos of different origins are sensitive to different mixing angles and mass splittings. Therefore, the mixing angles can be named after the respective neutrino origin. The angle θ_{12} is also referred to as 'solar mixing angle', θ_{23} is the 'atmospheric mixing angle' and θ_{13} can be interpreted as 'reactor mixing angle'.

There a still a lot of open questions in neutrino physics. For example, the octant of the atmospheric mixing angle is not yet determined [21]. The knowledge of the octant will improve the understanding of both neutrino compositions and the masses of neutrinos. Many properties regarding the neutrino masses are still unknown [22], [23]. The absolute neutrino mass is not accessible using neutrino oscillations and only upper limits can be estimated using high precision measurements of the energy spectrum of the β decay [22]. However, in certain cases, e.g. when matter effects come into play, it is possible to determine the sign of the mass differences. Using the Mikheyev–Smirnov–Wolfenstein (MSW) effect for solar neutrinos, it was determined that the mass of mass eigenstate 1 is lower than that of mass eigenstate 2 [23]. However, it is still unknown if mass eigenstate 3 is heavier (normal mass ordering) or lighter (inverted mass ordering) than the other mass eigenstates [20]. Both ordering possibilities with the corresponding flavor compositions are shown in Figure 2.3. It may be possible to determine the mass ordering using atmospheric neutrino oscillations in the Earth with future neutrino experiments like the IceCube Upgrade [23].

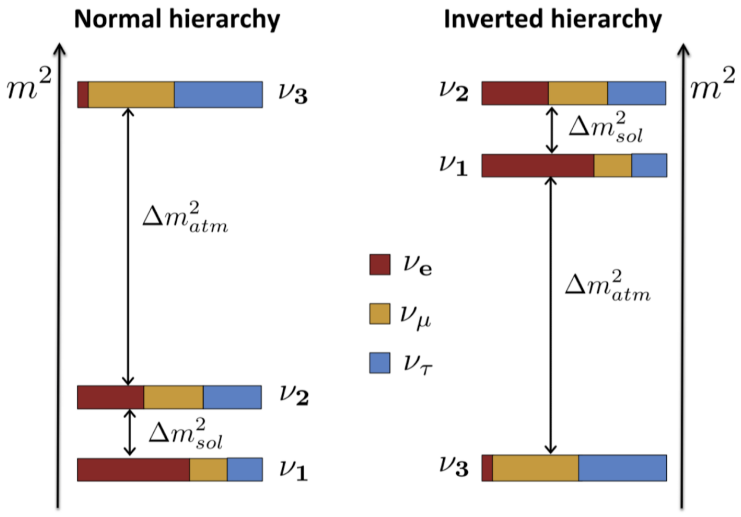

Figure 2.3: Sketch of neutrino mass ordering possibilities. The respective flavor composition is shown as color scheme. Figure from [24].

2.2 Cherenkov Effect

As described in Section 2.1, neutrinos cannot be detected directly but by secondary particles produced in their interactions. The Cherenkov effect described in this section is a common tool for indirect neutrino detection [25].

In the case that a non-relativistic charged particle moves through a dielectric medium, the atoms in the medium are temporarily polarized symmetrically around the particle [25].

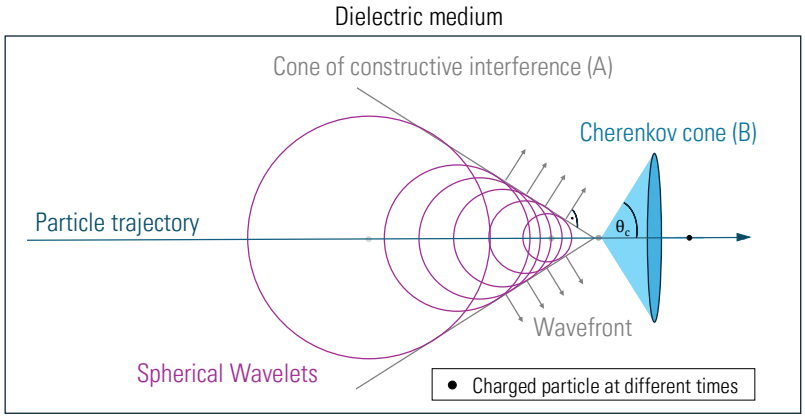

Figure 2.4: Schematic of the Cherenkov effect. Figure adapted from [26].

Due to deconstructive interference of the dipole radiation, no overall radiation is emitted. However, when a charged particle moves faster than the local speed of light in the medium, an effect known as Cherenkov radiation can be observed. A schematic of this effect is shown in Figure 2.4. The information for the polarization of the medium travels with the local speed of light. As the charged particle travels faster than this, an excess temporary polarization of the medium is left behind the particle. The spherical wavelets produced by the polarization interfere constructively on a cone, denoted by (A) in Figure 2.4, generating a conical wavefront. Electromagnetic radiation is therefore emitted along the surface of a second cone, the Cherenkov cone, perpendicular to the cone of constructive interference. The opening angle of the Cherenkov cone, the Cherenkov angle θ_c, can be derived geometrically and is given by:

$$\cos\theta_c = \frac{1}{\beta \cdot n}. \tag{2.8}$$

In this relation, n is the refractive index of the medium and $\beta = \frac{v}{c}$ with particle velocity v and speed of light c [25].

The photon yield of the Cherenkov radiation can be calculated using the Frank-Tamm formula [27]. For a relativistic charged particle traversing media such as water or ice, approximately 250 photons per meter are emitted within a wavelength range of 300 to 500 nm. Therefore, the emission ranges from optical blue light to ultraviolet light. Such photons can be detected using photomultiplier tubes as described in the following.

2.3 Photomultiplier Tubes

An important component for optical neutrino detection are photomultiplier tubes (PMTs). To accurately understand and interpret the measured signals, the properties of PMTs must be quantified in detail. This section provides an overview of the basic working principle, as well as the dark rates and typical photoelectron charge spectra.

2.3.1 Working Principle

The general idea of a PMT is to convert a faint light signal into an measurable electrical signal [28]. A photomultiplier consists of different parts, mainly a photocathode, several dynodes and an anode accommodated inside an evacuated glass tube. A successively larger accelerating voltage is applied between the dynodes [28]. A corresponding schematic is shown in Figure 2.5.

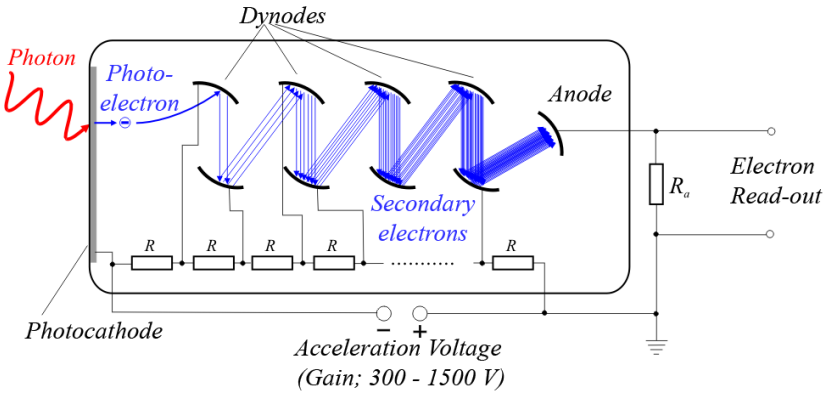

Figure 2.5: Schematic of a photomultiplier tube. An incident photon is converted to a photoelectron at the photocathode and is subsequently amplified. The voltage divider for the 8 dynodes is included as well as a readout using a resistor. Figure from [29].

When a photon with an energy larger than the band gap of the material hits the photocathode, the photon can be absorbed and an electron is released from the material, which is known as the external photoelectric effect [28]. This emitted electron is then called a photoelectron. Due to the applied voltage, the electron is accelerated to the first dynode. There, further electrons are released from the material by ionization and excitation processes. By the use of a voltage divider, the voltage to the next dynode is always higher than the previous one. Therefore, it is ensured that the electrons are indeed accelerated further to the following dynode. Through this repeated acceleration of a growing number of electrons, an electron avalanche is created. After several dynodes, the electron avalanche can then be converted into an measurable current at the anode. A voltage signal is typically readout in the end using a resistor.

The amplification factor g, also referred to as gain, of a photomultiplier tube with N dynodes can be described mathematically using two different coefficients [30]:

$$g(V) = \prod_{i=1}^{N} d_i c_i. \tag{2.9}$$

The mean number of electrons released at dynode stage i is given by the secondary emission coefficient d_i. This number depends on the energy of the incident electron and therefore depends on the applied high voltage V accelerating the electrons. However, due to the geometry of the PMT itself, not all of these secondary electrons might reach the next dynode. Therefore, an additional factor must be considered which is the inter-dynode collection efficiency c_i. With these factors and the number of dynodes in the PMT, the

average number of electrons at the anode per photoelectron can be calculated. This gain is thus high voltage dependent.

The shape of a PMT signal depends on several properties such as the inner structure of the specific PMT and the readout circuit [31]. A typical PMT signal, without further pulse shaping, has a steep leading edge, often referred to as rising edge and a shallower trailing edge, also called falling edge. The terms of rising and falling edge are derived from a PMT pulse with positive amplitude. However, in many circuits, the outgoing PMT pulse has a negative amplitude and the leading edge is termed rising edge nonetheless. This is the case for the pulses analyzed in this thesis.

The characteristic shape of the PMT pulses is a superposition of different effects. The PMT can be interpreted as a current generator in parallel with both a resistor and a capacitor [32]. This includes the charging characteristics of the dynodes [33]. Another effect contributing to the pulse shape is the angular and energy distribution of the secondary electrons [34]. The steep leading edge of the signal is created by electrons with maximum energy and an ideal path inside the PMT, while electrons with less energy, respectively longer paths inside the PMT contribute to the shallower trailing edge of the signal. The overall observed signal at the anode is then a convolution of the signals at the individual dynodes and thus becomes Gaussian for an infinite number of dynodes. However, the raw PMT signal is usually further processed. The resulting pulse shape can be characterized using its rise and fall time, defined according to the rising and falling edge, and the total length of the signal. Rise and fall times are defined by the time the signal needs to rise, respectively fall, between 10 % and 90 % of the positive pulse amplitude.

In most experiments that employ PMTs, the time resolution plays an important role [31]. For example in IceCube, the timing of a signal is crucial to determine the angle under which a charged particle crossed the detector. The time between the incident light and the signal arrival at the output of the PMT is called transit time (TT). The variation of it is called Transit Time Spread (TTS) and can be interpreted as the single photon time resolution of the PMT.

In an ideal case, every incident photon will lead to the emission of a photoelectron. However, in a real system the percentage of photons producing photoelectrons depends on the wavelength of the incident photon, the material of the photocathode and the optical properties of the PMT entrance window [28]. The quantity describing this efficiency is called quantum efficiency (QE). The quantum efficiency of the PMTs used in this thesis is given by $QE_{375} = (27.5 \pm 1.1)\,\%$ at a wavelength of $375\,\mathrm{nm}$ and $QE_{505} = (18.1 \pm 1.3)\,\%$ at a wavelength of $505\,\mathrm{nm}$ [35].

2.3.2 Dark Rate

When a PMT is shielded from external light sources, i.e. placed in a dark room, it will still produce measurable signals [28]. This phenomenon is called dark noise which is a collective name for several independent processes.

Dark Noise from Photocathode and Dynodes

The most important source of dark noise at room temperature is thermionic emission of electrons from the photocathode [28]. This emission is possible when the thermal energy of the electron is larger than the work function of the cathode material. The work function describes the energy that must be exceeded by an electron to be able to escape from the material [36]. The released electron is then treated just as a real photoelectron and therefore shows up as such at the PMT output. In principle, thermionic emission from the dynodes is possible as well. As this effect depends on the thermal energy of the electrons in the materials, thermionic emission is strongly temperature dependent and is therefore almost negligible for PMTs operated at low temperatures.

When a photomultiplier tube is operated at a high gain, background noise can be produced by field emission [28]. That means that electrons are released from the dynode material by the applied strong electric field. Such high gain settings should be avoided to not reduce the life time of the PMT.

Dark Noise from PMT Glass and Surrounding Materials

Important sources of dark noise at lower temperatures are radioactive decays within the glass of the PMT itself and surrounding materials [28]. In this thesis, the PMTs are housed in a pressure resistant vessel that consists of borosilicate glass. Sources of radioactive decays in such glasses, i.e., in the PMT window and the pressure vessel, are $^{40}\mathrm{K}$ as well as elements from the decay chains of $^{238}\mathrm{U}$, $^{235}\mathrm{U}$ and $^{232}\mathrm{Th}$ [37]. $^{40}\mathrm{K}$ for example is a naturally occurring radioactive isotope which has an abundance of 0.0117 % and a half-life of $1.27 \cdot 10^9$ years [38]. The full corresponding decay scheme of $^{40}\mathrm{K}$ is shown in Figure 2.6. The dominant decay channel is the β^- decay, transforming the unstable $^{40}\mathrm{K}$ into stable $^{40}\mathrm{Ca}$ [39]. The electron created in this decay has enough energy to generate photons via the Cherenkov effect in the glass of the PMT. A corresponding calculation is provided in Appendix A. In 11 % of the decays, electron capture (EC) occurs. This is related to the β decay. Instead of a neutron decaying under the emission of an electron, an electron of the atom is used to transform a proton into a neutron. As the now open space in the atom is successively filled by electrons from the shells above, the released energy is emitted as X-rays.

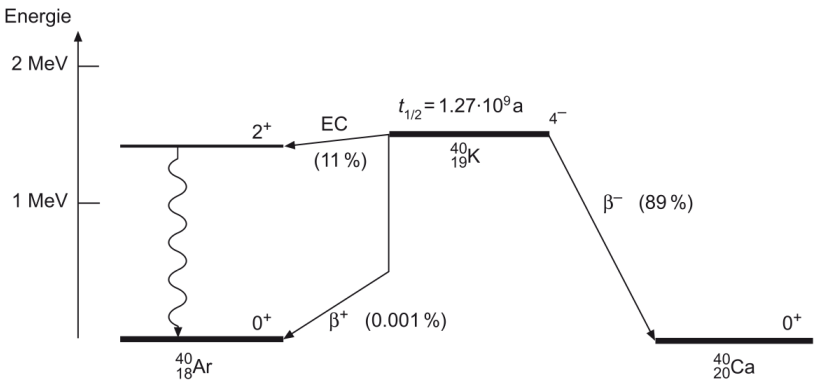

Figure 2.6: Decay scheme of $^{40}\mathrm{K}$. Electron capture is denoted by EC. Figure from [38].

In certain materials, the absorption of energy from ionizing radiation can lead to the emission of characteristic, visible, light in the de-excitation process of an atom [25]. The general term of such an emission process is luminescence, while it is typically referred to as scintillation when the excitation is caused by ionizing radiation. The production of scintillation light is temperature dependent. At higher temperatures, the de-excitation of the atoms via fully non-radiative processes is possible, reducing the amount of observed photons [37]. The properties of scintillation in borosilicate glass were investigated in more detail in [40], [41] and [37].

The photons generated either by Cherenkov radiation or more likely by scintillation can then be detected by the PMT [37]. Backgrounds induced by radioactive decays and thermionic emission are especially relevant for this thesis.

Additionally, muons as part of the secondary cosmic radiation can also produce Cherenkov photons in the PMT glass and therefore induce background noise [28].

2.3.3 Photoelectron Charge Spectrum

Before a photomultiplier tube can be used effectively for single photon detection, it needs to be calibrated [31]. For this purpose, typically a faint external light source is used. The dim light source, e.g., a light emitting diode (LED), is operated in a pulsed mode, releasing discrete light pulses. The PMT readout is triggered in coincidence with the released light pulse. Then the charge observed in the PMT signal is calculated by integrating over the signal in time and considering the impedance of the readout electronics. This is explained in more detail in Section 4.2.2. From these individual signals, a charge spectrum, termed the single photoelectron (SPE) charge spectrum, is built waveform by waveform (cf. Figure 2.7). As the photomultiplier has only a certain efficiency, not every waveform will contain a reasonable signal, thus some will only record the baseline of the PMT. These events form a characteristic peak around zero charge in the SPE spectrum called the pedestal.

Another distinct feature in the SPE spectrum is the SPE peak. It contains real events that were induced by a single photoelectron. The width of this peak is a measure for the total electron yield throughout the amplification process, and therefore, the resolution of a single photoelectron. The gain g can be derived directly from the SPE peak position μ_{SPE}:

$$g = \frac{\mu_{\mathrm{SPE}}}{e} \tag{2.10}$$

with elementary charge e.

When several photons arrive at the photocathode simultaneously and more than one photoelectron is created, the resulting events will then be part of the multi-photoelectron contribution [31].

A schematic representation of such an SPE charge spectrum and its individual components as well as the corresponding charge acquisition is shown in Figure 2.7.

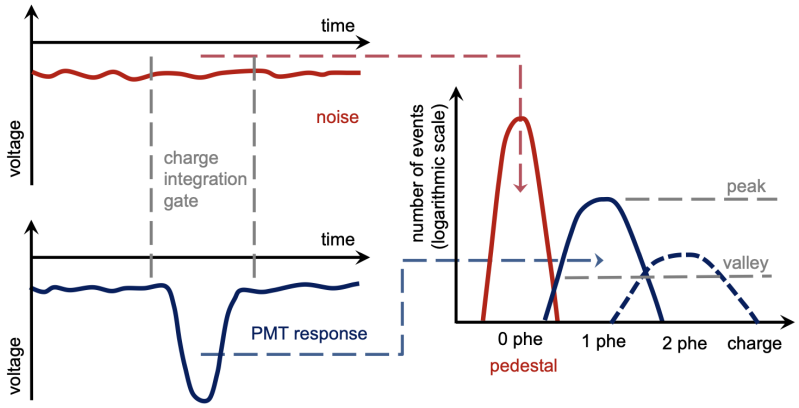

Figure 2.7: Charge acquisition (left) and individual components adding up to a full SPE charge spectrum (right). Waveforms that only contain noise (top left) contribute to the pedestal of the SPE charge spectrum (right). Waveforms with actual signals (bottom left) contribute to the SPE or higher PE peak. Figure from [31].

The ideal PMT response $S_{ideal}(q)$ to signals with charge q from a low intensity light source can be described mathematically. The calculation explained here follows the reasoning given in [42]. The mean number of photons arriving at the photocathode, m, follows a Poisson distribution. The probability P, to create a certain number of photoelectrons at the photocathode, n, is again described by a Poisson distribution considering the quantum efficiency QE of the PMT:

$$P(n, m \cdot QE) = \frac{(m \cdot QE)^n \cdot e^{-m \cdot QE}}{n!}. \tag{2.11}$$

In the ideal case, the pedestal is a delta function at zero charge $\delta(q)$ and the SPE peak of the spectrum can be described by a Gaussian distribution G_1:

$$G_1 = \frac{1}{\sigma_1 \sqrt{2\pi}} \exp\left(-\frac{(q - Q_1)^2}{2\sigma_1^2}\right). \tag{2.12}$$

Here, Q_1 is the position of the SPE peak and σ_1 is the width, i.e. the standard deviation of the SPE peak.

A higher nPE contribution G_n can then be expressed as convolution of n single-photoelectron Gaussian distributions assuming that the n photoelectrons and their subsequent amplification is independent:

$$G_n = \frac{1}{\sigma_1 \sqrt{2\pi n}} \exp\left(-\frac{(q - Q_1 n)^2}{2n\sigma_1^2}\right). \tag{2.13}$$

The overall ideal PMT response is then given by the convolution of Equation 2.11 and the convoluted Gaussian distributions $G(q)$:

$$\begin{aligned} S_{ideal}(q) &= P(n, m \cdot QE) * G(q) = \\ &= \delta(q) + \sum_{n=1}^{\infty} \frac{(m \cdot QE)^n e^{-m \cdot QE)}}{n!} \frac{1}{\sigma_1 \sqrt{2\pi n}} \exp\left(-\frac{(q - nQ_1)^2}{2n\sigma_1^2}\right). \end{aligned} \tag{2.14}$$

In a real PMT, background noise must also be considered [42]. The pedestal in a real photomultiplier tube cannot be described as a delta function, since the baseline of the PMT contains noise that integrates to a non-zero charge. In practice, therefore, the pedestal is better described as a zero-centered Gaussian with a standard deviation that characterizes the PMT baseline fluctuations. Additionally, some electrons might be poorly amplified within the PMT, for example when they miss the first dynode. Following [42], the poorly amplified electron contribution are reasonably described by an exponential function. Possible improvements to the modeling of this contribution are still under investigation [43].

The overall real PMT response function is given again by a convolution of the ideal PMT response with the background distribution [42]. This is a complex model that profits from further simplifications when used for fitting. The actual SPE models that are used in this thesis are described in Section 5.1.2.

An SPE like spectrum can also be created using dark noise instead of a low intensity light source [44]. This is especially important for this thesis as dark noise is used as calibration basis. In the case of dark noise generated spectra, the most prominent features, such as the SPE peak and the pedestal, remain. However, especially at low temperatures, when thermionic emission is suppressed, scintillation and Cherenkov radiation from radioactive decays play a more important role. Radioactive decays produce not only SPE like signals but also signals containing multiple photoelectrons. Thus, a discernible multiple PE contribution in the SPE spectrum is expected. In [44], it was demonstrated that a dark noise can be used for calibration purposes at room temperature when the PMT is operated at the recommended high voltage. This work further develops such a method in order to refine and monitor the calibration of PMTs specifically used in the IceCube Upgrade at lower temperatures.

3 Optical Detection of Neutrinos

In this section, the design and operating principles of the IceCube Neutrino Observatory will be discussed. In addition, the IceCube Upgrade will be described with a main focus on the multi-PMT digital optical module (mDOM).

3.1 The IceCube Neutrino Observatory

The IceCube Neutrino Observatory is an experiment dedicated to investigate the origin of astrophysical neutrinos and neutrino properties [45]. It is located at the Geographic South Pole and uses the Cherenkov effect (cf. Section 2.2) to detect neutrinos indirectly. Thus, it is an optical neutrino detector. The construction of this detector was finished in 2011.

The natural ice at the South Pole is used as detection medium in IceCube [2]. The large ice volumes and the corresponding high pressure in the deep ice ensure good optical properties. For example, the absorption length in the ice exceeds 100 m for wavelengths around 400 nm [46].

The detection of the Cherenkov light in IceCube is carried out by Digital Optical Modules referred to as DOMs [45]. The main part of the DOMs is a 10 inch downward facing

photomultiplier tube (PMT). The DOM furthermore contains readout electronics as well as a flasher LED board for calibration purposes. The PMT and all electronics are enclosed by a glass pressure vessel. A picture of a DOM is shown in Figure 3.1.

Figure 3.1: Picture of a DOM used in IceCube. The PMT in the lower hemisphere faces downward while the electronics are located in the upper hemisphere [47].

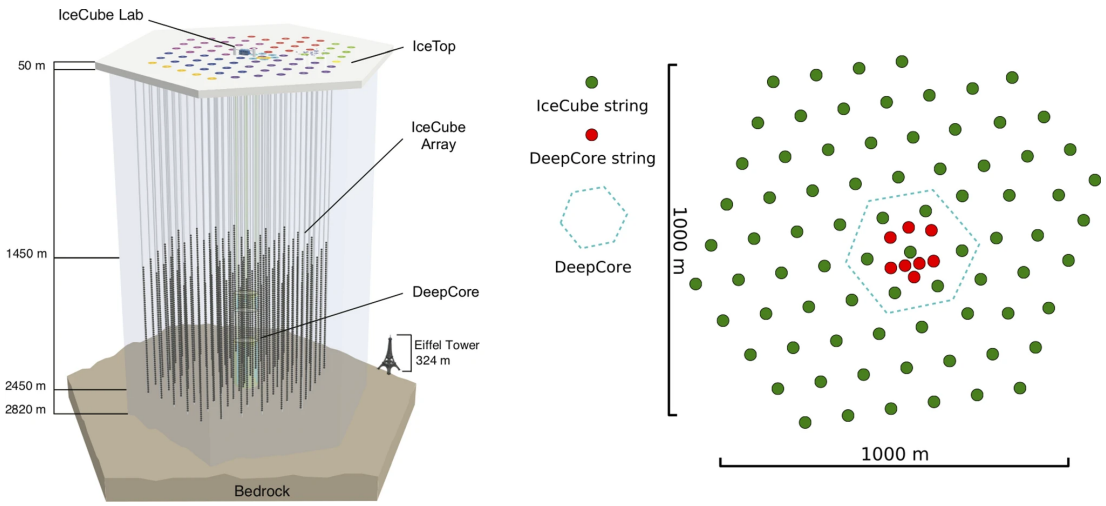

Figure 3.2: Left: General setup of the IceCube detector including the in-ice component with DeepCore and the surface detector IceTop. Right: Footprint of the in-ice strings. Figure from [2].

The whole in-ice component of the IceCube detector comprises a total of 5160 DOMs in an instrumented volume of approximately 1 km^3 [45]. The DOMs are distributed across 86

strings, i.e. each string holds 60 DOMs. The strings are arranged in a hexagonal pattern. A schematic of the IceCube detector is shown in Figure 3.2. The modules are located at depths between 1450 meters and 2450 meters ensuring good ice quality. Most strings have horizontal spacings of 125 meters and the DOMs are positioned with a vertical distance of 17 m, making the setup sensitive to neutrinos with energies above 100 GeV. However, the inner part of the detector consisting of 8 strings is more densely instrumented with only 7 m of vertical spacing and approximately 70 m between the strings. This part of the detector is referred to as DeepCore. This is used to study neutrino properties, such as oscillation properties (cf. Section 2.1.3) with high precision and search for low mass WIMP dark matter [48].

In addition to the in-ice component, the IceCube experiment also includes a surface detector called IceTop [49]. Tanks containing two DOMs each are located above the corresponding IceCube strings. These stations are used to characterize the cosmic ray spectrum and composition, and as a veto for IceCube and DeepCore [49].

3.2 The IceCube Upgrade

The IceCube Upgrade is an extension to the existing IceCube Neutrino Observatory [4]. The deployment is scheduled for the austral summer 2025/26.

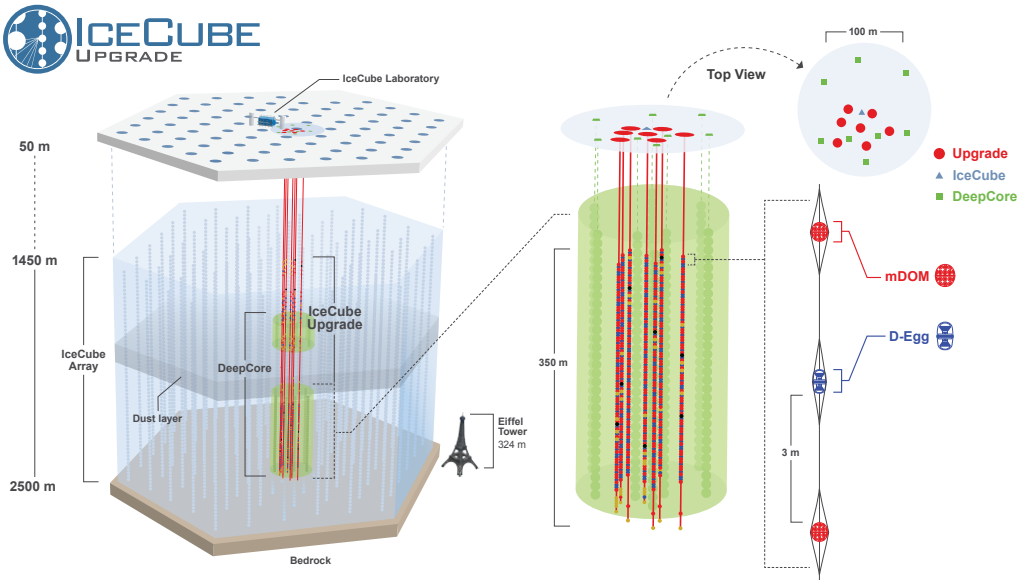

Figure 3.3: Left: Schematic of the IceCube Upgrade embedded in the IceCube experiment. Right: Layout of the 7 Upgrade strings with a closer view of the footprint and module arrangement within one string. Figure from [50].

3.2.1 Setup

The Upgrade will consist of 7 additional strings positioned in the area of the DeepCore detector, densely equipped with newly developed optical sensors, as well as new calibration

devices [3]. A sketch of the new IceCube footprint including the Upgrade strings is shown in Figure 3.3. The most abundant optical sensors will be Multi-PMT Digital Optical Modules (mDOMs) with 402 modules and Dual optical sensors in an Ellipsoid Glass for Gen2 (D-eggs) with 277 modules. Further types of new optical modules will be included in the setup to pave the way for the future IceCube Gen2 detector. The mDOM is especially important for this thesis and is therefore described in Section 3.3 in more detail.

Modules will be deployed in depths between approximately 1400 and 2600 m [3]. Most modules will be located between 2150 to 2425 m in the "physics region" with the best ice quality. Here, modules will have a vertical separation of 3 m. The modules deployed above and below this will mainly be used to investigate the optical and acoustic properties of ice across the entire depth range of interest for the existing IceCube detector.

3.2.2 Scientific Goals

The IceCube Upgrade will improve the knowledge about the antarctic ice using new calibration devices [3]. This will reduce systematic uncertainties in IceCube analyses. Additionally, due to the dense instrumentation with highly efficient optical modules, the sensitivity to neutrinos with energies down to 1 GeV is increased. This allows to investigate neutrino oscillations in more detail, including high-precision tau neutrino appearance and the study of PMNS matrix unitarity [3].

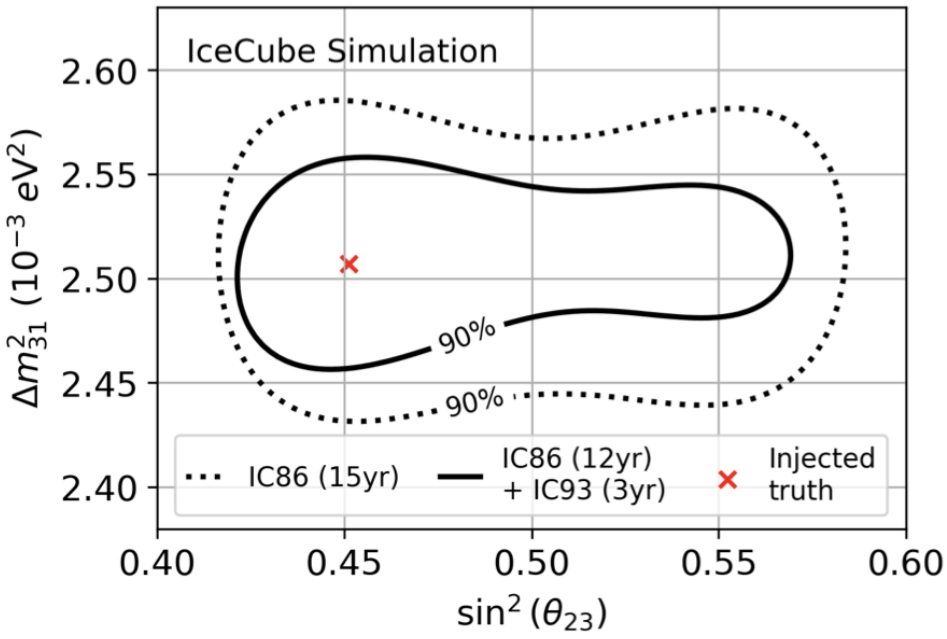

Figure 3.4: Sensitivity contours (90 % confidence level) for the current IceCube configuration and the future configuration including the Upgrade strings. A livetime of 3 years is considered for the Upgrade strings. Figure from [51].

An example for the capability of the IceCube Upgrade determining the mass difference

Δm_{23} and the mixing angle θ_{23} is shown in Figure 3.4. This includes the 90 % confidence level contours for the current IceCube configuration with a livetime of 15 years and the configuration including the IceCube Upgrade for 3 years. An improvement in sensitivity by 20-30 % can be expected for these oscillation parameters [51]. However, to achieve this improvement, a good energy and direction reconstruction is required. This is only possible if the optical modules are calibrated properly. Therefore, this thesis focuses on the development of in-situ calibration routines and long-term monitoring of crucial parameters for the mDOM described in Section 3.3.

3.3 The IceCube Upgrade Multi-PMT Digital Optical Module

Most relevant for this thesis is the multi-PMT digital optical module (mDOM). An "exploded" view of an mDOM as well as a picture of an mDOM are shown in Figure 3.5.

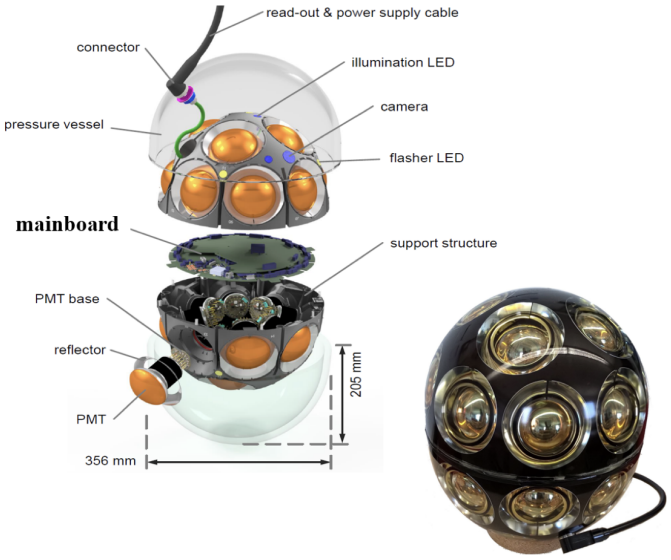

Figure 3.5: Schematic view of mDOM components (left) and picture of an actual mDOM (bottom right). Figure from [52].

This module contains 24 3-inch PMTs with their own active bases explained in Section 3.3.1 [52]. These PMTs are referred to as channels, where odd channel numbers are located in the lower hemisphere and channels with even numbers are positioned in the upper hemisphere. A total of 10 flasher LEDs are included in the mDOM for calibration purposes. Additionally, 3 cameras are included to study the ice in direct proximity to the mDOMs. Furthermore, several sensors such as temperature and pressure sensors are incorporated to monitor the operational environment inside the module. The arrangement and the relative positions of the channels, LEDs and Cameras are shown in Figure 3.6. The mainboard of the mDOM is located between the hemispheres and all electronics are surrounded by a Vitrovex glass pressure vessel [52].

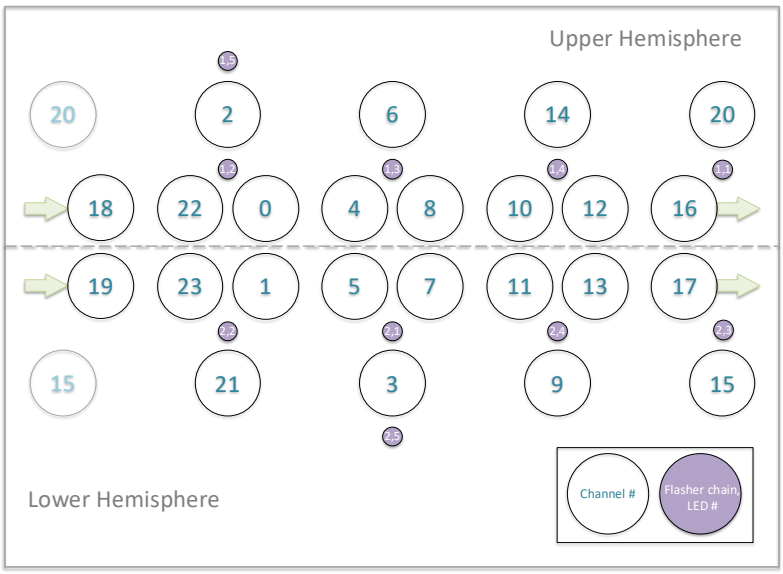

Figure 3.6: 2D projected schematic of the mDOM channel and LED arrangement. Figure adapted from [53].

3.3.1 PMT Base

The PMT base supplies the PMT with the required high voltage (HV). Due to a low-power budget per module at the South Pole, the mDOM PMTs use an active voltage divider approach [54]. More specifically, they use a Cockcroft-Walton (CW) circuit. A schematic of a CW circuit is shown in Figure 3.7. In this multiplier, a single stage consists of two diodes with opposite biases and two capacitors. The amplitude of the input alternating current (AC) peak-to-peak voltage V_{pp} is doubled at each stage. For a multiplier with N stages, the output voltage is given by $V_{\text{output}} = 2 \cdot N \cdot V_{\text{pp}}$. Thus, the potential can only be increased in increments of the input voltage amplitude [31].

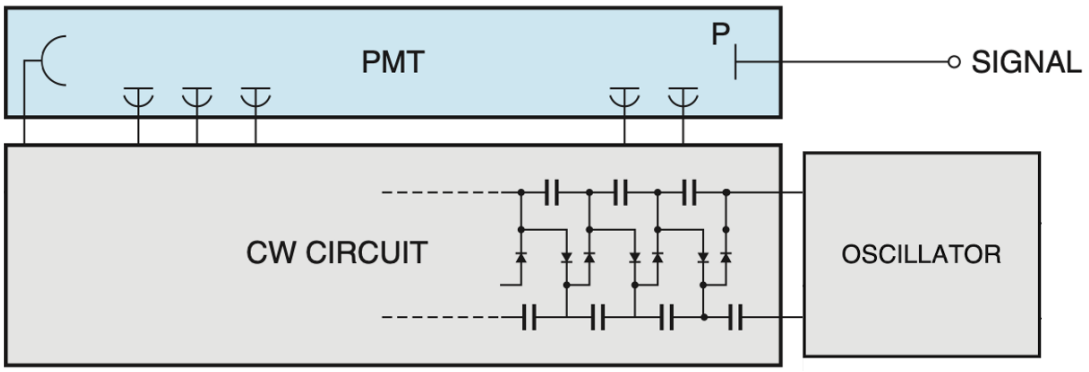

Figure 3.7: Schematic of a Cockcroft-Walton circuit used as PMT base. Figure adapted from [28].

In the mDOM, a microcontroller is used to control a rectangular signal generated by a rectangle wave driver [55]. This signal is transformed into a sine wave using LC resonators. This wave is then fed into a 13-stage Cockcroft-Walton multiplier with ratios of 1:1:1:1:1:1:1:1:1:1:3 starting at the anode. The generated direct current (DC) voltage is filtered by an RC filter before it is applied to the dynodes. The voltage is monitored at the first stage of the voltage divider, i.e. at dynode stage 10. A corresponding block diagram is shown in Figure 3.8.

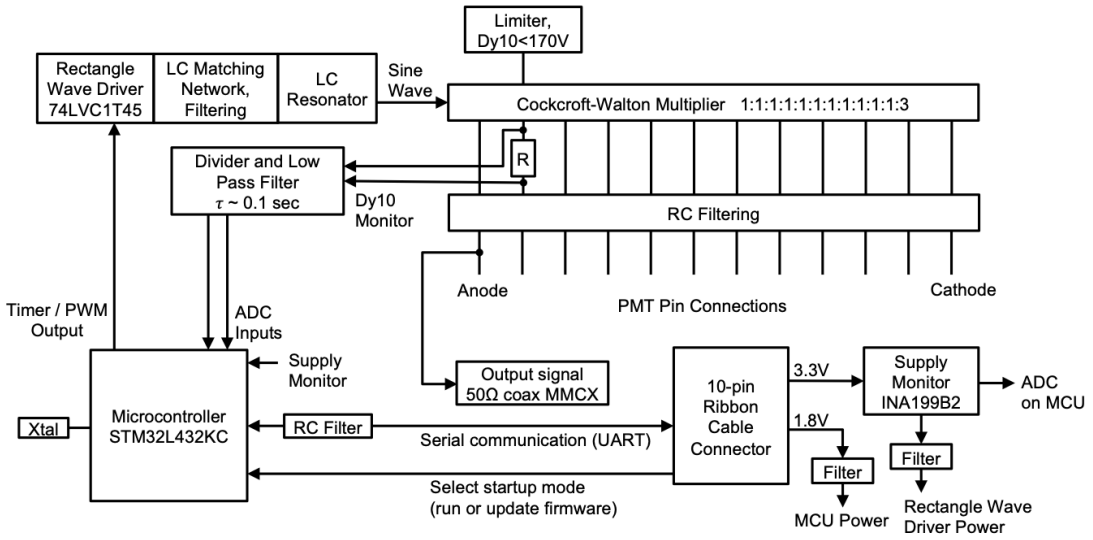

Figure 3.8: Schematic of the mDOM PMT base. Main parts are the microcontroller controlling the input power and the 13-stage Cockcroft-Walton multiplier. Figure from [54].

3.3.2 Analog Front-end

The raw PMT signals are directly digitized and processed within an mDOM via the analog front-end (AFE) circuit [52]. A block diagram of the AFE for one channel is shown in Figure 3.9.

The raw PMT signal follows two signal paths. On one path the signal is fed into a discriminator. In Figure 3.9, this discriminator is denoted by "Comp." as it is a simple comparator[1]. This comparator, as the name suggests, compares the incoming signal to a set reference voltage. This reference voltage is set using a Digital-to-Analog Converter (DAC). The discriminator signal in the mDOM is sampled with a sampling rate of 960 MHz.

At the second signal path, the raw PMT signal is introduced into a pulse shaping circuit. First, the signal is amplified by a preamplifier. Then, signals with a high frequency are attenuated by a low pass filter. The resulting signal is then again amplified before it is readout by a 120 MHz 12-bit Analog-to-Digital Converter (ADC). Its baseline is set by another DAC.

[1] Data Sheet. Accessed: 04.11.2025.

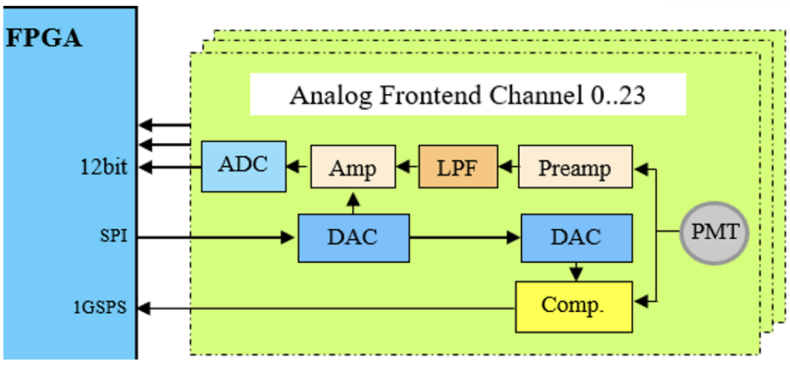

Figure 3.9: Schematic of an AFE of an individual channel. The raw PMT signal follows two distinct signal paths to the FPGA. The signal is processed and readout in the upper signal path, while it is compared to a reference voltage on the lower signal path. Figure from [52].

Additionally, each channel includes a front-end test pulser which is not depicted in Figure 3.9 [56]. The idea of the pulser is to verify the overall functionality of the front-end circuit [57]. The pulser is a capacitor with capacity of 2.2 pF. It can be charged by a front end pulser DAC allowing to set different pulse heights. The Field Programmable Gate Array (FPGA) can then give the signal to discharge the capacitor over the front-end impedance of approximately $75\,\Omega$. This signal bypasses the PMT signal and is processed as described above.

3.3.3 Final Acceptance Testing

Each mDOM that will be deployed in the IceCube Upgrade had to undergo extensive testing, called final acceptance testing (FAT), to ensure the functionality of all comprised components [4]. These tests included the calibration of both gain and discriminator threshold as well the monitoring of such at different temperatures. The methods used for the tests were therefore designed to investigate the quality of the produced mDOMs more than to achieve an ideal in-situ calibration of the quantities.

A large part of the testing was done within the Dark Freezer Lab (DFL) over a period of three weeks [4]. During this time, the temperature of the DFL was changed multiple times between -40°C and +20°C to model the conditions until the deployment of the modules. These temperature changes allowed for monitoring of the calibrated values for a maximum of 5 to 10 days [58]. Between the intended temperature changes, temperature variations of several degrees were observed. For a more precise monitoring, a stable measurement environment is required.

In the framework of this thesis, in-situ calibration and long-term monitoring routines without artificial light sources were developed based on the general idea of the FAT tests. Thus, a goal was to improve the precision of the calibration approaches.

4 Experimental Setup and General Methods

In this section, the experimental setup used in this thesis is described. In addition, general methods used in almost all calibration routines developed in this thesis are explained.

4.1 Experimental Setup

Within the scope of this thesis, experiments were carried out at two different sites with two different mDOMs. One site was located in Erlangen at the Erlangen Centre for Astroparticle Physics (ECAP) whereas the other site was located in Zeuthen at the Deutsches Elektronen-Synchrotron (DESY).

In Erlangen, experiments were performed at room temperature only. A block diagram for the experimental setup in Erlangen is shown in Figure 4.1. The mDOM used for the measurements is mDOM_D115_v1[1] and was housed in its transport box. This is a cardboard box with a hole that can be used as both a handle for lifting or, in the case of this setup, as a cable feedthrough. The mDOM was connected to a computer using a MiniFieldhub. This device enables communication between the connected modules and a computer via a wire pair [59]. The MiniFieldhub also acts as voltage supply for the mDOM.

The setup was placed in a room that is specifically designed for light sensitive measurements: there are no windows and the walls, the ceiling, the floor and the door are either black by production or painted black. The room is equipped with an traffic light interlock system, to avoid that the door is opened during measurements. All artificial and unwanted light sources, e.g. the light emitting buttons of the interlock system, were covered with tape. To ensure that potentially overlooked light sources do not interfere with light sensitive measurements, the transport box of the mDOM was placed underneath a table and covered with some black blankets. Additionally, the room was also used for development and testing of a device designed to perform ice stratigraphy measurements during the deployment of the IceCube Upgrade. This device is called LOMLogger and uses a laser which was tested in the same dark room. To ensure that the laser was turned off during light sensitive mDOM measurements, two chatbots[2] were configured to coordinate remote testing with either of the setups [60]. Pictures of the setup in Erlangen are shown in Figure 4.2.

In Zeuthen, the mDOM was setup inside a freezer allowing for tests at lower temperatures matching the ones expected in the ice at the depth of deployment. For this thesis, temperatures of -10°C, -20°C and -30°C were selected. Additionally, to model the conditions in the ice in more detail, the mDOM was taped using black adhesive tape. This suppresses internal photon reflection and impacts the index of refraction at the surface of the module such that it is more similar to a glass-ice transition than a glass-air one [37]. A picture of a taped mDOM, in this case mDOM_D049_v1 is shown in Figure 4.4.

[1] This mDOM is also known as 'Back to Life'.

[2] These bots were called "Herbert" and "Papp-Martin", translating to "Cardboard-Martin". For more information on this interlock system and the characters see Appendix B.

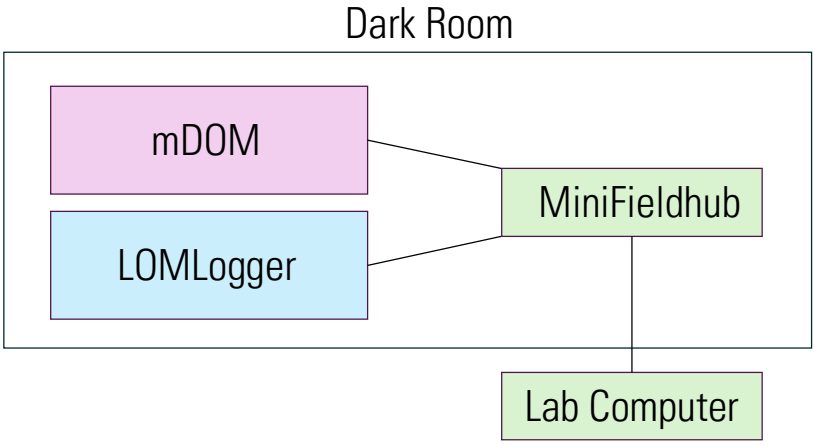

Figure 4.1: Block diagram of experimental setup in Erlangen.

(a) (b)

Figure 4.2: Experimental setup at ECAP site. Left: mDOM inside of its transport box. Right: Transport box covered by some blankets improving the light-tightness. In both pictures, the miniFieldhub is placed on top of a table. The control lights are covered by black tape. A part of the LOMLogger test setup is visible in the upper right corner.

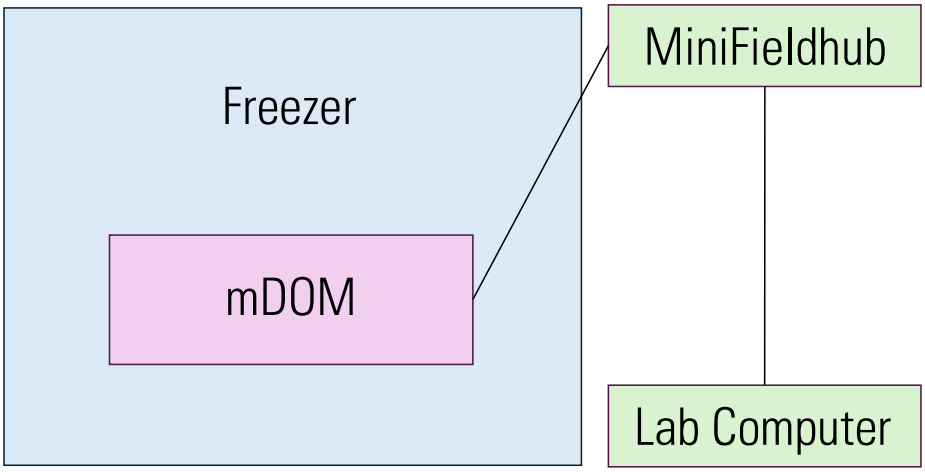

Figure 4.3: Block-diagram of experimental setup in Zeuthen.

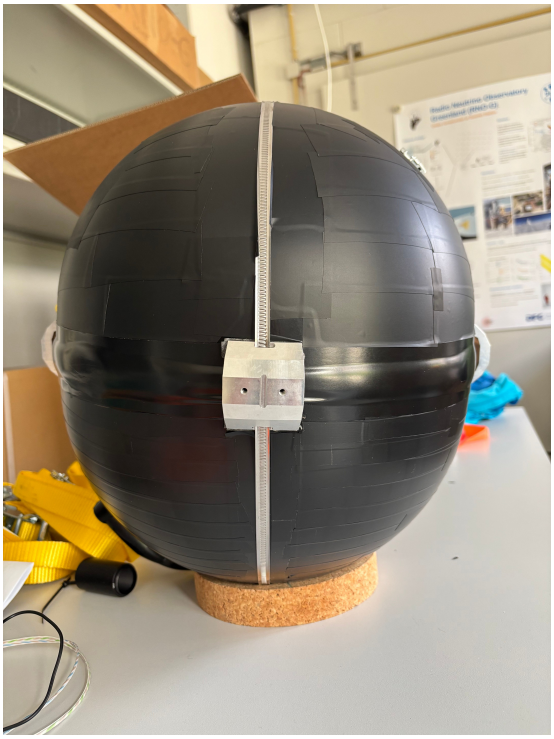

Figure 4.4: Taped mDOM used for measurements in Zeuthen.

(a) (b)

Figure 4.5: Experimental setup at DESY site for mDOM_D049_v1. Left: Freezer in which the mDOM was placed. Right: mDOM inside the freezer, covered by a black plastic bag.

(a) (b)

Figure 4.6: Experimental setup at DESY site for mDOM_D115_v1. Left: Freezer in which the mDOM was placed, covered by blankets. Picture by S. Blot. Right: taped mDOM inside the freezer. Picture by T. Karg.

The first measurements in Zeuthen were performed using mDOM_D049_v1 in the freezer. As this setup itself is not sufficiently light-tight, due to the cable feedthrough at the lid of the freezer, the mDOM was placed in a black plastic bag. Pictures of this setup are shown in Figure 4.5.

As mDOM_D049_v1 was shipped to the South pole during this thesis, it was then replaced by mDOM_D115_v1 from the Erlangen site. For this, mDOM_D115_v1 was taped as well. However, it was not placed in a plastic bag, leading to some issues explained in Chapter 7 in more detail. To improve the light-tightness of the setup, blankets were put on top of the freezer instead. Pictures of this are shown in Figure 4.6.

4.2 Waveform Characterization

The calibration routines developed in this thesis use ADC waveforms, i.e. time series of ADC counts, and the corresponding contained charges. In this section, methods for the waveform characterization and charge integration are explained. The method used for charge extraction is adapted from the charge integration method implemented in the framework of the mDOM Final Acceptance Test (FAT) [61]. Several improvements have been developed in this thesis to more accurately characterize the signal charge. Finally, the used data acquisition modes and different triggers used in this thesis are described.

4.2.1 Pulse Identification and Baseline Calculation

In this thesis, two different types of waveforms are used, PMT and test pulser waveforms (cf. Section 3.3.2). Due to an additional feature in the test pulser waveform, the calculation of the baseline differs slightly. Therefore, the two types of waveforms are discussed separately.

PMT Waveforms

A typical PMT waveform is shown in Figure 4.7. The waveform bins correspond to the time. The signal contained in the waveform is a down-going peak. In this thesis, the peak position is defined as the waveform bin containing the lowest ADC count. This bin will be referred to as reference bin b_{ref} in the following.

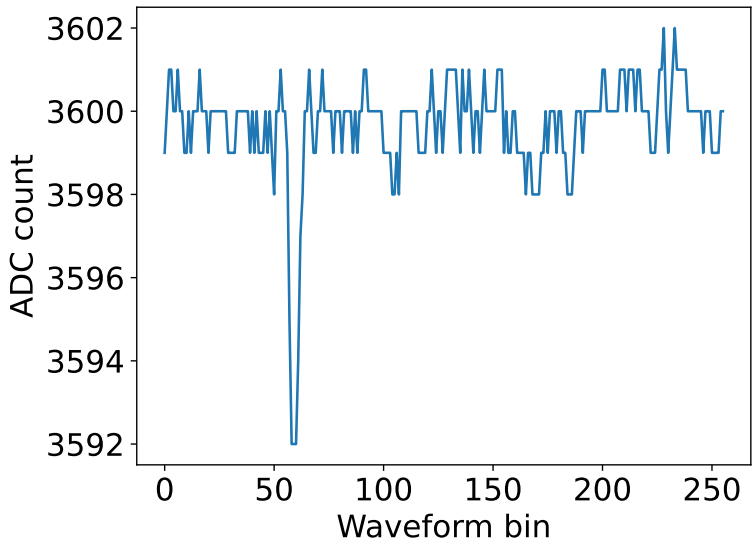

Figure 4.7: Example PMT waveform including one reasonable signal.

The baseline of the waveform only consists of electronic noise of the PMT and AFE. In the mDOM, the baseline offset can be set to a certain ADC value. In this example and throughout this thesis, the PMT baseline is set to 3600 ADC counts. This is referred to as nominal baseline in the following. For a proper charge integration, it is crucial to accurately determine the baseline value from the waveform itself. This is given by the average ADC value in a certain waveform interval. For a more robust determination of the baseline value,

a different measure such as the median could be considered instead.

For FAT, a fixed interval starting 13 bins after b_{ref} with a length of 20 bins is used for the baseline calculation. This interval was used for the measurements in Chapter 5. However, this can lead to a bias in the case a second signal, i.e. dark noise, is contained in this interval. Therefore, the selection of this interval was improved in this thesis. The baseline calculation procedure is shown in Figure 4.8. Waveforms are excluded from further processing in case the distance between peaks is too small or the calculated value deviates more than 2 ADC counts from the nominal baseline of 3600 ADC counts. Such a deviation indicates either an unwanted baseline shift or a poorly chosen interval for the baseline calculation. It was observed that less than 1 % of all waveforms are affected. In one example measurement including 24 PMTs, the average contribution of waveforms with deviating baselines was $0.13 \pm 0.06\,\%$.

The improved baseline calculation method was used for the measurements presented in Chapter 6 and Chapter 7.

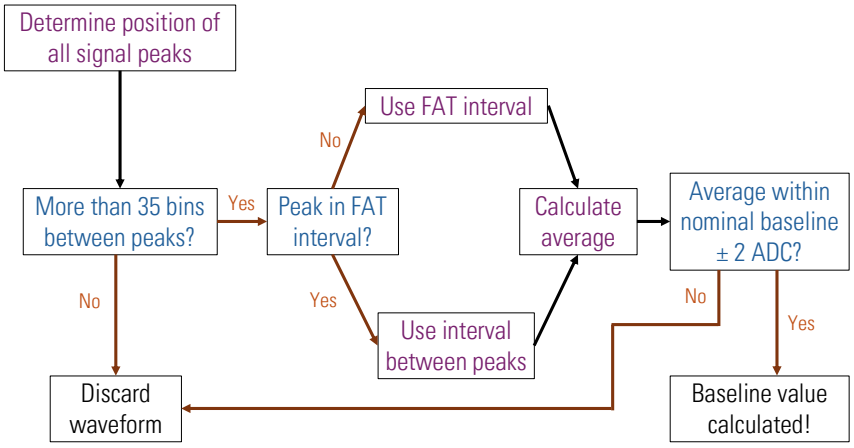

Figure 4.8: Sketch of interval selection procedure for baseline calculation. Peaks that are larger than 4 ADC counts are considered as signals in this procedure.

Test Pulser Waveforms

As described in Section 3.3.2, a test pulser is included in the AFE for each mDOM channel. This pulser is a capacitor that is charged by the FPGA and discharged over the front-end impedance. The discharge curve of the capacitor forms a down-going peak in the ADC waveform shown in Figure 4.9. This is similar to the PMT waveforms described above. However, for the test pulser, the charge curve of the capacitor is also included in the waveform as up-going peak. In this case, the interval for baseline calculation of the test pulser waveforms is fixed and is located between the charge and the discharge curve of the test pulser.

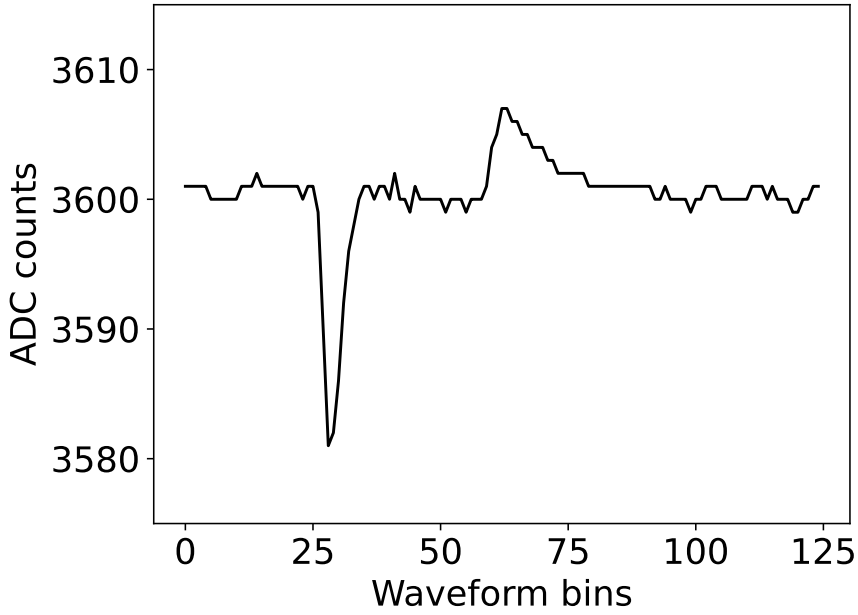

Figure 4.9: Example test pulser waveform. Down-going peak corresponding to discharge curve of the test pulser capacitor. Up-going peak corresponding to charge curve of the capacitor.

4.2.2 Charge Integration

All described calibration routines rely on the charges that are contained in the individual waveforms. For this, the area of the peak must be integrated and the unit must be converted to either pC or photoelectrons (P.E.) in this work. In IceCube, a more sophisticated approach called "WaveDeform" is used [62], [43]. The calibration routines presented here would profit from such an approach, however, implementing this for the mDOM was beyond the scope of this thesis.

The first step of the charge calculation in this thesis is to determine a suitable integration window around the signal peak. The position of the peak, b_{ref} is determined as described in Section 4.2.1. The integration window is then defined relative to this position:$[b_{\text{ref}}-5,b_{\text{ref}}+8]$. This interval is shown as a blue shaded region around the peak in Figure 4.10. The asymmetry of this interval is justified by the steep rising edge and shallower falling edge of the initial PMT signal (cf. Section 2.3.1). The values were taken from FAT [63].

In this thesis, this default integration interval is used for the measurements presented in Chapter 5. For the other measurements, the predefined integration interval was used unless the peak was located close to the edges of the waveform. In this case, the waveform was discarded. Additionally, the probability of acquiring such waveforms was reduced during this thesis. For later measurements such as described in Chapter 7, a variable waveform readout is used. In this case, a waveform includes 10 waveform bins before the initial trigger occurred and 40 bins after the end of the trigger.

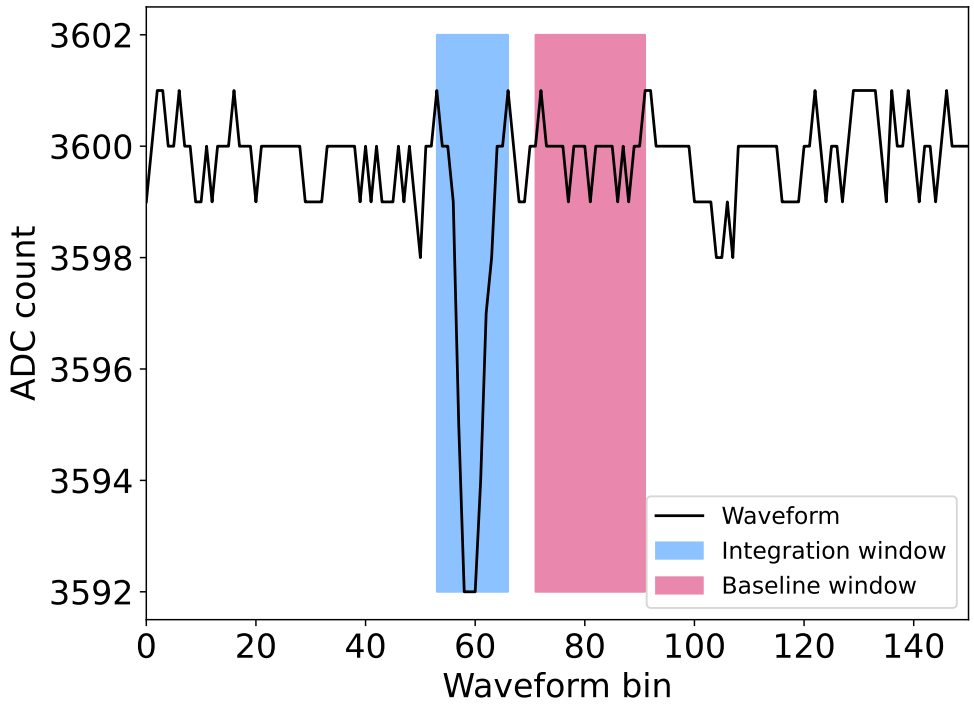

Figure 4.10: Example waveform processed by charge integration function. The shaded region around the peak itself is the integration window. The region right to it is the default choice for the required baseline calculation.

The baseline of the waveform is calculated as described in Section 4.2.1. The default baseline window is shown in Figure 4.10 as pink shaded region right to the signal peak. The baseline value is then subtracted from the waveform. This baseline corrected signal is then integrated using the trapezoidal rule implemented in `np.trapz()`[3]. The integrated charge value is first of all given in arbitrary units, as waveform bins and ADC counts are used for the integration. To extract the charge from the PMT output in pC, properties of individual mDOM components need to be considered. The conversion factor Q_{cf} can be calculated using the relations $Q = I \cdot t$, $I = U/R$ and $t = 1/f$ with charge Q, current I, voltage U, resistance R, time t and frequency f. Based on this, the general charge conversion factor is given by:

$$Q_{\text{cf}} = \frac{U_{\text{cf}}/R_{\text{front-end}}}{f_{\text{ADC}}} \tag{4.1}$$

In this sense, $R_{\text{front-end}}$ is the front-end impedance of the mDOM and f_{ADC} is the ADC sampling rate. The conversion factor between ADC counts and mDOM voltage U_{cf} is given by $U_{\text{cf}} = U_{\text{cf,ADC}}/\text{gain}_{\text{front-end}}$ with $U_{\text{cf,ADC}}$ defined by the voltage range and total counts of the ADC in use. This factor accounts for the fact that the PMT signal is amplified before the ADC readout.

[3]Documentation of np.trapz(). Accessed: 13.10.2025.

Combining this with Equation 4.1, the charge conversion factor of an mDOM results in [61]:

$$Q_{\text{cf}} = 1 \cdot 10^{12} \frac{U_{\text{cf,ADC}}}{\text{gain}_{\text{front-end}} \cdot R_{\text{front-end}} \cdot f_{\text{ADC}}} \approx 0.00488\,\text{pC/a.u.} \tag{4.2}$$

The integrated peak area in arbitrary units must be multiplied by this factor to obtain the charge in pC. The value is calculated using the mDOM properties displayed in Table 4.1. This charge q_{pC} in pC can be converted into the charge $q_{\text{P.E.}}$ in P.E.:

$$q_{\text{P.E.}} = \frac{q_{\text{pC}}}{e \cdot g_{\text{PMT}} \cdot 10^{12}}\,\text{P.E.} \tag{4.3}$$

with elementary charge e and PMT gain g_{PMT}.

Table 4.1: mDOM properties required to calculate charge conversion factor [61].

mDOM Property	Value
$U_{\text{cf,ADC}}$	$\frac{2}{4096}\frac{\text{V}}{\text{counts}}$
$\text{gain}_{\text{front-end}}$	11.12
$R_{\text{front-end}}$	75 Ω
f_{ADC}	120 MHz

4.2.3 Characterization of Pulse Shape

The signal pulses can not only be characterized by their charge but also by their width and height. This will be especially relevant for the discriminator threshold calibration routine using the test pulser described in Appendix E. For this routine, not only the corresponding charge but also the overall shape of the pulses must be comparable to the reference PMT pulse.

The pulse height is therefore defined as difference between the baseline calculated as described in Section 4.2.1 and the minimum value of the pulse.

To determine the pulse width, i.e. the full width at half maximum (FWHM), a Gaussian function is fitted to the pulse. An example is shown in Figure 4.11. From this fit, the FWHM can be calculated [64]:

$$\text{FWHM} = 2\sqrt{2\ln 2}\sigma. \tag{4.4}$$

As described in Section 2.3.1, a PMT signal approaches a Gaussian for an infinite number of dynodes. Therefore, this is just an approximation for the real pulse shape.

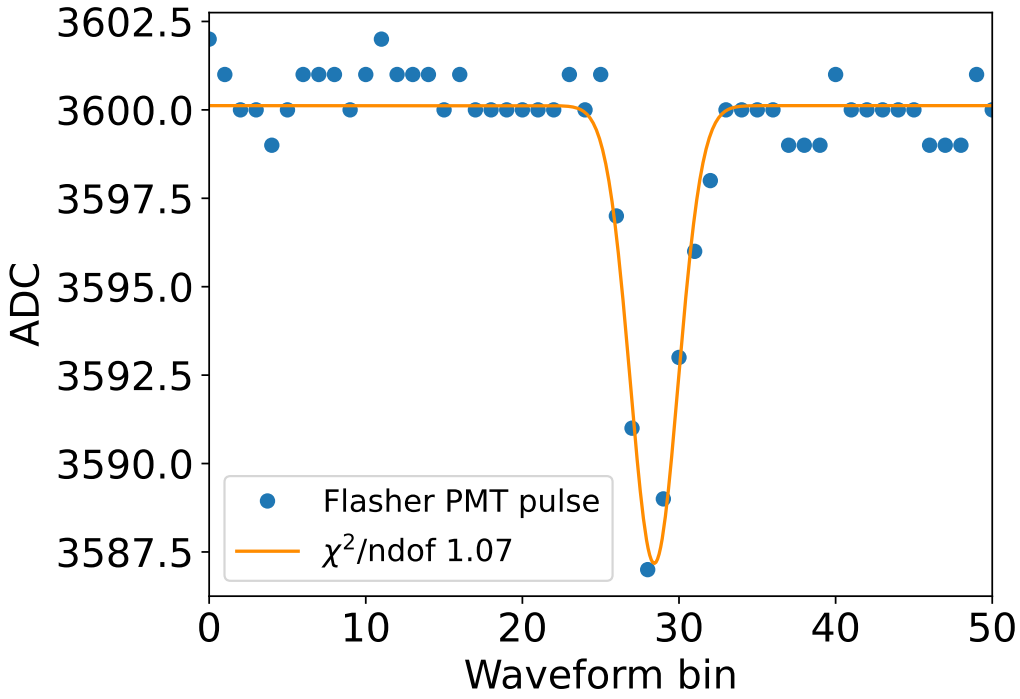

Figure 4.11: Example of flasher induced PMT pulse with corresponding Gaussian fit.

4.3 Data Acquisition

The mDOM features different options to readout ADC waveforms [56]. Here, only the triggers used in this thesis are described in detail.

A readout can be triggered by the discriminator [56]. In this case, a waveform is read out when a PMT signal exceeds the set reference voltage also referred to as discriminator threshold. This is the trigger mode that is expected to be used in-situ for the IceCube Upgrade modules [58]. In this thesis, this trigger is used for the PMT gain calibration using dark noise described in Chapter 5.

Additionally, a calibration trigger is implemented [56]. For this, the FPGA sends periodic trigger signals. In combination with an enabled flasher chain, the PMT readout can be made synchronous to a light flash from the LEDs. This is therefore also referred to as LED or flasher trigger. This trigger is relevant for the calibration routines used in the final acceptance testing (FAT) of the mDOMs. In Chapter 5 and Chapter 6, these routines are used as comparison for the procedures developed in the scope of this thesis.

Furthermore, a trigger is implemented that initiates a readout if the ADC value is equal to or smaller than a selected reference, which is referred to as "ADC trigger" [56]. The discriminator threshold calibration based on dark noise presented in Chapter 6 utilizes this trigger. In addition, waveforms can be acquired in coincidence with the front-end test pulser fired by the FPGA [56]. This is relevant for the calibration routine described in Appendix E.

In addition to the raw waveforms, the information if the discriminator was triggered or not can be recorded [56]. This information is stored in the "discWords" array. It includes the same number of bins as the corresponding waveform. As the discriminator is sampled 8 times faster than the ADC, each bin contains an 8-bit binary of which the least significant bit stores the earliest information. In this thesis, the discriminator response is required for the discriminator threshold calibration routine described in Chapter 6.

5 PMT Gain Calibration using Dark Noise

Before a PMT can be used in an experiment, it needs to be calibrated properly. The correct setting of the amplification factor is for example crucial for a reasonable energy reconstruction. An example how a deviation in gain impacts the determination of the number of photoelectrons is displayed in Figure 5.1. This uses the relation given in Equation 4.3 with a fixed observed charge in pC. For example, a gain that is 6 % higher than the target gain will lead to a 5.7 % bias in the observed charge in P.E, i.e. the charge in terms of photoelectrons.

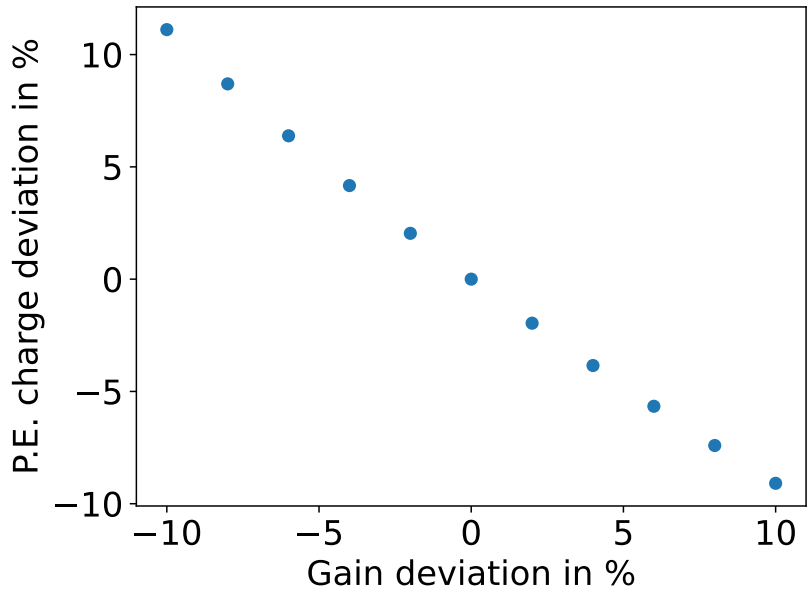

Figure 5.1: Photoelectron charge deviation in dependence of the gain deviation from the target gain. The observed charge in pC is the same for all data points.

In general, the interpretation of the expected gain deviation depends on the goal of the respective analysis. It is known that the gain calibration and estimation is sensitive to even small changes in the fit routine [33]. The primary goal of this part of the thesis is to investigate the feasibility and performance of a high voltage - gain calibration routine using dark noise. Such a routine has the advantage that no artificial light is required. Therefore, this will be possible in case of a flasher LED dysfunction. In addition, a similar approach could be used to monitor the gain settings of the mDOMs during the detector up-time.

The calibration routine using dark noise was first developed and tested within this thesis. Consequently, deviations of up to 5 % from the target gain will be considered acceptable in the following. This is consistent with the engineering requirements of the mDOM PMTs [65].

5.1 Methods and Procedure

In this section, the overall calibration procedure is explained. In addition, the methods used for the evaluation of the calibration are presented. This includes two fit approaches for the SPE charge spectra and the binnings that were tested in this thesis.

5.1.1 General Calibration Approach

The goal of this calibration routine is to find the high voltage (HV) required to reach the target gain of $5 \cdot 10^6$ for the mDOM PMTs. The general calibration procedure was adapted from the LED based approach used in mDOM FAT [61] and was transformed into a dark noise based approach within this thesis.

In FAT, this calibration is done by sweeping through a range of applied HV. This high voltage is both applied to and monitored at dynode stage 10 (DY10) (cf. Section 3.3.1). At each HV, an SPE charge spectrum is recorded using the flasher LEDs. A PMT response function is fitted to the SPE charge spectra and the corresponding gain is extracted from the SPE peak position as given by Equation 2.10. An example is shown in Figure 5.2 (a). Finally, the target high voltage setting for the target gain is extracted from a power law fit to the gain data in dependence of the corresponding high voltage setting. An example can be seen in Figure 5.2 (b).

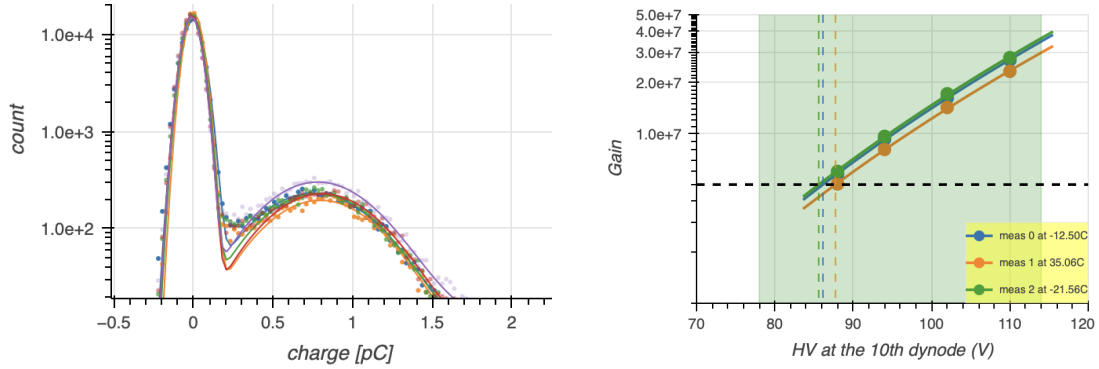

Figure 5.2: Example for key steps in PMT gain calibration from FAT for different temperatures. Left: SPE charge spectrum with corresponding PMT response fit. Right: Power law fit to gain data in dependence of the HV setting. Figures from [63].

For the dark noise based calibration routine developed in this thesis, the same HV settings as in FAT are used, i.e. settings of 78 V, 82 V, 88 V, 94 V and 102 V. This interval is based on the target HV values observed for all PMTs during the initial PMT testing [35]. In the dark noise based routine, the discriminator trigger is used to record an SPE charge spectrum at each HV setting. The threshold is set 1.25 mV above the noise level. Thus, the charge

spectrum does not contain a pedestal as shown in Figure 5.3 for two HV settings. In this thesis, two fit models for the PMT response are developed and tested to accommodate for the missing pedestal. These fit approaches are described in Section 5.1.2. The target HV is extracted from a power law fit as done for the flasher based FAT routine.

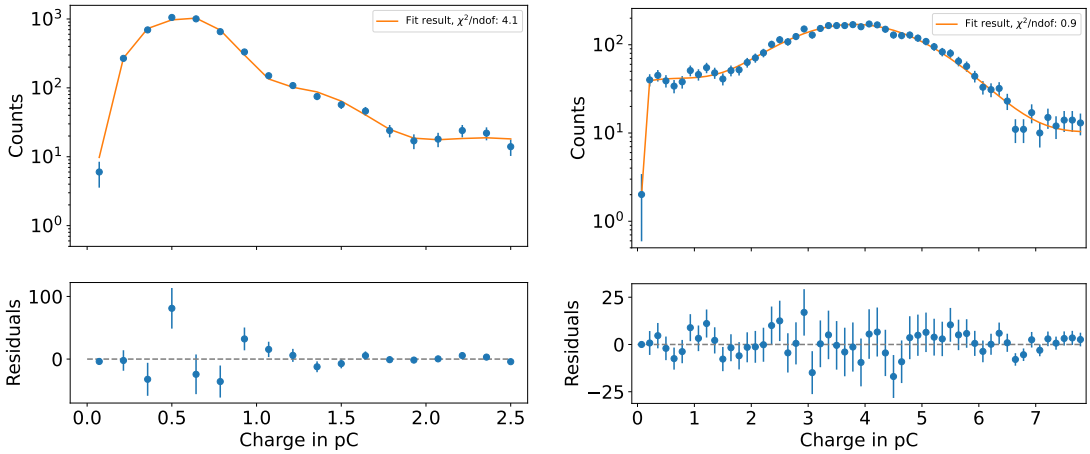

Figure 5.3: Example for dark noise SPE spectra. Left: Low HV setting (78 V). The pedestal and the poorly amplified electrons are cut off by the discriminator on the left of the SPE peak. Right: High HV setting (102 V). The spectrum contains a contribution of poorly amplified electrons that is cut off by the discriminator towards low charges.

As shown in Figure 5.3, the shape of the SPE spectra varies with the set HV value. Therefore, the SPE response fit must be flexible enough to account for the observed differences. To improve the performance of the calibration, a narrower HV scan range would be preferred. The approximate target HV value for each individual PMT from FAT and the initial PMT testing is known [5], [35]. This could be used as starting point for a narrower, customized HV scan range of each individual PMT in the future [58].

In general, the data used for the HV - gain calibration based on dark noise was acquired channel by channel, resulting in an overall measurement time between 90 minutes and 100 minutes for all 24 channels. This time can be significantly reduced when a parallel approach is chosen for the data acquisition. In this case, all 24 channels can be calibrated simultaneously.

Longer measurement times would increase the statistics in the individual SPE spectra. It is expected that the precision of the fits is increased. However, normal detector operations are not possible during the calibration. Thus, a compromise between short detector down-times and sufficient statistics in the SPE spectra is required for the gain calibration.

5.1.2 SPE Fit Approaches

In this section, two different fit methods for the dark noise generated SPE charge spectra are presented.

5.1.2.1 Maximum Likelihood Approach

In FAT, the SPE spectra are fitted using the software `pmt_taco`[1], initially developed for PMT testing at the mDOM PMT-base-assembly facilities [66]. In this software, the SPE spectrum is described by three Gaussians, one for the pedestal, one for the SPE component and one for the 2PE contribution. The poorly amplified electrons are represented by a combination of an error function with a cutoff at 0 charge and an exponential function. This leads to the following overall functional form:

$$\begin{aligned} F(q) = & A_{\text{ped}} \frac{1}{\sqrt{2\pi\sigma_{\text{ped}}^2}} e^{-\frac{(q-\mu_{\text{ped}})^2}{2\sigma_{\text{ped}}^2}} + \\ & + A_{\text{SPE}} \frac{1}{\sqrt{2\pi\sigma_{\text{SPE}}^2}} e^{-\frac{(q-\mu_{\text{SPE}})^2}{2\sigma_{\text{SPE}}^2}} + A_{\text{2PE}} \frac{1}{\sqrt{2\pi(\sqrt{2}\sigma_{\text{SPE}})^2}} e^{-\frac{(q-2\mu_{\text{SPE}})^2}{2(\sqrt{2}\sigma_{\text{SPE}})^2}} + \\ & + A_{\text{cutoff}} \cdot \frac{1}{2} \left(1 + \text{erf}\left(\frac{10}{\sqrt{2}} q\right)\right) e^{-\frac{q}{b_{\text{cutoff}}}}. \end{aligned} \tag{5.1}$$

In this equation, the first two lines are properly normalized probability density functions (PDFs). However, the contribution describing the poorly amplified electrons is not a PDF. A normalization factor should be included in the future.

The position and standard deviation of the Gaussian representing the 2PE contribution is defined relative to the SPE peak of the distribution. The form of the 2PE contribution can be derived from a convolution of the SPE peak with itself, resulting again in a Gaussian function with twice the standard deviation of the SPE peak [67]. In a more evolved fit model, poorly amplified electrons need to be considered as a contribution to the 2PE peak as well. In this kind of models, the convolution for the 2PE region also includes the low charge region of the spectrum [43]. This will be described in Section 5.1.2.2 in more detail.

For the dark noise based measurement, an SPE spectrum is recorded by triggering on the discriminator as mentioned in Section 5.1.1. The pedestal is located below this value and is therefore not included in such a spectrum. Thus, the Gaussian representing the pedestal is removed from the fit function. To account for the cutoff generated by the discriminator threshold, an additional fit parameter c_{cutoff} describing the position of the error function is introduced. This cutoff is only applied to the contribution of the poorly-amplified electrons. In a future fit, this cutoff should be applied to the full model and not only to a single component. In this thesis, a total of 7 fit parameters is considered for the dark noise based calibration:

$$\begin{aligned} F(q) = & A_{\text{SPE}} \frac{1}{\sqrt{2\pi\sigma_{\text{SPE}}^2}} e^{-\frac{(q-\mu_{\text{SPE}})^2}{2\sigma_{\text{SPE}}^2}} + A_{\text{2PE}} \frac{1}{\sqrt{2\pi(\sqrt{2}\sigma_{\text{SPE}})^2}} e^{-\frac{(q-2\mu_{\text{SPE}})^2}{2(\sqrt{2}\sigma_{\text{SPE}})^2}} + \\ & + A_{\text{cutoff}} \cdot \frac{1}{2} \left(1 + \text{erf}\left(\frac{10}{\sqrt{2}} (q - c_{\text{cutoff}})\right)\right) e^{-\frac{q}{b_{\text{cutoff}}}}. \end{aligned} \tag{5.2}$$

An example for this model fitted to an SPE spectrum is show in Figure 5.4. The individual

[1] IceCube internal software.

components of the model are indicated.

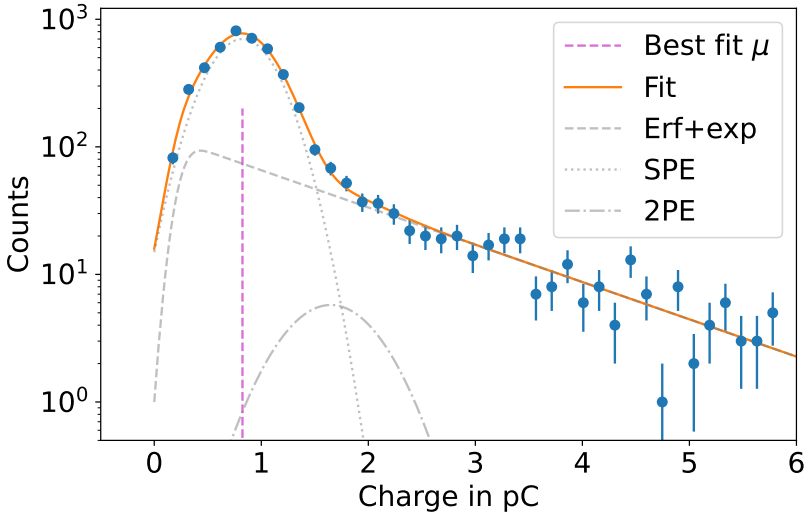

Figure 5.4: Example for a dark noise SPE spectrum fitted with the PMT response model adapted from mDOM FAT and the initial PMT testing. This model is given by Equation 5.2. The individual components contributing to the overall model are visualized.

Instead of using a χ^2 fit as done during FAT, a maximum likelihood approach was chosen for the dark noise based HV-gain calibration. χ^2 fits typically rely on Gaussian uncertainties [68]. The uncertainties in the recorded SPE spectrum however follow a Poisson distribution. According to the central limit theorem, a Poisson distribution can be described by a Gaussian distribution for larger statistics [69]. This assumption therefore is not applicable for a small amount of counts per bin, e.g. for bins with less than 10 counts. In the higher charge tails of the SPE spectra, the counts per bin fall below this threshold. Thus, their uncertainties can not be considered Gaussian which might impact the fit result of a χ^2 minimization [68]. Using a Poisson maximum likelihood fit avoids this complication.

For this fit implementation, the charges are filtered depending on the applied high voltage. For high voltages below $83\,\mathrm{V}$, charges up to $6\,\mathrm{pC}$ are considered. For high voltages above, charges up to $10\,\mathrm{pC}$ were included in the fitted spectrum. This choice is based on the observation that the contribution above these charges at room temperature is low for the investigated PMTs but the exact values were chosen arbitrarily based on measurements using mDOM_D115_v1 at room temperature. During integration, the PMTs for each mDOM were selected based on their target high voltage at nominal gain to achieve similar settings for each of the PMTs in one mDOM [58]. Thus, the high voltage ranges for charge filtering defined here are not generally applicable and might impact the overall fit result. Therefore, in a high precision gain measurement, such an arbitrary choice of charge cutoff should be avoided.

A Poisson likelihood fit of Equation 5.2 is used with additional penalty terms. An overview of the used conditions is shown in Table 5.1. The constraints on the SPE peak position correspond to gains of $12.5 \cdot 10^5$ and $5 \cdot 10^7$ which are not expected to be reached at the investigated high voltage settings.

Table 5.1: Summary of penalty term conditions used for the maximum likelihood fit.

Targeted parameter	Condition / Preference
Amplitude (Positivity)	All amplitudes > 0
Amplitude (Ratio)	$A_{\text{SPE}} > A_{\text{2PE}}$
SPE peak position	$< 2\,\text{pC}$ for HV $< 80\,\text{V}$
	$< 8\,\text{pC}$ for HV $\geq 80\,\text{V}$
Cutoff exponent	$b_{\text{cutoff}} > 0$
Cutoff position	$c_{\text{cutoff}} < \mu_{\text{SPE}}$

The fit procedure itself is based on `iminuit`[2]. First, initial start parameters are extracted from the charge histogram itself. An overview on the determination is provided in Table 5.2. In this table, $q_{\text{half-width}}$ is the charge at which the spectrum falls below half of A_{SPE} on the right side of the SPE peak.

Table 5.2: Summary of initial parameter estimates for the maximum likelihood fit model. In this table, $q_{\text{half-width}}$ is the charge at which the spectrum falls below half of A_{SPE} to the right side of the SPE peak.

Parameter	Initial value / estimation rule
A_{SPE}	Maximum of distribution (excluding first bins)
μ_{SPE}	Charge at maximum of distribution (excluding first bins)
σ_{SPE}	$\sigma_{\text{SPE}} = \frac{\text{FWHM}}{2\sqrt{2\ln 2}}$ with FWHM=$(\mu_{\text{SPE}}\text{-}q_{\text{half-width}}) \cdot 2$
A_{2PE}	20 counts (arbitrary)
A_{cutoff}	Maximum before SPE peak
b_{cutoff}	$0.1 \cdot \mu_{\text{SPE}}$ (empirical, cf. `pmt_taco` [66])
c_{cutoff}	0.4 P.E. (expected discriminator cutoff: 0.1–0.4 P.E.)

The fit was found to yield different results depending on the initial parameters. This is most likely due to the fit converging to a local minimum in the parameter space. To reduce the influence of the input parameters, the fit procedure shown in Figure 5.5 was developed. The fit is repeated 5 times and the best fit with the corresponding fit parameters and uncertainties is considered. The other fits and parameters are discarded. For the best fit, the likelihood profile for the SPE peak position is determined to ensure that a global minimum was found. An example likelihood profile for the SPE peak position is shown in Figure 5.6. Likelihood profiles for the other fit parameters were not determined as the SPE peak position is the only relevant parameter for the gain calibration.

This whole procedure can be further optimized by running `simplex` only once and then using the perturbation of the fit results as initial parameters for the `migrad` based fit. Additionally, as shown in Figure 5.4, the higher PE contribution is described by the exponential function modeling the poorly amplified electrons on the left side of the spectrum. From a physical point of view, this is not intended. Thus, the fit would profit from including fur-

[2]Documentation of iminuit. Accessed: 24.11.2025.

ther nPE contributions and a penalty term constraining the slope of the exponential function.

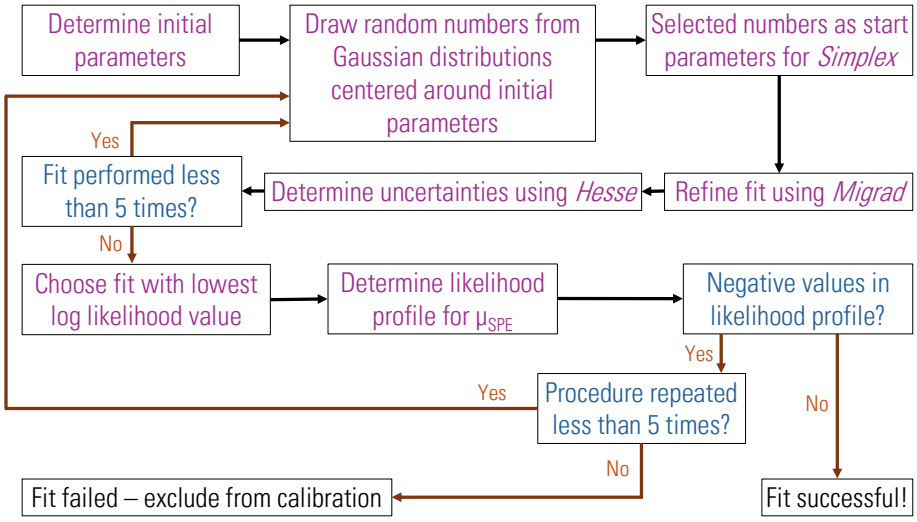

Figure 5.5: Poisson likelihood fit routine for dark noise generated SPE spectra.

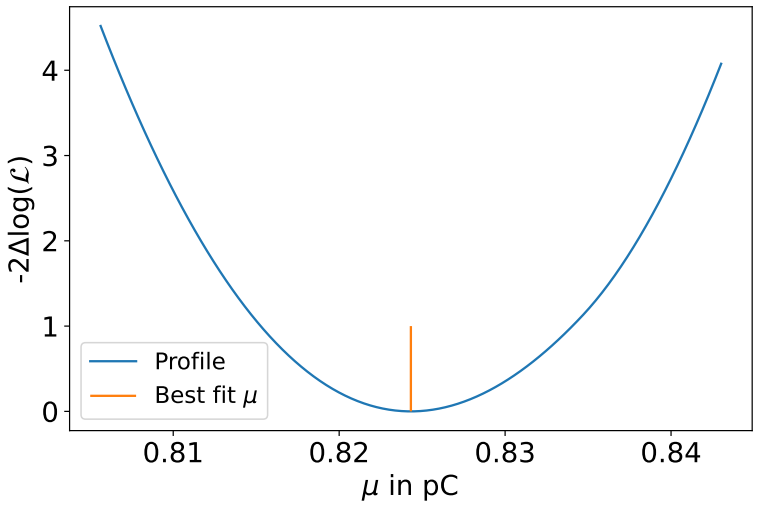

Figure 5.6: Example for a likelihood profile for the SPE peak position. This corresponds to the fit shown in Figure 5.4.

5.1.2.2 Convolutional Fit Approach

The fit approach described in this section is based on the convolutional fit used for modeling the charge response of the IceCube PMTs [70]. The fit function and the fit procedure presented in this section deviate therefore from the method used in Section 5.1.2.1.

The overall function was again adapted by removing the term describing the pedestal of the spectrum and introducing two variables describing the position and slope of an error function cutoff towards low charges. Furthermore, the model was extended to consider multi

PE contributions up to 5 photoelectrons. The original IceCube code only included a 2PE contamination.

The part of the spectrum consisting of poorly amplified photoelectrons in this model f_{PA} is described empirically by a Gaussian function with an error function cutoff towards lower charges:

$$f_{\mathrm{PA}}(q) = \frac{n_{\mathrm{PA}}}{\sqrt{\frac{\pi}{2}} \cdot \sigma_{\mathsf{PA}} \cdot \mathrm{erfc}\left(\frac{q_{\mathrm{cutoff}} - \mu_{\mathsf{PA}}}{\sqrt{2}\,\sigma_{\mathsf{PA}}}\right)} \exp\left(-\tfrac{1}{2}\frac{(q-\mu_{\mathrm{PA}})^2}{\sigma_{\mathrm{PA}}^2}\right) \cdot \frac{1}{2}\,\mathrm{erfc}\left(\frac{q_{\mathrm{cutoff}} - q}{\sqrt{2}\,\sigma_{\mathrm{cutoff}}}\right). \tag{5.3}$$

In this function, n_{PA} is the norm of the error function modified Gaussian function. The mean and the width of the Gaussian are given by μ_{SPE} and σ_{SPE}. While q_{cutoff} and σ_{cutoff} describe the position and slope of the error function.

The SPE peak is defined as a normalized Gaussian function:

$$f_{\mathrm{SPE}}(q) = \frac{n_{\mathrm{SPE}}}{\sqrt{\frac{\pi}{2}} \cdot \sigma_{\mathsf{SPE}} \cdot \mathrm{erfc}\left(\frac{-\mu_{\mathsf{SPE}}}{\sqrt{2}\,\sigma_{\mathsf{SPE}}}\right)} \exp\left(-\tfrac{1}{2}\frac{(q-\mu_{\mathrm{SPE}})^2}{\sigma_{\mathrm{SPE}}^2}\right). \tag{5.4}$$

Here, n_{SPE} is the norm of the SPE peak which can be expressed as $n_{\mathsf{SPE}} = 1 - n_{\mathsf{PA}}$.

These two contributions are then combined to describe the complete lower charge region of the SPE spectrum:

$$f_{\mathsf{lower\text{-}charge}} = f_{\mathsf{PA}} + f_{\mathsf{SPE}}. \tag{5.5}$$

The full model describing the charge spectrum is then given by the weighted sum of the n-fold convolutions of $f_{\mathsf{lower\text{-}charge}}$ with itself. In this thesis, a 5-fold convolution is used as cutoff:

$$F_{\mathsf{model}}(q) = \sum_{n=1}^{5} A_n\, f^{(*n)}_{\mathsf{lower\text{-}charge}}(q). \tag{5.6}$$

The overall fit model includes 12 fit parameters and the convolution is calculated using `scipy.signal.fftconvolve`[3].

It was later noticed that the convolution calculated to describe the higher PE contribution is not entirely correct. In theory, the nPE distribution is obtained by convolving the entire low-charge region with itself. This means that contributions from charges below the discriminator threshold must be included. In this thesis, the convolution contains only the observed part of the lower charge region above the discriminator cutoff and not the full low charge contribution.

[3]Documentation of fftconvolve. Accessed: 16.10.2025.

In the future, charges below the discriminator threshold should be included in the spectrum to describe the full lower charge region. This can be achieved by an improved pulse selection, considering smaller signals obtained in the discriminator triggered waveforms as done for IceCube [70]. It is expected that the impact of this change is small, i.e., below the precision requirement of 5 %, as this change will mainly affect the calculation of the higher charge region. This means that the SPE peak position and therefore the gain extraction will only be affected indirectly.

Before the model is fitted to the data, all bin counts are divided by the maximum number of counts observed in the spectrum. Thus, the data is scaled down such that the maximum y-value is 1. The uncertainties in the SPE charge spectrum are calculated using Poisson statistics of the original spectrum and are then scaled according to the scaling of the full spectrum. The fit is performed using `scipy.optimize.curve_fit`[4]., i.e. it is a χ^2 minimization. As discussed in Section 5.1.2.1, this fit requires Gaussian distributed uncertainties. Thus, at least 10 counts per bin of the unscaled spectrum are necessary to fulfill this requirement. In this routine, a charge cutoff is introduced to the spectrum when a bin contains less than 10 counts. This means that only bins with lower charges than the cutoff bin are considered in the fit. A fixed set of initial parameters and boundaries ensuring physically realistic values is used. Values such as the initial SPE peak position and the position of the poorly amplified electron Gaussian with error function modulation are defined relative to the charge corresponding to the maximum of the spectrum. In addition, fixed boundaries are defined.

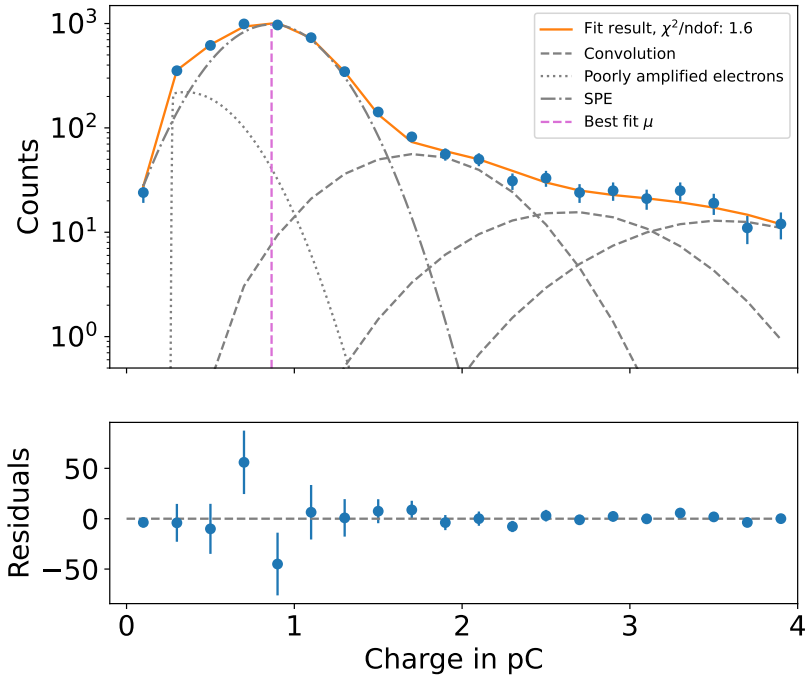

Figure 5.7: Example for an dark noise SPE spectrum fitted with the convolutional fit approach. The individual components contributing to the overall model are visualized.

[4]Documentation of scipy.optimize.curve_fit. Accessed: 16.10.2025.

After the fit, the spectrum is re-scaled for final display. An example SPE spectrum with a corresponding convolutional fit is shown in Figure 5.7. The individual components of the model are included. The residuals in the lower part are given by the absolute distance between the data points and the fit. The feature in the residuals where the data points deviate from the fit in the lower charge region is observed in almost all fits independent of the channel and the high voltage settings. This might be a result of the mathematical uncertainties of the SPE model at low charges. Thus, the fit would profit from an improved description of the low charge region, i.e. the contribution of the under-amplified electrons.

The fit function described in this section could be embedded into a fit procedure similar to the one presented in Section 5.1.2.1. Using a Poisson likelihood fit would avoid the requirement to filter the data based on the counts in a bin. In addition, the hard boundaries used for this approach could be replaced by softer penalty terms. However, this was not investigated in this thesis.

5.1.3 Binning Options

Before the SPE charge spectra can be fitted using the approaches explained in Section 5.1.2.1 and Section 5.1.2.2, the collected charge data must be binned properly. A fine binning will reduce the statistics per bin drastically while a coarse binning will mask important features of the spectrum.

In this thesis, two different types of binnings were tested for the SPE charge spectra used in the HV - gain calibration. One of the investigated binnings uses a fixed number of bins in a certain interval. Different values were tested and the corresponding results are presented in Appendix C. For the second approach, the binning is based on the underlying charge distribution. The bin width is determined following the Freedman-Diaconis rule using the interquartile range IQR of the distribution [71]:

$$\text{bin width} = 2 \cdot \frac{IQR}{\sqrt[3]{n}} = 2 \cdot \frac{Q_3 - Q_1}{\sqrt[3]{n}} \tag{5.7}$$

In this case, Q_1 is the lower quartile, corresponding to the 25th percentile and Q_2 is the 75th percentile of the distribution. The total number of counts in the distribution is given by n. However, this rule was derived in the context of normal distributions which might not be ideal for the considered SPE distributed charges. In general, this binning yields different numbers of bins depending on the exact structure of the data. Thus, the bin widths between the different high voltage settings for the same channels will deviate from each other.

It was found that the binning does not influence the gain calibration routine. The observed deviations in target gain were within the fit uncertainties of the power law function. Therefore, a fixed number of bins was chosen for both fit approaches. Details of the corresponding analysis are provided in Appendix C.

5.2 Analysis and Results

In this section, the analysis and results of the PMT HV - gain calibration routine using dark noise are presented. Furthermore, the potential impact of the HV scan range on the calibration and the calibration results are discussed.

5.2.1 Impact of Scan Range on Target HV

An example for the gain data in dependence on the set HV with a corresponding power law fit is shown in Figure 5.8. This fit is used to extract the target HV setting. A measurement at -30°C is considered. The gain was determined from the raw data using the maximum likelihood approach. The target high voltage is extracted from the power law fit corresponding to the target gain. The residuals show that the data point at 102 V lies below the fit, while most of the other data points are located above the fit. Thus, a deviating fit result is expected in case the data point at 102 V is not considered. A fit without the data point at 102 V would lead to a change in target HV by 0.02 % compared to the result considering this data point. This difference is small.

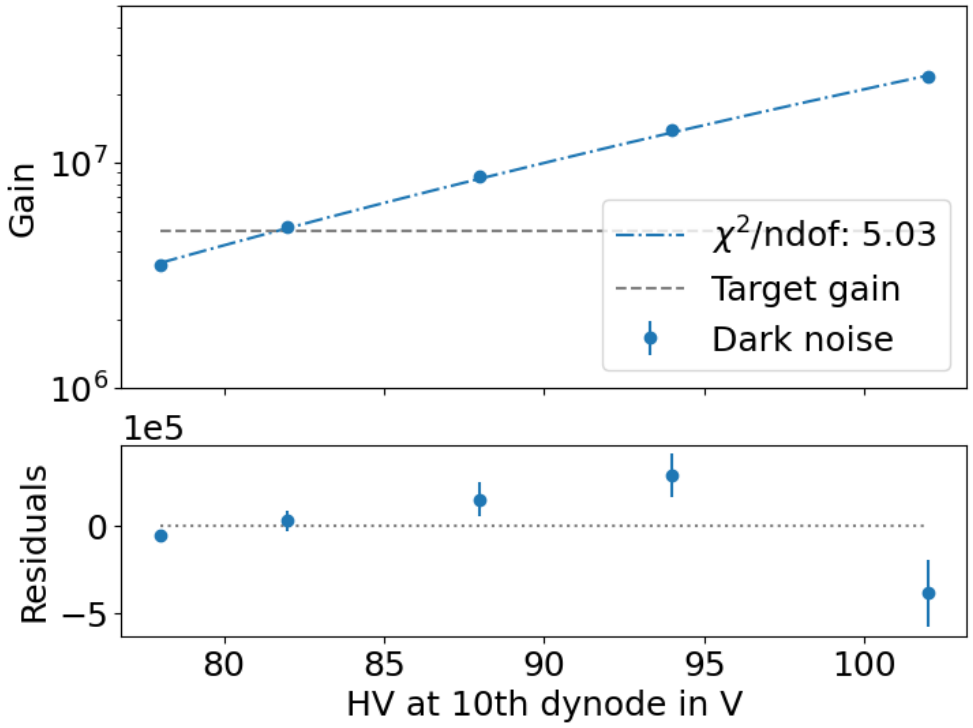

Figure 5.8: Example for the gain calibration function. The data points were extracted from SPE charge spectra using the maximum likelihood fit approach. A power law function fitted to the gain values in dependence of the set high voltage is included. The target HV is extracted from this fit.

However, the corresponding deviation in gain is of interest. Therefore, an average power law function was constructed to estimate the expected gain deviation for a certain HV deviation. The median of the obtained fit parameters of the power law function was calculated for one

calibration run. This included all 24 channels. These averaged parameters a, and b were then used to model the gain deviation:

$$\text{gain deviation} = \frac{a \cdot (\text{target HV} \cdot (1 + \text{target HV deviation}))^b}{\text{target gain}} - 1 \tag{5.8}$$

The target HV was determined from the average power law function at the target gain of $5 \cdot 10^6$.

Equation 5.8 is modeled in Figure 5.9. A deviation of 0.02 % in the target HV leads to a deviation of approximately 1.4 % in target gain. Following Chapter 5, this deviation is negligible. However, it is expected that a reduced HV scan range will improve the goodness of the power law fit and with this, the precision of the extracted target HV.

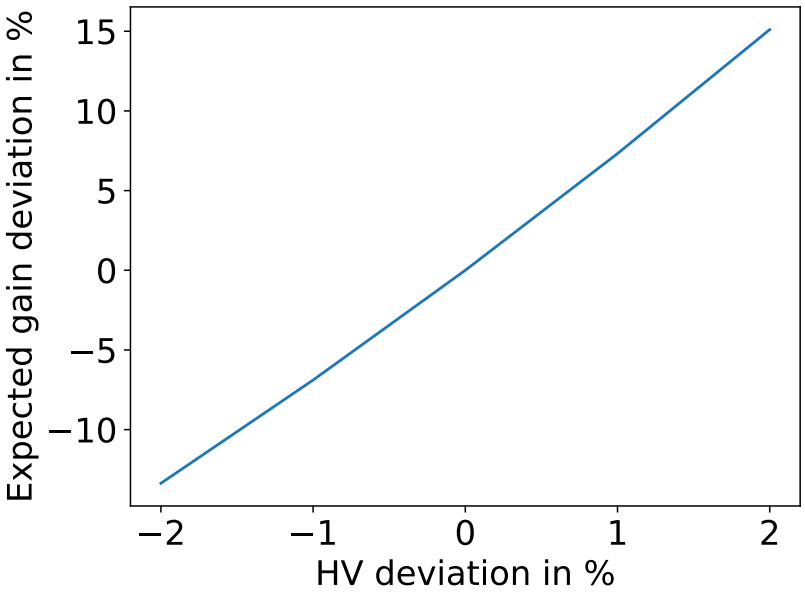

Figure 5.9: Influence of the target HV setting on the expected gain. Average fit parameters of the power law function are used.

5.2.2 Calibration and Verification

In this section, the overall calibration results are discussed. This includes a reproducibility study of the calibration results and a comparison of the different fit approaches explained in Section 5.1.2. Furthermore, dark noise and LED based calibration results are compared and the temperature dependence of the target HV values is investigated. Additionally, the calibration settings are verified by investigating the gain at the target HV for three different temperatures.

5.2.2.1 Reproducibility of Calibration Results

The calibration using dark noise was performed twice at -30°C to investigate the reproducibility of the target HV. The results using the Poisson likelihood fit for both runs can be seen in

Figure 5.10 (left). All target high voltage values satisfy the FAT requirement. This means that all voltages are in the expected range between 79 V and 112 V. In addition, a histogram containing the deviations of the target HV between the runs is shown in Figure 5.10 (right). Calibration run 1 is used as reference. The mean difference of the target HV values and the corresponding standard deviation are (0.008 ± 0.140) % with a median of -0.002 %. The calibrations are compatible with each other and are thus reproducible.

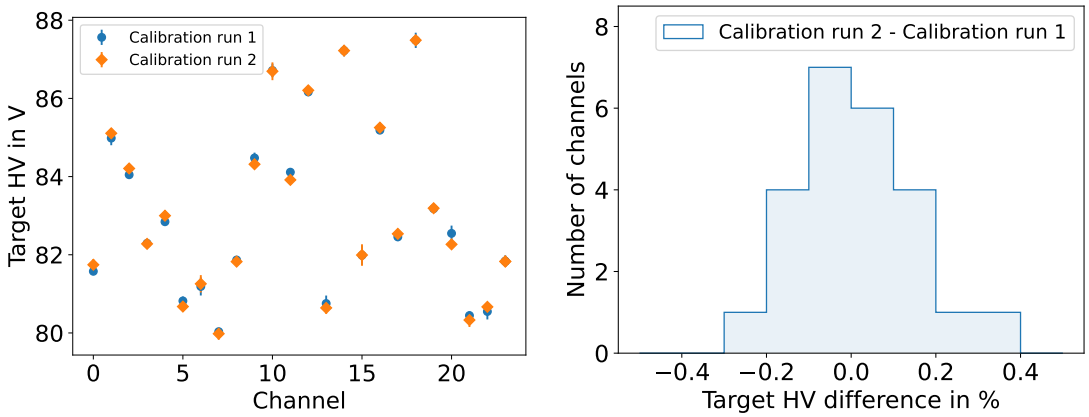

Figure 5.10: Results of two calibration runs at -30°C using Poisson likelihood SPE fits. Left: Absolute values in dependence of the channels. Right: Histogram of deviations between the runs in percent. The verification of calibration run 1 is used as reference.

Before this calibration is used in an actual measurement, it must be ensured that the selected target high voltage does indeed yield a gain of $5 \cdot 10^6$. Thus, a verification of the calibration must be performed. For this, the HV value obtained in the calibration is set and a dark noise based SPE charge spectrum is recorded using the discriminator trigger. Then, the gain is determined from the SPE peak position. In this case, the maximum likelihood fit is used. The results of the verification for both calibration runs are shown in Figure 5.11.

The deviations from target gain are below 5 % in almost all channels and are therefore consistent with the corresponding calibration (cf. Chapter 5). The mean, median and σ of the distribution of gain deviations from the target gain are provided in Table 5.3. In both calibration verification runs, the average gain of the channels is slightly below the target gain. This might be caused by an insufficient HV stabilization during the verification measurements which could be investigated in future measurements.

Table 5.3: Statistical measures for deviations from target gain for the verification of two calibration runs at -30°C.

Verification of calibration run	Mean in %	Median in %	σ in %
1	-1.12	-0.13	3.37
2	-0.93	-0.78	1.61

One outlier is observed during the measurements. This is channel 19 in the verification of calibration run 1. For this channel, only one data point is displayed in Figure 5.11 (left).

The fit for this channel yields a low gain of approximately 4.2. This corresponds to the outlier visible in the histogram, i.e. Figure 5.11 (right). The target HVs between the two calibrations deviate by only 0.01 %. It is not expected that this small deviation in target HV leads to the large observed deviation in gain. In channel 19, low gains were also observed in further measurements. These measurements and this behavior will be investigated in more detail in Section 5.2.2.4.

The longer-term stability of the gain with constant HV settings will be discussed in Chapter 7 for mDOM_D115_v1.

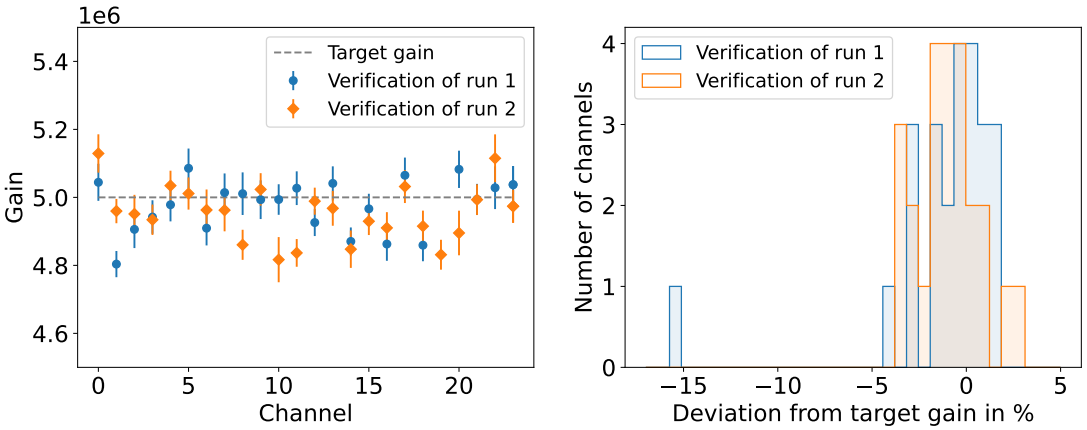

Figure 5.11: Verification results for calibrated HVs from two dark noise based calibration runs at -30°C. Left: Absolute values in dependence of the channels. Right: Histogram of deviations from the target gain.

5.2.2.2 Comparison of Fit Approaches

The calibration results for the same data sets at -30°C for both fit approaches are shown in Figure 5.12. All target high voltage values satisfy the FAT requirement. Differences between the two fit approaches are observed. In almost all channels, the likelihood fit approach yields higher voltage values than the convolutional fit. This hints to a systematic effect originating from one of the used fits. This might be due to the inconsistency of the nPE determination in the convolutional fit explained in Section 5.1.2.2, or the difference in the description of the lower charge region. For the Poisson likelihood fit, the poorly amplified electrons are modeled by an exponential function with an error function cutoff (see Section 5.1.2.1). In contrast, the poorly amplified electrons are modeled using a Gaussian with an error function cutoff (cf. Section 5.1.2.2).

In general, the mean difference between the fits is 0.35 % with a standard deviation of 0.28 %. Using the relation described in Equation 5.8 for an average power law function, the target HV deviation leads to an expected gain deviation of $(2.5 \pm 2.0)\,\%$ between the fits. This deviation is still in the required calibration precision Chapter 5, but the systematics should be investigated in more detail in the future.

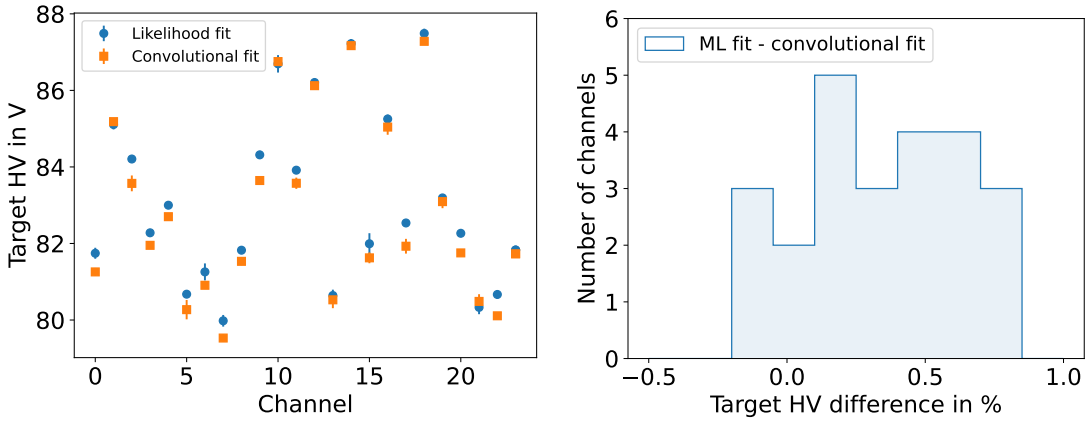

Figure 5.12: Results of gain calibration at -30°C for maximum likelihood and convolutional SPE fits. Left: Absolute values in dependence of the channels. Right: Histogram of deviations between the different fit methods. The results of the maximum likelihood fit are used as reference.

5.2.2.3 Temperature Dependence of Target HV

The dark noise calibration was performed for three different freezer temperatures, i.e. -10°C, -20°C and -30°C. These temperatures are expected to be reached in the ice at different deployment depths [72]. The warmer temperature corresponds to a deeper deployment region. This is due to the geothermal heat from below and the isolating effect from the ice above.

The calibration results at the different temperatures for 5 different channels are shown in Figure 5.13. The convolutional approach was used to fit the individual SPE spectra. The observed target HVs depend on the temperature. The higher the freezer temperature, the higher the target voltage value. This means, that the gain decreases with increasing temperature and therefore, a higher HV setting is necessary. This is consistent with observations from other measurements [73]. A hypothesis for this observation is a temperature dependency of the mean free path of the electrons within the dynode material [73]. When the temperature increases, the mean free path of the electrons decreases, leading to more scattering and energy loss of the electrons. Less electrons then have sufficient energy to escape the material. This reduces the dynode yield and therefore the overall PMT gain.

A linear function is fitted to the individual channel data. Considering all 24 channels, a minimum slope of $(0.03 \pm 0.01)\ \frac{\mathrm{V}}{^\circ\mathrm{C}}$ and a maximum slope of $(0.08 \pm 0.008)\ \frac{\mathrm{V}}{^\circ\mathrm{C}}$ is observed with an average of $(0.05 \pm 0.01)\ \frac{\mathrm{V}}{^\circ\mathrm{C}}$. An overall approximate value, e.g. the average slope of all channels, can be used to estimate an improved scan range of HV values during calibration as mentioned in Chapter 5 using test data from FAT and the PMT tests at different temperatures. Repeating this measurement at additional freezer temperatures will most likely improve the overall estimation of the HV temperature dependence. It will then be possible to describe the dependence by an empirically tailored fit function instead of a default linear fit as used in this analysis.

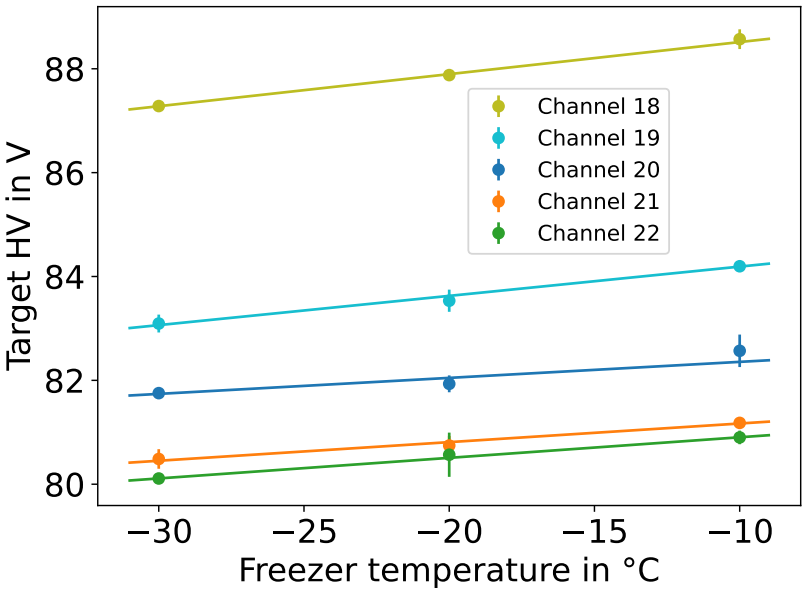

Figure 5.13: Temperature dependence of target HV values using convolutional fit for 5 different PMT channels. For each channel, a corresponding linear fit is performed and included.

5.2.2.4 Calibration Verification at Different Temperatures

At all investigated temperatures, a verification of the calibrations are performed. In this section, verification data is obtained based on the settings obtained using the maximum likelihood fit. Therefore, the data is also fitted using the likelihood approach. This allows to investigate the self-consistency of the calibration method using the likelihood fit. The verification of the calibration based on the convolutional fit is discussed in Chapter 7 for mDOM_D115_v1 in the frame work of a long-term monitoring.

The verification gain results for freezer temperatures of -10, -20 and -30°C are shown in Figure 5.14. The corresponding statistical measures for the deviations from the target gain are displayed in Table 5.4 for all temperatures. On average, the observed gains are slightly above the target gain for the verification at -10°C, while the gains tend to be below the target gain for the measurements at -20°C and -30°C. In total, almost all observed gains deviate less than 5 % from the target gain at all temperatures and are therefore acceptable. The dark noise based calibration routine is considered to be sufficiently precise at all investigated temperatures.

Table 5.4: Statistical measures for deviations from target gain for the verifications at -10°C, -20°C and -30°C.

Freezer temperature in °C	Mean in %	Median in %	σ in %
-10	1.70	1.53	2.63
-20	-0.6	-0.50	1.46
-30	-0.93	1.61	-0.78

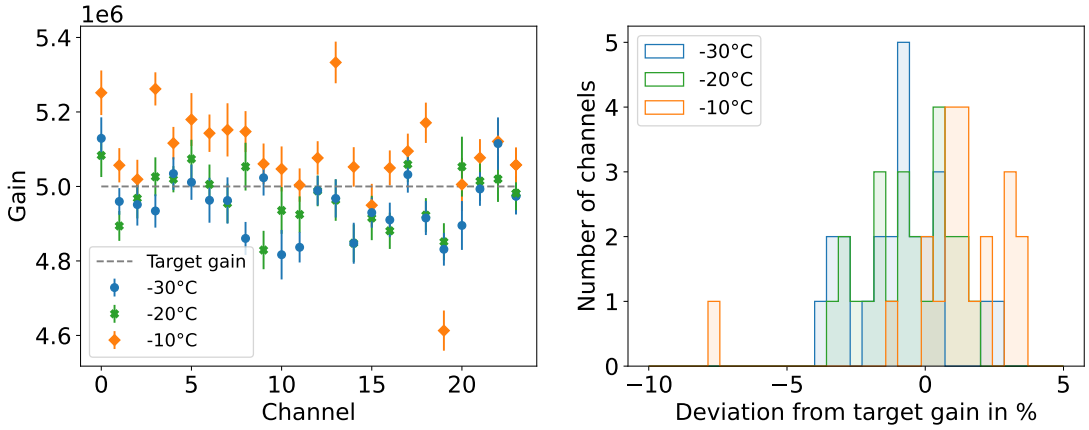

Figure 5.14: Verification of calibration results both obtained using the maximum likelihood fit approach. Left: Absolute values in dependence of the channels. Right: Histogram of deviations from the target gain at -10°C and -30°C.

The only outlier is again channel 19 observed at -10°C. The SPE charge spectra and corresponding fits for channel 19 at -10 and -30°C are displayed in Figure 5.15. By eye, the spectra at both temperatures look similar, especially the falling edges between 1 and 2 P.E. are aligned. The second data point however has a higher count at -10°C than at -30°C. It is possible that this slightly higher count at this charge pulls the Gaussian, describing the SPE peak, to the left, leading to the observed lower gain in the verification. Thus, the lower verification value might not be observed due to an actual much lower gain at -10°C but due to the fit itself. For this maximum likelihood fit, a description of the higher PE component should be implemented in general. This might minimize the pull by the lower charge region as more features of the whole spectrum will be considered.

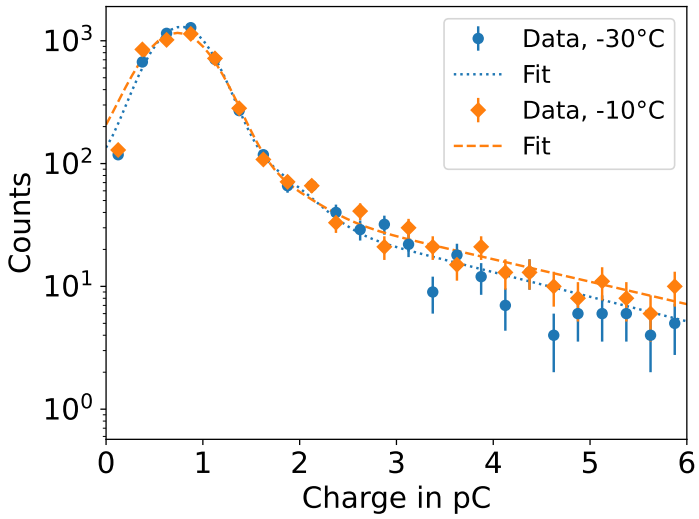

Figure 5.15: SPE charge spectra for channel 19 at -10 and -30°C. The HV of the PMT is set to calibrated values using dark noise spectra. The shown fits are maximum likelihood fits.

5.2.2.5 Comparison of LED and Dark Noise Based Measurements

It is expected that the dark noise based gain calibration is equivalent to the LED based measurement. Therefore, it is important to also compare the dark noise results to the results obtained using this light source. Thus, the gain calibration was performed using the flasher LEDs. In this case, the waveform readout was triggered by the flasher trigger, following the FAT procedure. A fixed binning for the SPE spectra was used, matching the approach for the dark noise maximum likelihood fit (cf. Section 5.1.2.1). The SPE spectra were fitted using the model described in Equation 5.1. Additional penalty terms as described in Section 5.1.2.1 for the dark noise fit are introduced. Furthermore, the same guess for the initial fit parameters was used, extended by the position of the pedestal at 0 P.E., its width of 0.1 P.E. and its amplitude as the maximum value. An example SPE spectrum with fit and the corresponding likelihood profile for the SPE peak position are shown in Figure 5.16.

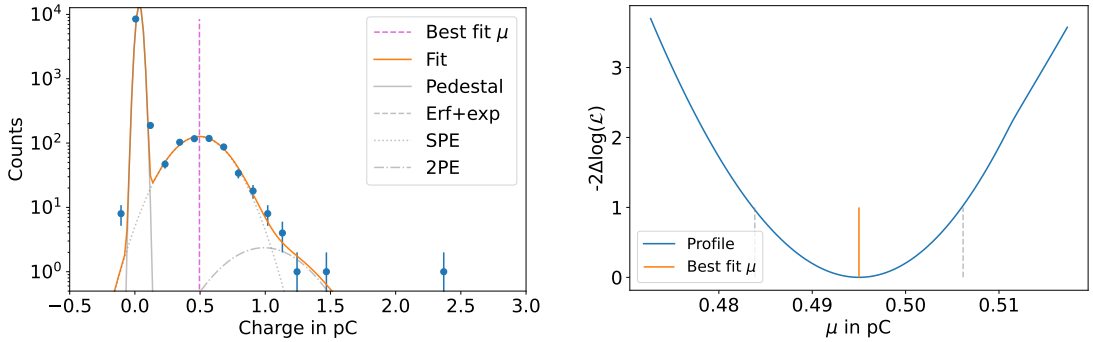

Figure 5.16: Left: LED generated SPE spectrum with Poisson likelihood fit at HV of 78 V. Right: Corresponding likelihood profile for the SPE peak position μ.

The results in comparison with the dark noise measurement are displayed in Figure 5.17. Both measurements were conducted at a freezer temperature of -20°C. For the dark noise measurement, the SPE spectra are fitted with both, the maximum likelihood approach as well as the convolutional fit. The LED fit failed for channel 15. Therefore, only 23 data points are included in Figure 5.17 for the LED based measurement.

In Figure 5.17, some systematics seem to be present, as the LED based calibration yields higher voltage values than the dark noise measurement. The statistical measures of the deviation distributions are displayed in Table 5.5. The observed mean deviation of approximately 1 % between the target HV values is expected to lead to a deviation in gain of approx. 7 % (cf. Equation 5.8).

Table 5.5: Statistical measures for deviations of the dark noise results from the LED measurement. Both fit procedures are applied the dark noise data.

Dark noise fit approach	Mean in %	Median in %	σ in %
Convolutional	0.97	0.95	0.57
Maximum likelihood	0.74	0.76	0.44

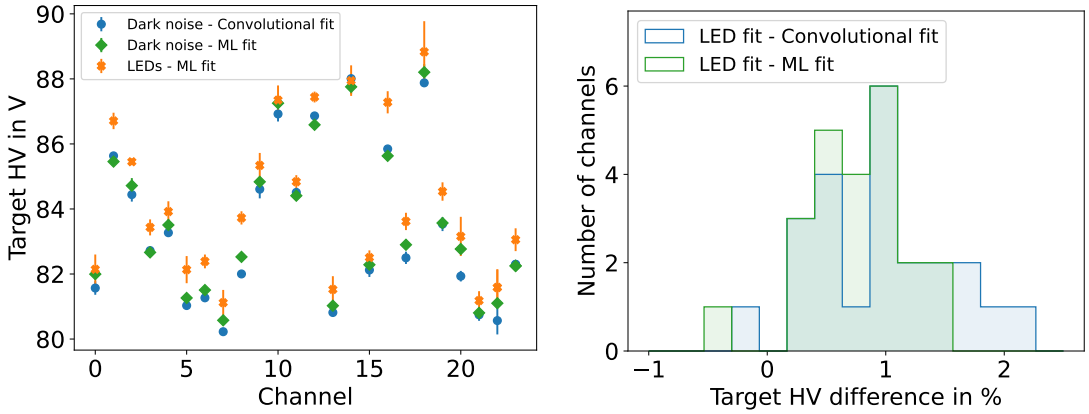

Figure 5.17: Results of gain calibration at -20°C for dark noise and LED based measurements. Left: Absolute values in dependence of the channels. Right: Histogram of deviations between different measurement types. The LED measurement is used as reference.

It is suggested that the LED measurement is repeated. It can then be investigated wether the observed systematic discrepancy between the dark noise and LED measurement is due to systematics in the fit itself or a more fundamental difference in the SPE spectra. For this measurement, the flasher trigger should still be used. Additionally, the discriminator should be set to the same value as for the dark noise-based measurement. Not only should the waveforms at the ADC be recorded, but also whether or not this waveform triggered the discriminator. This will result in two spectra: one containing all charges, and the other consisting only of charges that triggered the discriminator. The calibration analysis should then be performed using both spectra. Any observed differences in the target HV values can then be directly attributed to systematics of the fits as the charge spectra are not independent from each other.

All fit routines used in this thesis contain some minor inconsistencies in the implemented fit functions. This includes either not properly normalized components taken from `pmt_taco` or a slightly corrupted calculation of the nPE components as described in Section 5.1.2.1 and Section 5.1.2.2. Even though the dark noise based calibration routine is sufficiently precise, it is advised that the inconsistencies of the fit functions are removed and the accuracies of all measurements and fit procedures are investigated in more detail before used in-situ. Measurements with higher statistics can contribute to this goal.

6 Discriminator Threshold Calibration using Dark Noise

The discriminator trigger will be used for the in-situ waveform readout of IceCube Upgrade modules (cf. Section 4.3). This trigger initiates a readout if the incoming PMT signal is above a certain set reference value, the discriminator threshold. The target threshold is chosen such that the acquisition of pure noise waveforms is suppressed without filtering reasonable signals. For the IceCube Upgrade, a 50 % trigger efficiency at a pulse charge of 0.2 P.E. is defined as target threshold [4]. The corresponding reference voltage is set

by a DAC. As the baselines and noise levels vary between the PMTs, each discriminator threshold must be calibrated individually. In this section, method for the in-situ discriminator threshold calibration using dark noise is presented.

An alternative approach using the front-end test pulser was investigated in the scope of this masters thesis and is described in Appendix E. The general idea was designed within a DESY Summer Student project [74] and the procedure was improved and evaluated within the scope of this thesis. However, investigation of this approach was discontinued after a better-performing, dark-noise-based calibration routine was developed.

In the framework of the final acceptance testing for the mDOMs, the discriminator threshold calibration was performed using the flasher LEDs. This routine requires a fully functional flasher chain. An alternative approach developed within this thesis uses PMT waveforms induced by dark noise instead of LED light. This has the advantage that the underlying measurement can also be used for long-term monitoring of the discriminator threshold during the detector up-time. Thus, this alternative threshold calibration routine serves the same purpose as the gain calibration using dark noise described in Chapter 5.

6.1 Methods and Procedure

In this section, the general calibration routine is explained. The used trigger method and the trigger allocation are described. In addition, the calculation of the trigger efficiency curves required for the calibration are presented as well as the different fit approaches for the resulting threshold curves.

In this thesis, threshold fluctuations will be observed. The impact of such fluctuations on the detector performance and event reconstruction must be determined by simulations in the future. This was beyond the scope of this thesis.

6.1.1 General Calibration Approach

The general steps for the dark noise based threshold calibration are taken from the calibration routine using flasher LEDs developed for FAT [61]. An overview of the whole procedure is given in this section. The details of the individual steps are explained in the following sections. The improvements developed within this work and the differences to the FAT calibration are emphasized.

Overview of Calibration Routines using PMT Waveforms

For both routines, a certain range of discriminator DAC settings is swept through. The following procedure is performed at each threshold:

1. A full SPE charge spectrum is recorded using the flasher trigger for the LED based calibration or the ADC trigger for the dark noise based routine.

2. The information if the discriminator was triggered for a certain waveform is acquired. With this, a second spectrum containing only discriminator triggered charges is created.

3. The ratio of these spectra is calculated, determining a trigger efficiency curve.
4. An error function is fitted to the trigger efficiency curve.
5. The threshold in P.E. is defined as 50 % trigger efficiency level extracted from the fit.

The results obtained at all DAC counts are combined, creating a threshold curve. This curve contains the observed thresholds in P.E. in dependence of the DAC setting for the discriminator threshold. The target threshold setting is then extracted from the curve using a fit.

6.1.2 Discriminator Threshold Scan Range

In FAT, 10 discriminator thresholds are considered for the calibration routine. The initial investigated threshold corresponds to a voltage of 1 mV above the PMT baseline $T_{1\text{mV}}$. The respective threshold DAC setting is obtained using an `Iceboot`[1] function called `mDOMSetDiscriminatorThresholds()`. This function performs a binary search for the PMT noise level first, obtaining the corresponding DAC value, before calculating the required DAC setting of the discriminator [56].

$$\text{DAC threshold setting} = \frac{\text{Threshold in mV above PMT baseline}}{2.5\,\text{V}} \cdot 65536\,\text{DAC} + \\ + \text{PMT baseline in DAC.} \tag{6.1}$$

In this relation, 2.5 V is the dynamic range of the discriminator and the threshold can be set by a DAC with a resolution of 65536 counts.

The initial DAC threshold setting is then decreased stepwise by 10 DAC counts. This results in the following threshold scan interval [61]:

$$\text{FAT Threshold Interval} = [T_{1\text{mV}}, T_{1\text{mV}} - 100[. \tag{6.2}$$

As the threshold in DAC counts is decreased, the observed threshold in P.E. is increased.

In this work, it was observed that the scan range defined in FAT does not necessarily reach the target threshold of 0.2 P.E. Thus, the threshold interval was adjusted within this thesis. The improved scan range used in this work is given by:

$$\text{FAT Threshold Interval} = [T_{1\text{mV}} + 15, T_{1\text{mV}} - 40[. \tag{6.3}$$

The step size is decreased to 5 DAC counts, leading to a total number of 11 investigated threshold settings.

6.1.3 Trigger Methods and Allocation

For a discriminator threshold calibration using PMT waveforms, a trigger is required that is distinct and independent from the discriminator trigger. In this section, the trigger methods used for the threshold calibration routine both using LEDs and dark noise are described in

[1] Documentation of Iceboot. IceCube internal. Accessed: 27.11.2025.

more detail. Furthermore, it is explained how a trigger is assigned to a signal peak in a waveform.

Trigger Method

In FAT, the waveform readout is synchronized with the flasher LEDs using the calibration trigger. This approach will also be used in this thesis to compare the calibration results of the different routines.

For the dark noise based threshold calibration developed in this thesis, the ADC trigger is used. For this trigger, a signal must reach or fall below a certain predefined ADC value to initiate a readout. The goal for this trigger is to generate a charge spectrum that is equivalent to an SPE spectrum.

Most spectra used in this thesis were generated using a combination of two different ADC thresholds, corresponding to settings of 2 ADC counts and 3 ADC counts below the baseline of the signals. This reduces the amount of waveforms that do not include a reasonable signal. However, there is a minority of spectra that include a component generated with an ADC threshold set at 1 ADC count below the baseline.

In Section 6.2.1, it is investigated in detail if such a trigger approach introduces a bias into the discriminator threshold calibration.

Trigger Allocation

For the discriminator threshold calibration, the information if a certain PMT signal triggered the discriminator or not is required. In FAT and in this thesis, the "discWords" array explained in Section 4.3 is used. This array stores the discriminator response.

In FAT, a signal, i.e. the largest peak within a waveform, is considered to be triggered by the discriminator in case the corresponding "discWords" array contains a non-zero entry. This is independent of the trigger position within the array. For this approach it is assumed that the largest pulse in the waveform is the discriminator triggered signal. However, this assumption might bias the discriminator threshold calibration result.

Therefore, in this thesis, the trigger allocation was based on the actual positions of the signal peak in the waveform and the discriminator trigger. A signal is only considered to be discriminator triggered in the case that the trigger occurs in proximity of the integrated waveform pulse. This means that the trigger must occur in an interval of 10 bins before and one bin after the minimum of the signal peak. This is an empirical interval which should be adjusted based on a more systematic investigation of typical distances between discriminator triggers and signal peaks in the future.

6.1.4 Trigger Efficiency Curves

As mentioned before, the goal for the discriminator threshold calibration of the mDOM is to reach a 50 % discriminator trigger efficiency at a charge of 0.2 P.E. Thus, for each

set discriminator threshold in DAC during the calibration, the charge at the 50 % trigger efficiency must be obtained.

Determination of the Trigger Efficiency Curve

This trigger efficiency at a certain pulse charge q is defined as:

$$\text{trigger efficiency}(q) = \frac{\#\,\text{discriminator triggered waveforms}(q)}{\#\,\text{acquired waveforms}(q)}. \tag{6.4}$$

A trigger efficiency curve in dependence of the charge can therefore be determined by calculating the binned ratio of the histogram containing the discriminator triggered charges and the SPE charge spectrum containing all ADC-triggered charges. In Figure 6.1, an example for both histograms as well as the corresponding trigger efficiency curve is shown. This approach was taken from FAT.

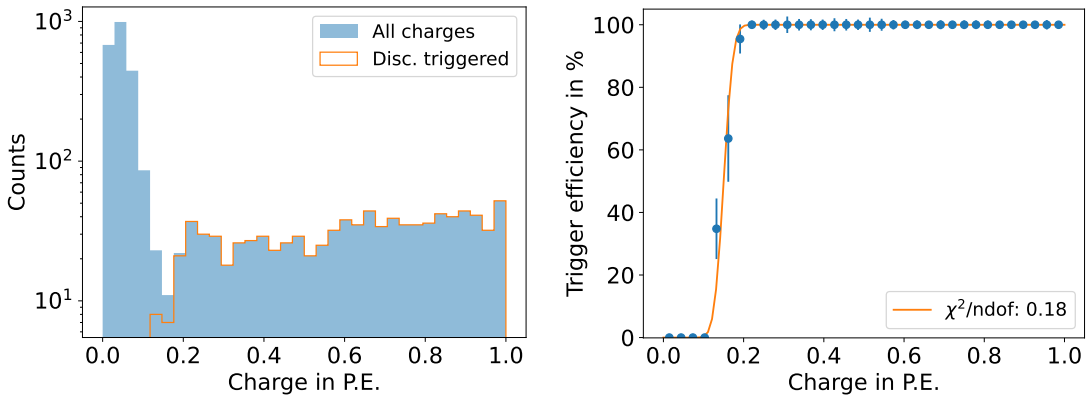

Figure 6.1: Left: Histograms containing all charges (SPE spectrum) and only discriminator triggered charges. Right: Corresponding trigger efficiency curve with error function fit.

Fit and Uncertainties of the Trigger Efficiency Curves

In FAT, the uncertainties of the trigger efficiency values are neglected and a sigmoid function is fitted to the trigger efficiency curve. The charge at the 50 % trigger efficiency level is defined by the center of the function. This value is a fit parameter and therefore directly returned by the fit. However, this assumes that the trigger efficiency curve covers the full range from 0 % to 100 %. Only in this case does the charge at the 50 % trigger efficiency level correspond to the position of the center of the function.

In this thesis, the uncertainties of the trigger efficiencies are considered. The obtained trigger efficiencies follow a binomial distribution [75]. Therefore, the uncertainties can be represented by 1σ Jeffreys intervals, which are described in Appendix D in detail. These intervals are typically asymmetric. However, the used optimizer `scipy.optimize.curve_fit` expects symmetric uncertainties as error bars. Therefore, Jeffreys intervals must be symmetrized before they can be used in the fitting process. The most conservative option to estimate the uncertainties is to choose the limit furthest from the considered data point and to apply

the difference between the data point and the limit as uncertainty in both directions. A less conservative approach is to calculate both, the upper and the lower limit of the interval. In this case, half the difference between these values is considered as symmetric uncertainty.

An error function is then fitted to the trigger efficiency curve. The charge corresponding to the 50 % trigger efficiency level, i.e. the threshold in P.E., is determined by the inverse of the error function instead of the center of the function. The overall uncertainty of the extracted charge value is calculated using Gaussian error propagation including the covariance of the obtained fit parameters.

The definition of the uncertainty of the individual trigger efficiency data points was found to be negligible in the final extracted threshold in P.E. In this thesis, the considered uncertainties are calculated using half the width of Jeffreys interval. In case a more precise determination of the uncertainties is of interest, an optimizer accounting for asymmetric uncertainties should be chosen.

6.1.5 Threshold Curves and Fit Methods

The collected thresholds in P.E. in dependence of the set DAC values create a curve referred to as threshold curve. The target DAC setting will be extracted from a fit describing the curve.

In FAT, a linear fit is used [61]. This assumes an ideal system. In an ideal discriminator that is set by an ideal DAC, the applied reference voltage depends linearly on the set DAC value. Furthermore, the charges of the pulses show a linear dependence on the size of the leading edge of the pulse. Thus, a linear dependence of the threshold in P.E. on the set DAC value is expected.

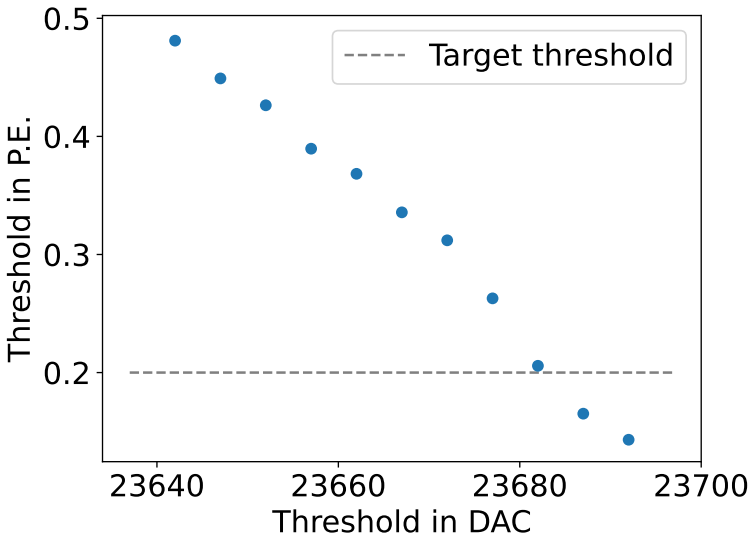

Figure 6.2: Threshold curve for dark noise based calibration with non-linear behavior. Uncertainties are included in but are smaller than the marker.

However, as shown in Figure 6.2, the typical threshold curve observed in these measurements is non-linear. In the future it should be investigated in more detail if the used error function fit is ideal to describe the trigger efficiency curves. The shape of the underlying SPE spectrum might affect the shape of the trigger efficiency curve and with this the extracted 50 % trigger efficiency level. This hypothesis was however not proven within this thesis.

In this thesis, different empirical fit methods for the threshold curves were investigated instead. The first approach is the same as in FAT, using a single linear function. The second approach uses an iterative, multi-linear fit approach describing the lower charge data points. In this fit, outliers in the lower charge region will lead to an inappropriate fit and a deviation between the extracted threshold value and the target. To avoid this, a third option is to fit a third degree polynomial to the data to adapt for the observed non-linearities.

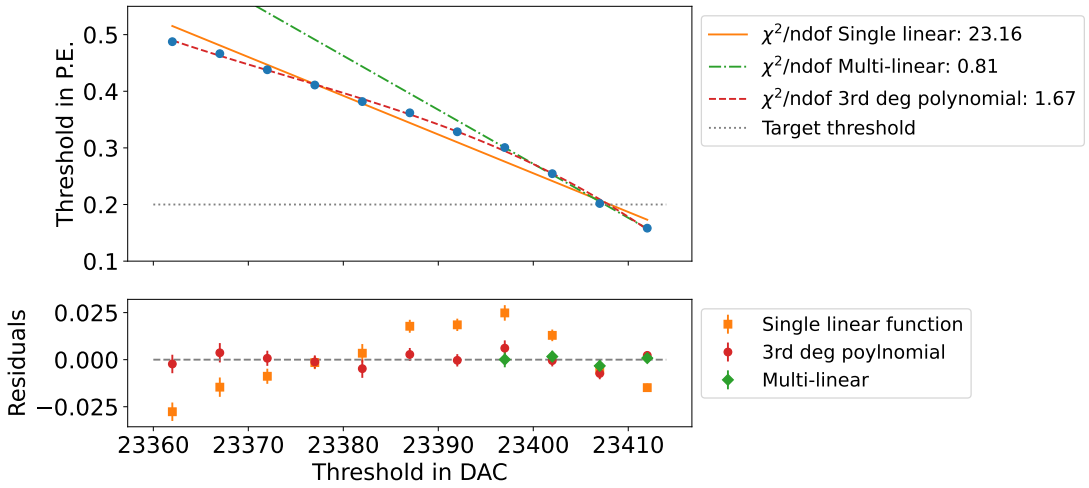

Figure 6.3: Example threshold calibration curve. Included are three different fit methods. The residuals are the absolute differences between the data points and the respective fit function.

An example for all three fits with the corresponding reduced χ^2 values are shown in Figure 6.3. In general, the polynomial fit of third order is preferred for the dark noise based threshold calibration routine. The goodness of the polynomial fit is always better than the goodness of the single linear fit. Additionally, the third degree polynomial fit considers all collected data points and avoids bias induced by outliers in the lower charge region. However, the multi-linear fit was used for the threshold calibration in earlier measurements conducted in the framework of this thesis. It was later fully replaced by the polynomial fit approach. The fit approaches used for the evaluation of the individual calibration runs throughout this thesis will be mentioned when the corresponding results are discussed.

6.2 Analysis and Results

In this section, the results of the discriminator threshold calibration routine developed within this thesis are discussed. This includes the investigation of potential bias introduced by the use of the ADC trigger and the selection of the fit model for the calibration evaluation. The reproducibility of the calibration results is investigated before the dark noise based calibration results are compared to the LED based results.

6.2.1 Bias Study for ADC Triggered Dark Noise Waveforms

For a suitable threshold calibration using dark noise, it must be ensured that the used trigger does not introduce a bias in the measured efficiency curve of the discriminator. In theory, each data point contributing to the obtained trigger efficiency curve using the ADC trigger is described by a conditional probability $P(disc|ADC)$ [75]. This means that the information if the discriminator was triggered is only recorded under the condition that the waveform was readout using the ADC trigger. This probability can be written as:

$$P(disc|ADC) = P(disc) \cdot \frac{P(ADC|disc)}{P(ADC)} \tag{6.5}$$

In this equation, $P(disc)$ describes the probability that a waveform is triggered by the discriminator. This is the quantity of interest. The factor $\frac{P(ADC|disc)}{P(ADC)}$ includes the probability that a waveform is triggered by the ADC under the condition that the discriminator is triggered ($P(ADC|disc)$) and the probability that a waveform is triggered by the ADC ($P(ADC)$). This factor might introduce an unwanted bias in the observed trigger efficiency curve if it is unequal to 1. In contrast, the recorded trigger efficiency curve is unbiased if $\frac{P(ADC|disc)}{P(ADC)} = 1$ as then $P(disc|ADC) = P(disc)$ holds. This is especially the case when $P(ADC) = 1$, meaning that the ADC trigger is fully efficient at a certain pulse charge independently of the discriminator trigger, implying $P(ADC|disc) = 1$. Thus, the trigger efficiency curve is unbiased in case the ADC trigger is fully efficient.

The trigger efficiency of the ADC was investigated using the front-end test pulser. This pulser is described in Section 3.3 in more detail. The apparent test pulser pulse height was set to values between 2 and 8 ADC counts. According to the measurements described in Section E.1.2, these pulse heights correspond to observed charges between approximately 0.05 and 0.2 P.E. equivalents. For each of the test pulser settings, the ADC threshold is set to 3 ADC counts below the baseline of the waveform. For each channel, 1000 test pulser pulses are generated and the ADC scaler rates, counting ADC threshold crossings, are recorded. The trigger efficiency is then calculated by the ratio of the observed ADC scaler rate and the total number of generated pulser pulses. This measurement is repeated 5 times per channel.

The average trigger efficiency curve of all channels and repetitions is shown in Figure 6.4. The uncertainties are the standard error of the mean of the observed trigger efficiency values. The ADC trigger can be considered fully efficient down to pulse heights of 4.5 ADC counts, i.e. pulse charges of approximately 0.1 P.E. equivalents.

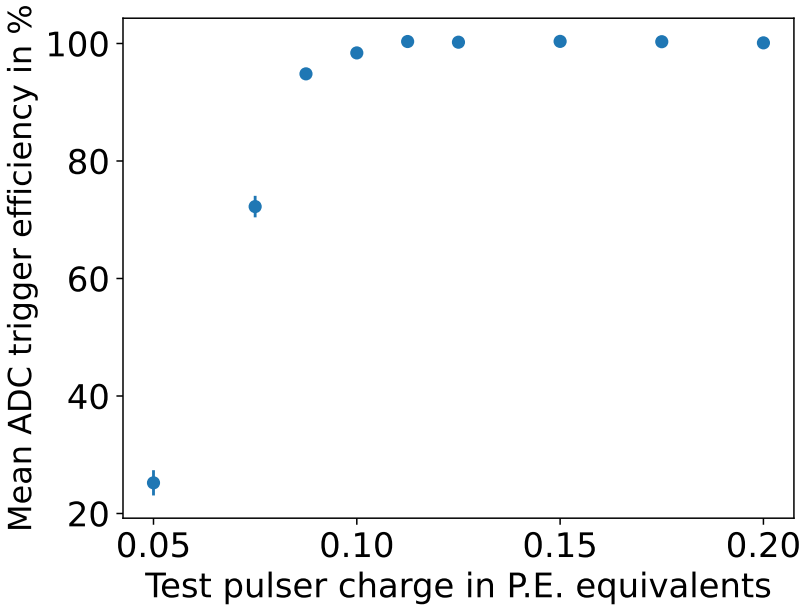

Figure 6.4: ADC trigger efficiency curve at ADC threshold 3 ADC counts below waveform baseline. The results are averaged over 5 repetitions and all channels. Uncertainties on trigger efficiency values are the standard error of the mean.

In Figure 6.5, two typical trigger efficiency curves occurring during the dark noise based threshold calibration are shown, one close to the target threshold and one at a lower charge. A vertical line represents a charge of 0.1 P.E. where the ADC trigger is still fully efficient. This indicates, that all data points in the region of interest fall into the charge regime where the discriminator trigger efficiency curve is unbiased. A potential bias only affects the data points at the very low charge region where the discriminator efficiency is close to zero. It is assumed that the effect of a bias at these low charges can be neglected and the observed discriminator trigger efficiency curves can be regarded as unbiased in terms of the presented threshold calibration routine. However, data points in the resulting threshold curves with thresholds below 0.1 P.E. should not be considered during the calibration routine, as this might lead to a bias.

To show experimentally that the ADC trigger does indeed not lead to a bias in the observed threshold curves, the dark noise based threshold calibration was repeated using forced triggered data for one exemplary channel. For this measurement, the calibration trigger implemented in the `Iceboot` software was used. This trigger reads out waveforms with a fixed frequency and is in principle the same trigger used with the flasher LEDs. However, for this measurement the flasher chain was not supplied with voltage ensuring that the LEDs were turned off.

In Figure 6.6, the threshold curves for the routines using the ADC trigger and the calibration trigger, i.e. the forced trigger, are shown. The observed threshold curves are similar for both triggers. This confirms the assumption that no bias is present in the ADC triggered data. The forced trigger based measurement is fundamentally unbiased, but the number of noise waveforms in the pedestal is increased with respect to SPE spectra triggered by the ADC.

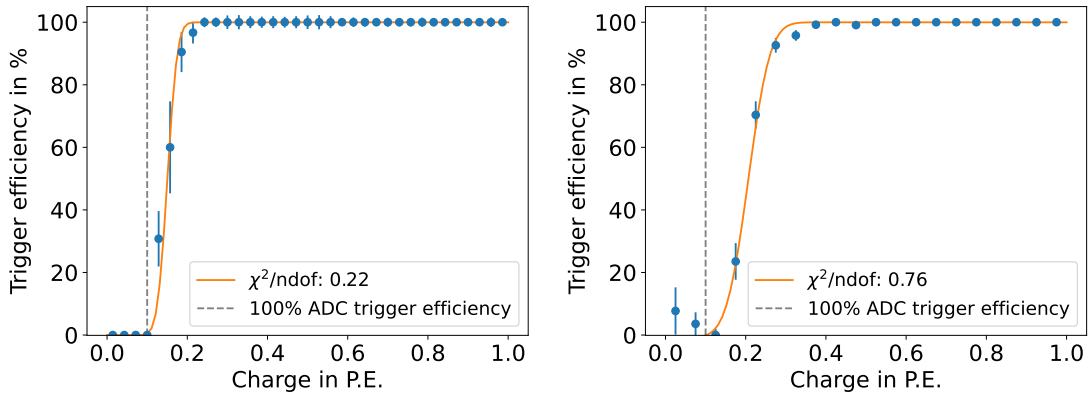

(a) Discriminator threshold at low charge in dark noise measurement.

(b) Discriminator threshold close to target charge in dark noise measurement.

Figure 6.5: Typical discriminator trigger efficiency curves occurring during dark noise based threshold calibration. Left: low charge at 50% trigger efficiency. Right: charge close to calibration target. Vertical lines show charge down to which the ADC trigger is fully efficient.

Thus, more waveforms must be collected until sufficient coverage in the region of interest, i.e., the region where the trigger efficiency transitions from 0% to 100% efficiency, is reached. However, since the ADC trigger was sufficiently unbiased, this approach was preferred over the forced triggered data acquisition in order to minimize the number of collected waveforms.

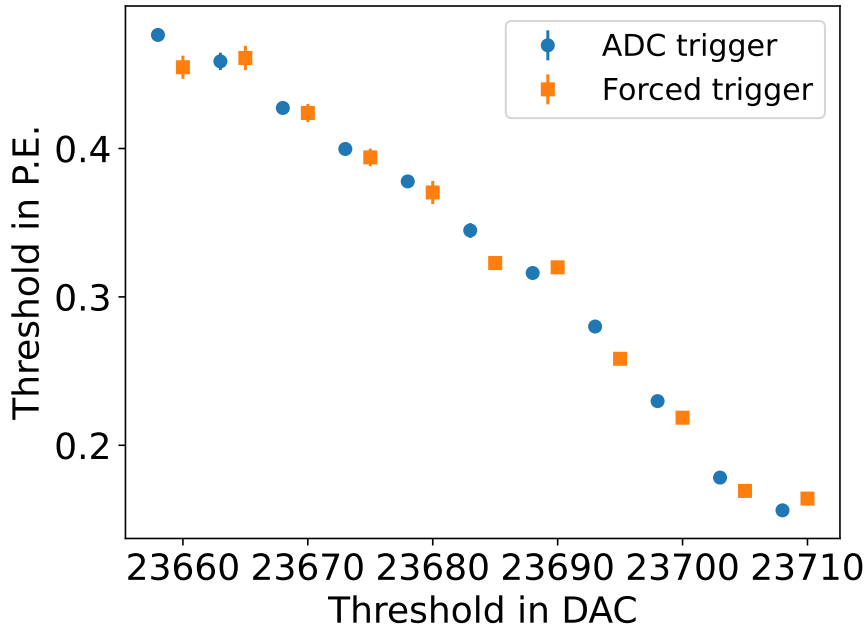

Figure 6.6: Example of threshold curves obtained from ADC and forced triggered dark noise data.

6.2.2 Discriminator Threshold Resolution

The resolution of the discriminator is estimated using the slope of the multi-linear fit explained in Section 6.1.5. This fit describes mainly the lower charge region around the target threshold and is used as a rough approximation of the discriminator threshold resolution. The mean slope m for all channels of one calibration run at room temperature is given by $m_{\text{multi-linear}} = (-0.010 \pm 0.002)\,\frac{\text{P.E.}}{\text{DAC}}$. Thus, it is assumed that deviations below 0.01 P.E. cannot be resolved using the discriminator DAC.

6.2.3 Dark Noise based Calibration and Verification

In this section, the calibration results for mDOM_D115_v1 at room temperature are described. Additionally, the calibration results are verified by measuring the threshold in P.E. at the calibrated threshold value.

Calibration Results

The calibration using dark noise was performed twice for mDOM_D115_v1 at room temperature. The high voltage was set to the same values throughout both calibration runs. For each run, the calibration was done channel by channel with a duration of approximately 17 min/channel for both calibrations.

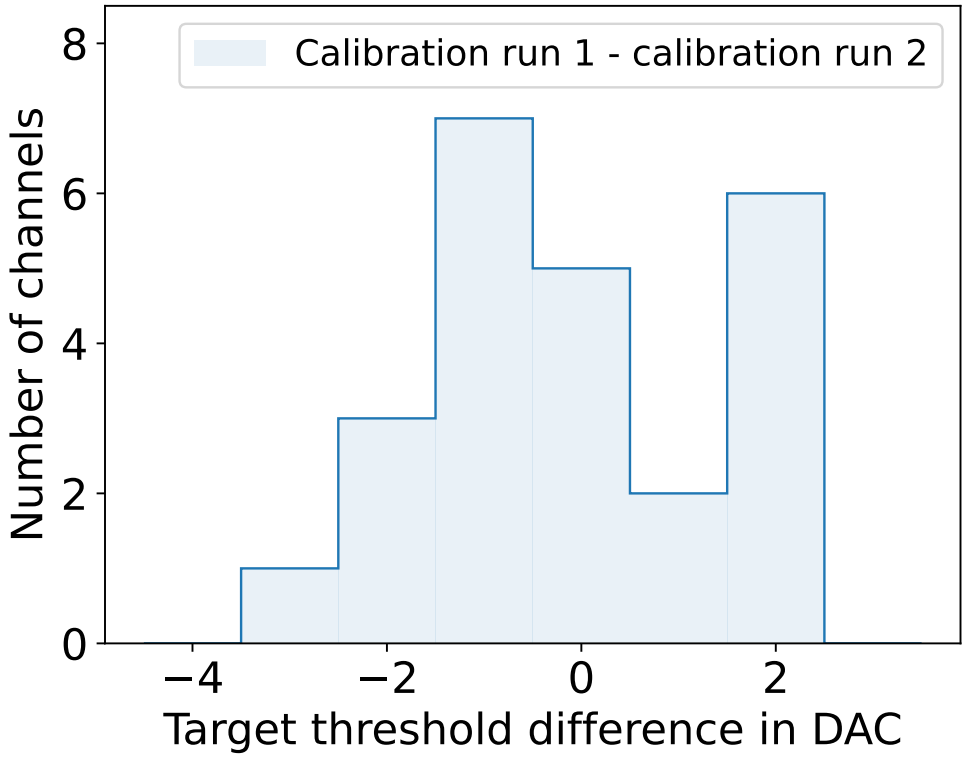

Figure 6.7: Comparison of target threshold values in DAC counts from two different calibration runs. Calibration run 1 is used as reference and the difference is defined relative to the corresponding value in each channel.

In Figure 6.7, a comparison between the target threshold DAC values is shown in reference to the values obtained in run 1. In this analysis, the threshold extraction from a third degree polynomial fit is used for both runs (cf. Section 6.1.5). The threshold difference is given in integer values as the discriminator threshold can only be set in integer steps. The mean difference between the target threshold settings is (-0.08 ± 0.30) DAC counts and is therefore interpreted as negligible. The temperature difference between the runs was small (0.6°C). The gain was not monitored throughout these measurements. An influence on the observed thresholds can therefore not be excluded.

The threshold calibration using dark noise was repeated at lower temperatures. The results for mDOM_D115_v1 at -20°C will be presented in Chapter 7.

Calibration Verification

It is necessary to verify that the calibrated threshold value leads to the target threshold of 0.2 P.E. To confirm the calibration, the discriminator threshold is set to the calibrated DAC value and a charge spectrum is collected using an iterative ADC trigger. This trigger routine should be the same as for the calibration routine. However, in the measurements presented here, the ADC thresholds were subsequently set to 2 and 4 DAC counts below the baseline of the signal. This was corrected in later measurements presented in Chapter 7. The final threshold in P.E. is extracted from the trigger efficiency curve as done for the threshold calibration.

In this analysis, the tested threshold values were extracted using the multi-linear fit approach. The used data was the same as in calibration runs 1 and 2 described above. A verification was performed once per calibration.

The verification results for both calibrations are shown in Figure 6.8. The corresponding mean, median and standard deviations are displayed in Table 6.1. The absolute deviations from the target threshold are small on average. Following this analysis at room temperature, the dark noise based calibration is able to achieve threshold settings close to the target threshold. As mentioned before, the impact of the observed threshold deviations on the event selection and reconstruction must be determined by simulations in the future.

Table 6.1: Statistical measures for the verification of two threshold calibration runs.

Calibration run	Type of distribution	Mean	Median	σ
1	Absolute values in P.E.	0.20	0.21	0.03
1	Relative deviation in %	-0.07	4.3	13.14
2	Absolute values in P.E.	0.21	0.21	0.02
2	Relative deviation in %	6	7	10

A detailed analysis of the verification of the calibration at -20°C is provided in Chapter 7.

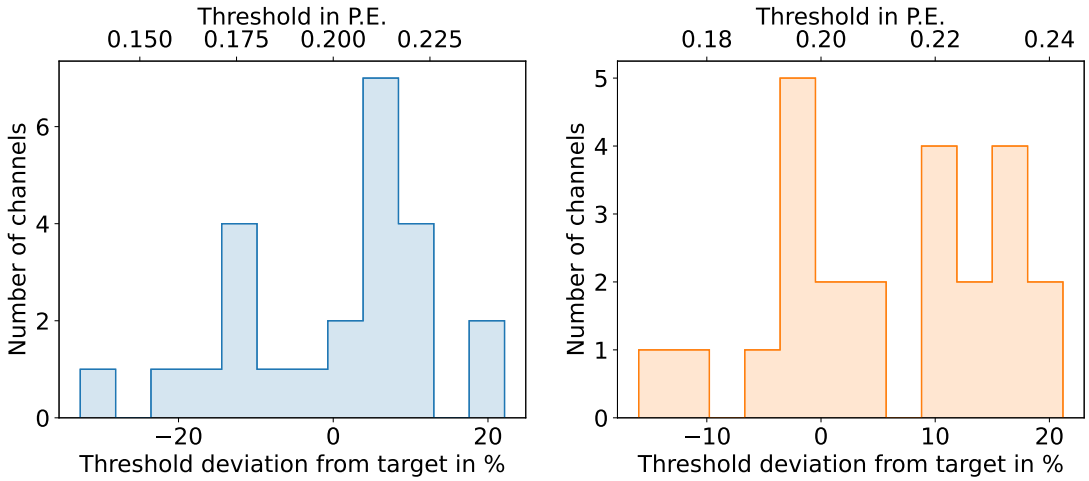

(a) Verification of calibration run 1.

(b) Verification of calibration run 2

Figure 6.8: Verification for the discriminator threshold values obtained in two different calibration runs. Absolute values and relative deviations from the target are considered. The measurements were conducted at room temperature.

6.2.4 Dark Noise - LED Calibration Comparison

In theory, it is expected that the calibration routines based on dark noise and flasher LEDs are equivalent to each other and therefore lead to the same results. To investigate the expected equivalence, the calibration is repeated using the flasher LEDs. Only odd channels, i.e. channels in the lower hemisphere of mDOM_D115_v1, could be considered due to a broken flasher chain in the upper hemisphere.

Initial Calibration Comparison

The flasher based calibration results using all LEDs are compared to the results of calibration run 2 using dark noise described in Section 6.2.3. In Figure 6.9, the threshold curves of the dark noise and flasher based calibrations are shown for two channels. For the channel in Figure 6.9 (left), the observed threshold curves for both methods match, but larger deviations are observed for the threshold curves displayed in Figure 6.9 (right) starting around 0.3 P.E. The observed thresholds in P.E. for the LED measurement drop faster than the corresponding values of the dark noise based calibration in this channel. This means, that the discriminator seems to trigger on smaller charges compared to the dark noise measurement. Therefore, the LED based calibration results in an overall lower DAC threshold at the target threshold in P.E.

Additionally, the flasher based calibration was repeated using only one LED at a time. With this approach only the channels located in proximity of the used LED can be calibrated. For example when LED 1 is enabled, only channels 3, 5 and 7 register a sufficient amount of reasonable signals due to the layout of the mDOM (cf. Figure 3.6). Channels 3, 9 and 21 are located close to two LEDs meaning that they are calibrated twice in this approach. In general, it is expected that the calibration results do not depend on the number of LEDs used, including the dark noise measurement. The results of the LED calibrations are shown

in Figure 6.10 in reference to the dark noise measurement.

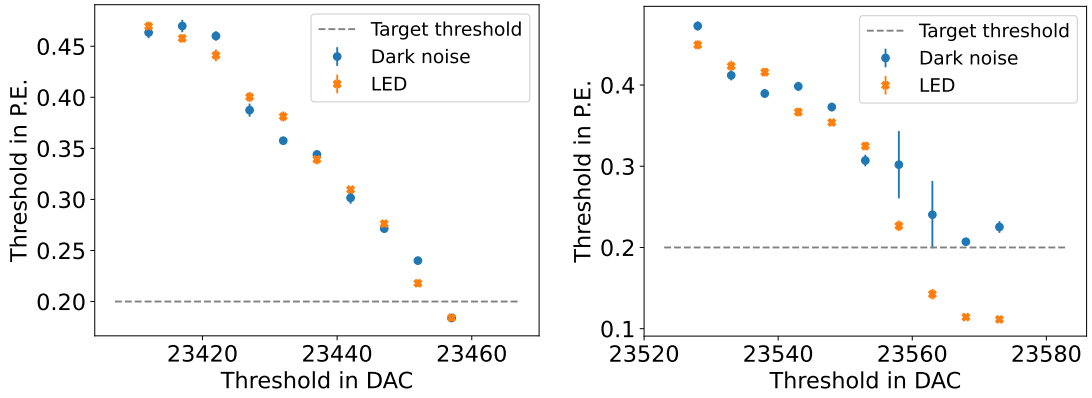

Figure 6.9: Examples for threshold curves obtained in flasher and dark noise based measurements. Left: Good agreement between calibration methods. Right: Larger deviations between calibrations.

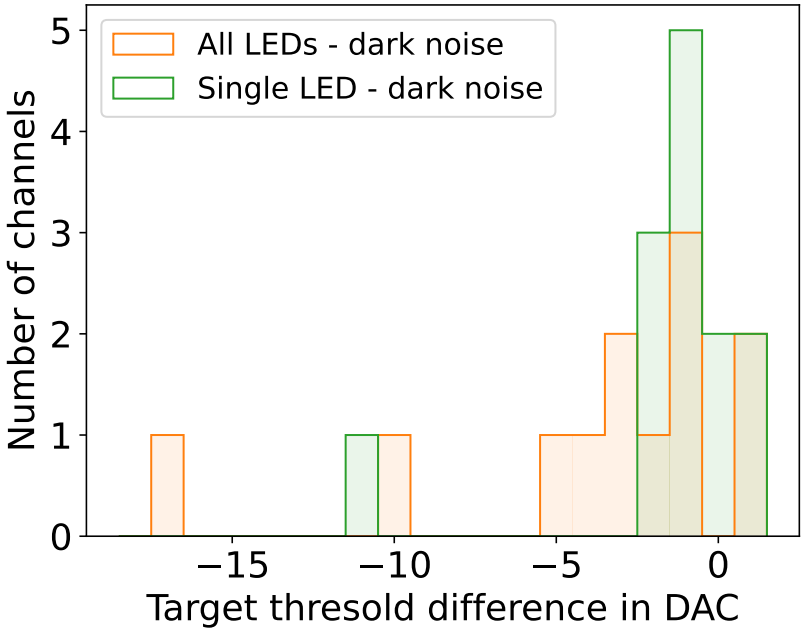

Figure 6.10: Calibration results using all bottom hemisphere LEDs, and only one LED at a time relative to the dark noise based calibration. The histogram for the single LED approach contains three additional results. Three of the channels are located close to two LEDs and can therefore be calibrated twice in the single LED approach.

The mean deviation between the calibration measurement considering all LEDs and the dark noise measurement is (-3.8 ± 1.4) DAC counts. The deviation between the single LED and dark noise calibration is (-0.9 ± 0.8) DAC counts. Thus, the uncertainty is minimized in the case that only a single LED is used.

Investigation of Calibration Deviation

In 2020, it was reported internally that the flasher trigger might introduce additional noise into the recorded waveforms [76]. Such ringing induced at the PMT base could lead to an additional trigger in the discriminator, and could therefore lead to a bias in the discriminator threshold calibration.

The discriminator response is studied in more detail to investigate the supposed ringing induced by the flasher trigger. For waveforms with charges below the expected discriminator threshold, it was observed that the discriminator response included triggers at the same position in 23 out of 24 investigated channels. A histogram of the number of triggers in dependence of the waveform bin observed in the full measurement of one example channel is shown in Figure 6.11. A total of 3338 waveforms was recorded of which 1016 have charges below 0.04 P.E. Two trigger distributions are visible in the histogram, one starting at waveform bin 49 and another one starting approximately at waveform bin 54. Almost all waveforms were triggered by the discriminator regardless of the charge observed at the ADC readout. Thus, even waveforms with charges below 0.04 P.E. were triggered. The trigger that starts mainly at waveform bin 54 is only present in waveforms that contain larger charges. Thus, it is assumed that the trigger at waveform bin 54 is induced by the actual PMT signal.

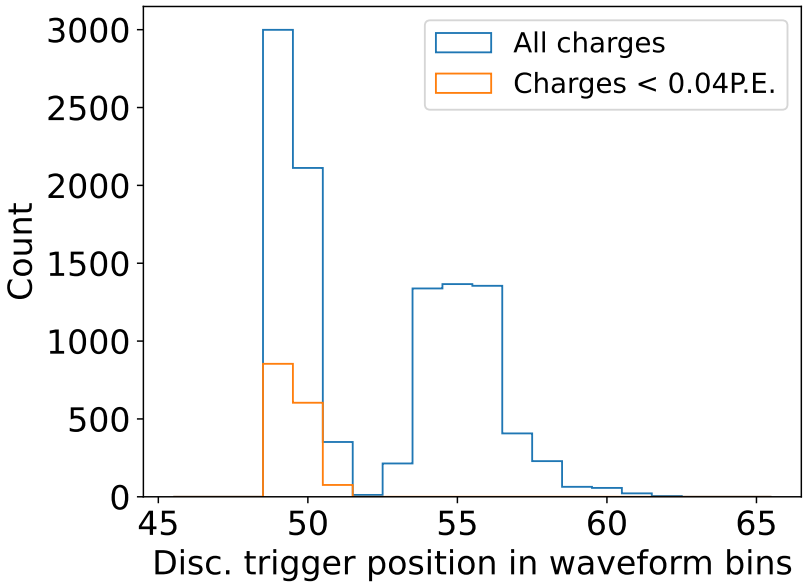

Figure 6.11: Histogram of discriminator trigger positions in waveforms of channel 1. The distribution for all charges is shown as well as a distribution for charges below 0.04 P.E. observed in the ADC readout. The histogram considered a total of 3338 waveforms with 1016 waveforms containing charges below 0.04 P.E.

In case that the excess trigger in waveform bin 49 is indeed due to ringing induced by the flasher trigger, it is expected that the time difference between the triggers corresponds to

the transit time of the PMTs. The potential ringing signal is induced into the PMT base directly, while the actual PMT pulse is formed within the PMT requiring the corresponding transit time [58]. The transit time of a PMT model similar to the one used in the mDOM is specified with 43 ns by Hamamatsu [77]. Assuming waveform bin 49 and 54 as main starting points for the discriminator triggers, the difference of 5 bins corresponds to approximately 41.7 ns. Thus, the observed distance between the triggers aligns with the transit time of the PMT. This result supports the hypothesis that the observed excess trigger is caused by ringing induced by the flasher trigger.

To visualize the ringing on the ADC waveforms, average waveforms were calculated for charges below 0.04 P.E. These waveforms typically do not contain a reasonable photoelectron signal. Examples of such average waveforms with all LEDs enabled can be seen in Figure 6.12 for several channels. Artifacts in the waveform at the same position are observed in almost all channels. This is consistent with the assumption that the flasher trigger introduces additional noise into the waveform. Before the noisy signal reaches the ADC readout, it passes through a pulse shaping chain smoothing out short noise pulses as described in Section 3.3.2. Thus, only smoothed artifacts of the flasher induced noise will be observed in the ADC. Therefore, it is likely that the pulse shaping chain introduces a discrepancy between the observed threshold at the ADC readout compared to the actual discriminator threshold.

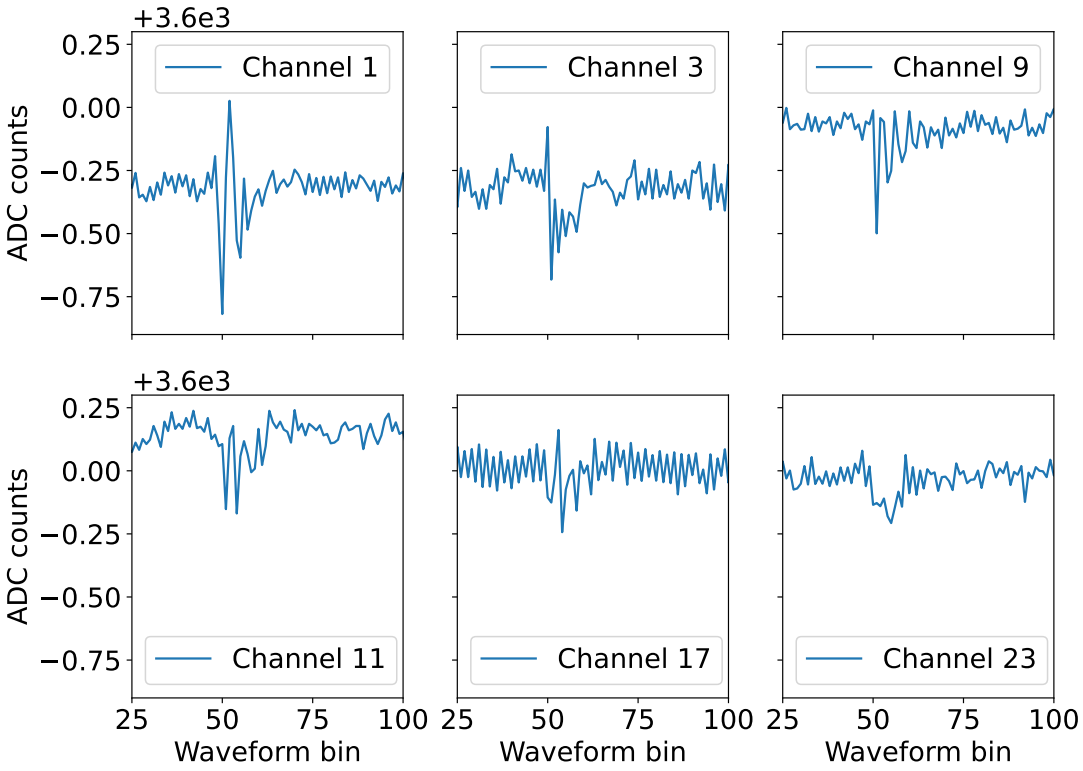

Figure 6.12: Average flasher generated waveforms with charges below 0.04 P.E. for a selection of channels.

Improvement of LED Calibration and Comparison

As the supposed false discriminator trigger induced by ringing is located always at the same position in the waveform, this can be used to mask the excess trigger. Thus, the corresponding entries in the discriminator response are replaced by 0. An improvement in the calibration agreement between dark noise and LED measurements is expected in case the excess trigger is the reason for the threshold discrepancy. The comparison of the calibration results using this filtering approach is shown in Figure 6.13. The mean difference between the calibrations using all LEDs and the dark noise based measurement is (-1.0 ± 0.6) DAC counts. The mean deviation of the single LED measurement from the dark noise based threshold calibration is (0.0 ± 0.4) DAC counts. Almost all data points are located within the fluctuation window observed between the dark noise calibration runs. Thus, the dark noise - flasher agreement is indeed improved for all channels. A larger difference between the usage of all LEDs and only a single LED is observed in one channel.

One outlier is observed in the threshold calibration using all flasher LEDs. In this channel, the single LED calibration is in good agreement with the dark noise measurement while the multi-LED result deviates further. It is not expected that this is an artifact of the false discriminator trigger. To draw a conclusive statement for this channel, further measurements are necessary. This could include repeated calibration measurements as a first step to investigate if the deviations are persistent.

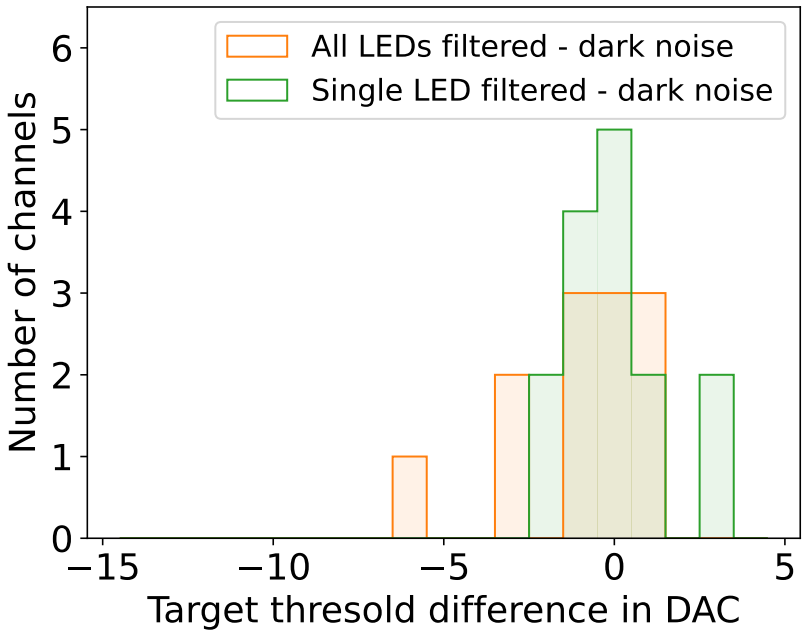

Figure 6.13: Calibration results with applied masking for suspected false trigger. Results for all bottom hemisphere LEDs and only one LED at a time relative to the dark noise based calibration. Additionally, the region in which calibration fluctuations were observed between dark noise runs is shaded. For channels 3, 9 and 21, two data points are present for the single LED calibration as these channels are located next to two LEDs.

In general, this analysis shows that an equivalence of the calibration methods can be expected when the false trigger observed in the LED based measurement is masked properly. The differences in the LED calibrations using one and all LEDs in one channel should be investigated in more detail before the LEDs are used for the threshold calibration in-situ.

Observing a false discriminator trigger induced by the flasher trigger indicates that it should be handled carefully in the future. Otherwise, a bias could be introduced to measurements requiring the flasher LEDs in combination with the discriminator response.

7 Long-term Monitoring using Dark Noise

For all physics experiments it is important to be aware of potential changes and drifts in the calibration of the setup. Additionally, unnecessary re-calibrations should be avoided, especially if experimental down-times are involved. Therefore, the knowledge of the timescales on which changes happen is crucial to determine the frequency of required calibration runs.

To investigate such changes in the PMT gain and discriminator threshold of the mDOM, a long-term monitoring of these properties was setup. For this, mDOM_D115_v1 was placed in a freezer at -20°C as described in Section 4.1. The dark noise based approaches developed within this thesis were used. The advantage of this dark noise approach is that it can also be used in-situ during the up-time of the detector.

7.1 Initial Calibration

The gain of the mDOM PMTs and the discriminator threshold were calibrated once using dark noise. The corresponding procedures are explained in Chapter 5 and Chapter 6. The convolutional fit described in Section 5.1.2.2 is used for the gain calibration.

The calibrations were performed during the day. It was later discovered that the initial setup was not fully light-tight. Thus, external light entered the setup and affected the shape of the SPE charge spectrum. As shown in Figure 7.1, the nPE component is systematically larger at night than during the day. The external light was dim enough to induce SPE-like signals, replacing part of the higher PE contribution from radioactive decays, changing the overall shape of the spectra.

Although an increased amplitude of the SPE peak could in principle improve the gain calibration, the fit model was optimized for spectra with a large nPE contribution. The changed spectral composition could therefore reduce the precision of the calibration. Additionally, at the time of the calibration, bins with less than 10 counts were still included in the fit. The corresponding cutoff was introduced only later for the data analysis in Chapter 5 and the analysis of the long-term monitoring data. Applying the cutoff to the gain calibration data would lead to failed fits in some channels due to too few considered bins.

After the change in spectral composition was traced back to light pollution in the setup, the freezer was covered with blankets to improve the light-tightness during the long-term monitoring (cf. Section 4.1). All monitoring data collected before the coverage of the freezer was discarded.

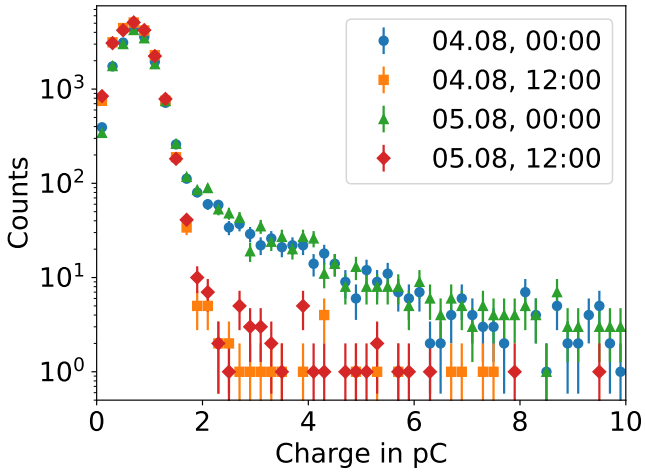

Figure 7.1: SPE spectra recorded during day and night using dark noise. The nPE contribution is persistently higher during the night.

7.2 Monitoring Tests and Schedule

The main tests implemented for the long-term monitoring are dark noise based verification measurements of the PMT gain and the discriminator threshold explained in Section 5.2.2.1 and Section 6.2.3. For each of this tests, environmental parameters such as the mainboard temperature and the pressure were collected. In addition, the HV monitored at dynode stage 10 was recorded. A larger change in these properties might have an impact on the observed gain and discriminator thresholds. For example, the temperature dependence of the gain was discussed in Section 5.2.2.3.

Furthermore, a third test was implemented, monitoring the dark rates at the calibrated gain and threshold settings. For each channel, the scaler rates are recorded. These rates are determined by the number of signals crossing the discriminator threshold in a certain time interval. A short integration time of 1 ms was used and the measurement of the scaler rates was repeated 5000 times per channel. The number of threshold crossings per integration period is low. For a future measurement, a longer integration time with less repetitions should be chosen to improve the statistics per recorded scaler rate. The scaler rates reported in this thesis are averaged over all 5000 trials in the individual channels. The corresponding uncertainties are the corresponding standard deviations, neglecting the underlying Poisson statistics.

For the long-term monitoring, all three tests are run every 12 hours, starting at noon and midnight.

7.3 Analysis and Results

In this section, the results of the long-term monitoring are presented. This includes the investigation of the precision of the underlying calibrations as well as the observed stability of the gain and the discriminator threshold.

7.3.1 Day - Night Differences of Dark Rates

The goal of the long-term monitoring is to investigate the internal changes in gain and threshold over time in a controlled environment. This means, that the environmental parameters such as the temperature and the pressure should be as constant as possible. In addition, the light pollution within the setup is required to be low and at least constant to ensure comparability between the individual measurements.

The dark rates collected in the measurements during the day and at night after coverage of the freezer are compared in Figure 7.2. For this, the median dark rate was calculated for the measurements at night and during the day in each channel. The difference normalized by the night time measurement is depicted in the histogram. A total of 41 measurements were considered for each time. A mean difference of (-2.6 $\pm$ 0.5) % is observed between the measurements at different times of the day with a median of -2.16 %. As the dark rates are higher during the day than at night, it is suspected that the setup is not fully light-tight even after coverage with blankets. The average dark rates for all channels were 519 ± 7 Hz during the day and 506 ± 6 Hz at night.

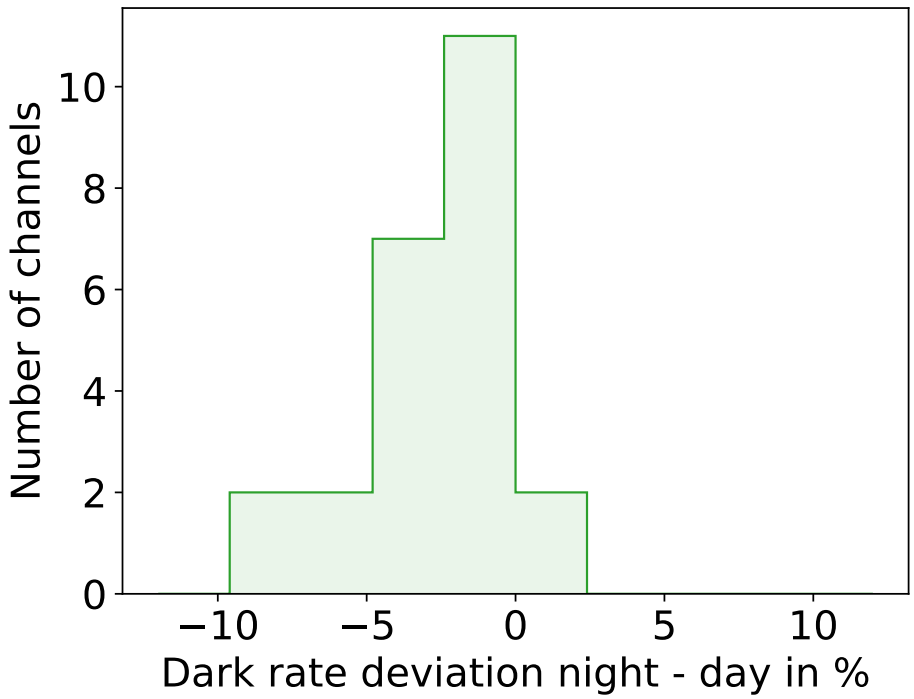

Figure 7.2: Deviations of dark rates collected during the day and at night. The night time measurement is used as reference.

To avoid corresponding systematic effects in the long-term monitoring analysis, the data obtained during the day are discarded. The corresponding measurements might have been affected by the light pollution within the setup.

In the future, the mDOM should be placed in an additional plastic bag as done for mDOM_D049_v1 (cf. Section 4.1). This is expected to increase the light-tightness of the setup.

7.3.2 Precision of the Initial Calibrations

The precision of the initial calibrations is evaluated for both the gain and the discriminator threshold. For this, the median observed gain and threshold values for all channels are calculated and compared to the corresponding target.

7.3.2.1 Gain

The results for the monitored gain values are shown in Figure 7.3. Both, the absolute values obtained in the channels and the relative deviations from the target gain of $5 \cdot 10^6$ are displayed. The corresponding mean, median and standard deviation for both distributions are provided in Table 7.1. Thus, the precision of the gain calibration using dark noise and the convolutional fit approach is comparable to the dark noise based calibration using the maximum likelihood fit described in Section 5.2.2.4. In total, 19 out of 24 channels are within the requirement for a sufficient calibration routine, i.e., these channels have a deviation of less than 5 % from the target gain (cf. Chapter 5). It is expected that the observed standard deviation of the observed gains is reduced when the calibration is performed without light pollution in the setup.

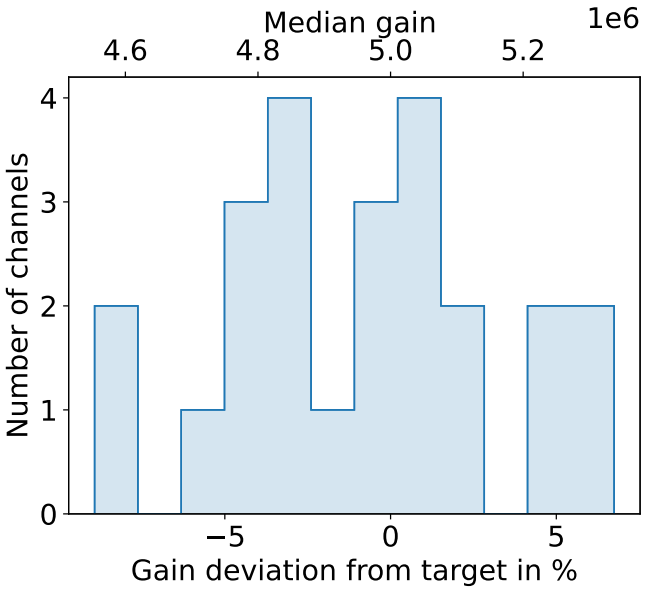

Figure 7.3: Precision of gain calibration in all investigated channels. The median of the obtained gain verification measurements is shown as well as the relative deviation from the target gain. A measurement time of 41 days is considered.

Table 7.1: Statistical measures for the precision of the gain calibration used for the long-term monitoring.

Type of distribution	Mean	Median	σ
Absolute values	$4.95 \cdot 10^6$	$4.95 \cdot 10^6$	$0.20 \cdot 10^6$
Relative deviation in %	-1.00	-1.00	4.04

7.3.2.2 Threshold

The results for the threshold calibration verification are shown in Figure 7.4. Both, absolute observed values and relative deviations from the target threshold are included. The corresponding statistical measures are displayed in Table 7.2 for the absolute values and their deviation from the target. The observed absolute standard deviation is smaller than the estimated resolution of the discriminator DAC of $0.01 \frac{\text{P.E.}}{\text{DAC}}$ in the charge region of interest (cf. Section 6.2.2). Thus, it is expected that this calibration can be considered sufficient. Nonetheless, the impact of the observed deviations from the target threshold must be investigated in more detail.

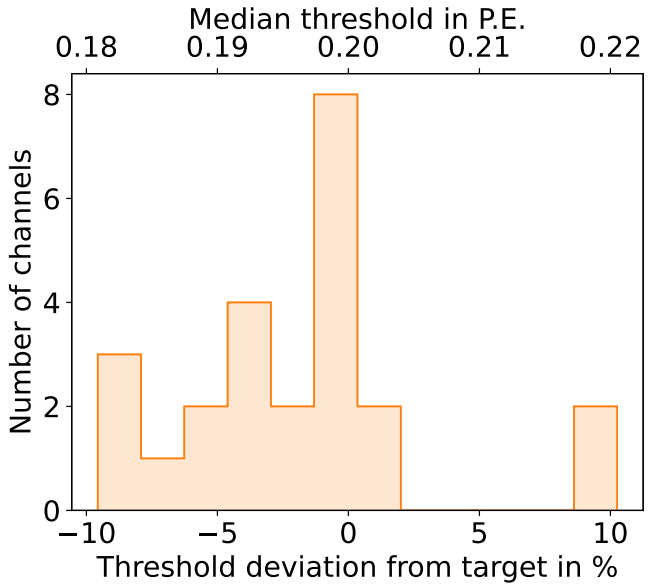

Figure 7.4: Precision of threshold calibration in all investigated channels. The median of the obtained threshold verification measurements is shown as well as the relative deviation from the target threshold. A measurement time of 41 days is considered.

Table 7.2: Statistical measures for the precision of the threshold calibration used for the long-term monitoring.

Type of distribution	Mean	Median	σ
Absolute values in P.E.	0.196	0.197	0.009
Relative deviation in %	-1.9	-1.3	4.7

7.3.3 Time-Series Overview

In Figure 7.5, an overview of all monitored quantities is shown for an example channel. Gain and threshold values extracted from fits with reduced χ^2 values below 0.01 or above 10 are highlighted using a deviating marker. This is the case for the monitored threshold value on the 22nd of September in this channel, accompanied by a large uncertainty.

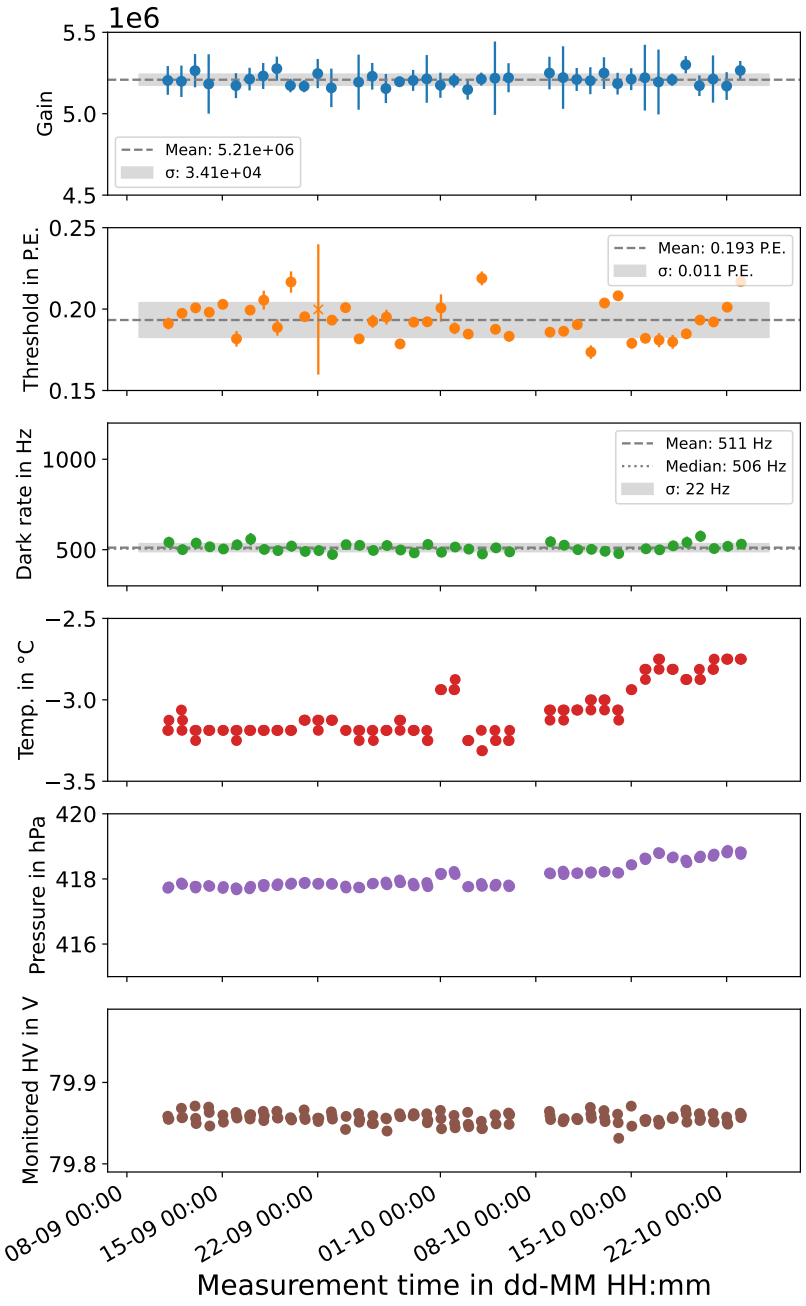

Figure 7.5: Overview of all quantities collected during long-term monitoring for an average channel (channel 10). The temperature is the mainboard temperature and therefore higher than the freezer temperature of -20°C.

Communication to the mDOM was lost for two days leading to missing data points for all properties during this time. In addition, no data files were produced for two other gain verification measurements. An unknown error has occurred during data acquisition, prohibiting the storage of the corresponding measurement files.

Over the course of the measurements, small changes below 1°C are observed in the mainboard temperature. The changes in temperature and pressure are correlated to each other as expected.

When more data is collected, the trends and changes should be investigated using a fit of the time-series of the individual quantities. In this thesis, the methods for this monitoring were developed and a test stand was set up in the laboratory. The setup will continue to operate, enabling the investigation of long-term effects over significantly longer measurement times in the future.

7.3.4 Stability Studies

In this section, the stability of the gain and the threshold is studied. The stability in terms of the drift is investigated. Following [32], the drift is defined as:

$$\text{drift} = \frac{\sum_{i=1}^{n} |\bar{p} - p_i|}{n\,\bar{p}}, \tag{7.1}$$

with the mean of the investigated property, $\bar{p}$, the values of the property in a single measurement, p_i, and the number of considered data points, n. Thus, this quantity corresponds to the mean absolute deviation normalized by the average of the investigated property [78].

In the future, the drift in dependence of the measurement time should be investigated. Longer-measurement are preferred for such an investigation.

7.3.4.1 Gain

The drift of the gain over the full measurement period was calculated for each channel individually. The result is shown in Figure 7.6. A mean gain drift of $(0.88 \pm 0.06)\,\%$ is obtained. This value is within one standard deviation from the overall observed gain deviation from the target gain (cf. Table 7.1). This mean drift in the channels is therefore negligible. However, longer measurement times are required to investigate longer-term variations of the gain.

The largest drift was observed in channel 17. The corresponding time-series of the gain and the monitoring values are shown in Figure 7.7. A temporarily increased gain is observed in a period of approximately 9 days in this channel. The mainboard temperature increases and decreases slightly within the corresponding time window. However, the temperature increases after the increase in gain and decreases before the gain returns to the initial values. Thus, it is unlikely that the change in gain is caused by the change in temperature. Furthermore, the monitored HV value is stable and does also not explain the observed change in gain. Therefore, the cause for the change in gain and threshold remains unclear.

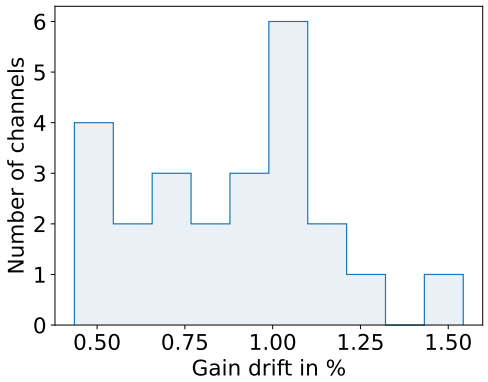

Figure 7.6: Distribution of the gain drift obtained in 24 investigated channels. A measurement period of 41 days is considered for each channel.

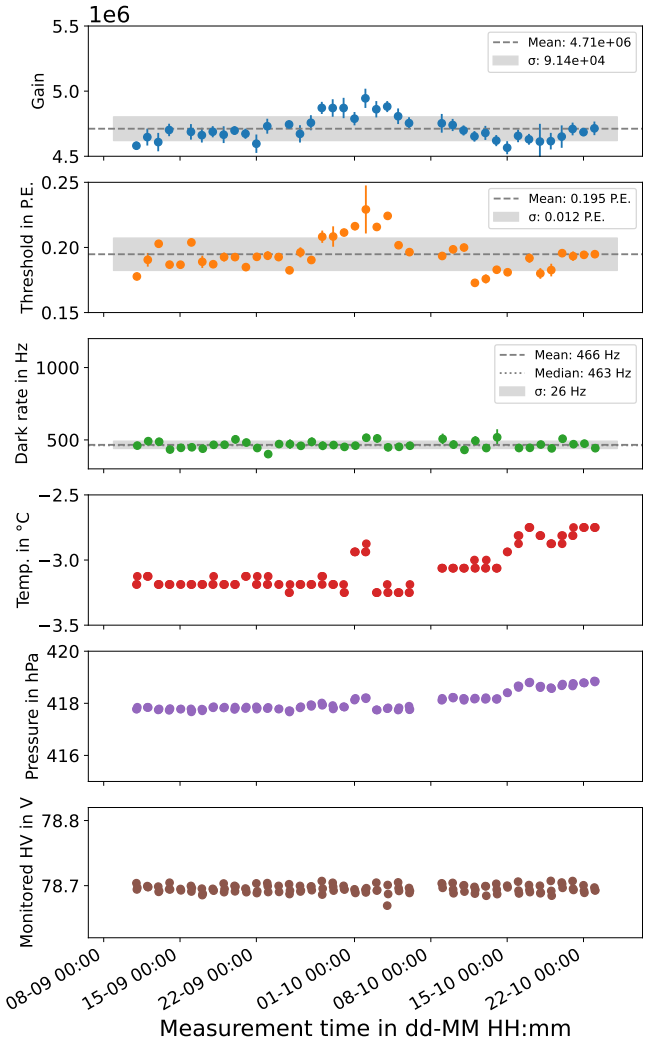

Figure 7.7: Overview of all quantities collected during long-term monitoring for channel 17 with the largest gain drift.

7.3.4.2 Threshold

The observed threshold drift for all channels is shown in Figure 7.8. The mean drift of the threshold is $(4.7 \pm 0.1)\,\%$ and is larger than the mean drift of the gain. As mentioned before, the impact of such a drift on the performance of the experiment must be investigated in more detail. However, it is expected that the influence is small as the absolute deviations from the target threshold shown in Figure 7.4 and Table 7.1 are small.

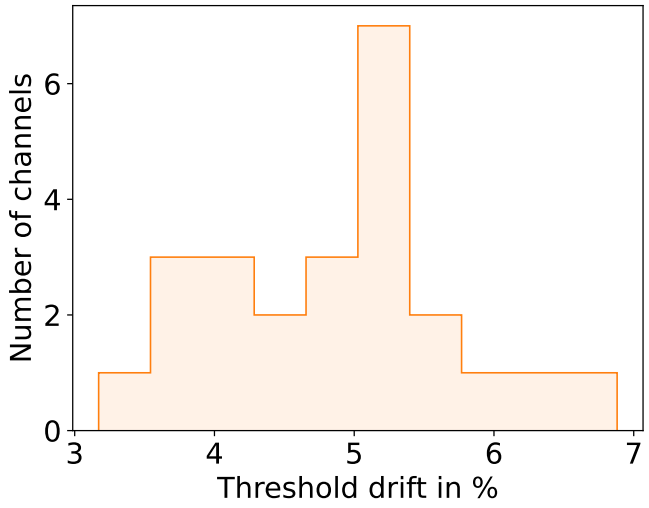

Figure 7.8: Distribution of the threshold drift obtained in 24 investigated channels. A measurement period of 41 days is considered for each channel.

In the channel with the largest drift, outliers with low statistics in the underlying SPE charge spectra were observed. It is expected that these outliers lead to the larger threshold drift in this particular channel. In the future, such spectra with low statistics should be avoided during data acquisition. A minimum required number of waveforms with charges close to the expected threshold during data acquisition should be specified. This means that the measurement in a particular channel is continued until the minimum number of waveforms is reached.

8 Summary and Conclusions

The goal of this thesis was to investigate if the calibration of an mDOM without artificial light is possible. Therefore, alternative calibration routines for the PMT gain and the discriminator threshold were developed and tested. In addition, a test stand for the long-term monitoring of the parameters using PMT dark noise was set up and operated.

For the development of a gain calibration routine, the performances of two different SPE fits were evaluated for the SPE spectra generated by dark noise. The fit models were adapted from the final acceptance testing (FAT) and the fit approach currently used in IceCube. Both models yielded an average deviation from the target gain of less than 5 % in the calibration routine. Therefore, both approaches are consistent with the engineering requirement of the IceCube Upgrade.

Systematic deviations of about 2.5 % were observed between the fit approaches. The deviation might be introduced by the differences in the fit function modeling the lower charge region of the SPE spectrum. In addition, minor inconsistencies were found in both fit functions and could contribute to the systematic deviation. The presence of systematic effects was confirmed by an LED based measurement. The observed deviation should be investigated in more detail in the future before the dark noise based calibration routine is used in-situ.

The threshold calibration results of the developed routine using dark noise were reproducible. The observed absolute deviations from the target gain of 0.2 P.E. were small. The impact of such deviations on the detector performance must be determined by simulations in the future. However, it is expected that the calibration is sufficient.

The dark noise based approach was found to be compatible with the calibration results using single flasher LEDs. In the LED measurements, a false trigger due to crosstalk between the calibration trigger and the discriminator was identified and filtered. Deviations between a single and a multi-LED approach were obtained in one channel. This should be investigated in more detail in the future, but it does not affect the dark noise based calibration. Following this analysis, the discriminator threshold calibration can be used in-situ.

Furthermore, a test stand for the dark noise based long-term monitoring of the calibrated values was set up and operated for several weeks to verify the stability of the calibrated values over longer time periods. Drifts in the gain of up to 1.5 % were observed, while the threshold showed drifts up to 6.9 %. In the future, time intervals will be considered in this analysis to investigate the time scales on which changes in gain and threshold are to be expected. The setup will continue to operate, enabling the investigation of long-term effects over significantly longer measurement times in the future. In addition, this monitoring can be used in-situ during normal detector operating conditions. This will furthermore allow to investigate deviations between the stable laboratory environment and the deployed modules in the ice.

In this thesis, a solid foundation for the mDOM calibration procedure based on dark noise has been laid. This dark noise approach ensures that reliable calibration remains possible even in the event of a flasher LED dysfunction. In addition, the dark noise based long-term monitoring routine can be applied during regular detector operations. Such continuous monitoring will contribute to an improved understanding of the IceCube Upgrade detector and thus the quality of the data it acquires. As of the submission of this thesis, the detector is nearing deployment and is expected to provide valuable insights into the field of neutrino physics.

Appendix

A Energy Threshold for Cherenkov Effect

In the scope of this thesis, for example potassium-40 decays inside of borosilicate glass are of interest. This type of glass of the manufacturer Vitrovex has a refractive index of approximately $n = 1.47$ [79]. Thus, for the Cherenkov effect to take place the emitted electrons need to overcome an energy threshold such that they move faster than the speed of light in the glass [25]. Therefore, the total energy that needs to be transferred to the electron in β decay such that Cherenkov radiation occurs can be calculated using the formula for the total relativistic energy of a moving particle:

$$E_{th}(v) = \frac{m_0 \cdot c^2}{\sqrt{1 - (\frac{v}{c})^2}} > \frac{m_0 \cdot c^2}{\sqrt{1 - (\frac{1}{n})^2}} \approx 697\,\text{keV} \tag{A.1}$$

Here, v is the velocity of the electron, m_0 is the rest mass of the electron being 511 keV and c is the speed of light in vacuum. It was used that $v > c_{glass} = \frac{c}{n_{glass}}$. Thus, Cherenkov radiation is to be expected from $^{40}\mathrm{K}$ decays in borosilicate glass as an energy transfer of 697 keV in the electronic system out of the total released energy of 1.311 MeV is possible. Such decays are a background source in optical neutrino detectors described below [40].

This formula can also be used to calculate the energy threshold for the Cherenkov effect in ice with a refractive index of approximately 1.3 [46]. This is therefore also relevant for the IceCube experiment.

B Laser Interlock System using Chatbots

Two chatbots were used to coordinate laser measurements for the LOMLogger development and light-sensitive calibration measurements with the mDOM. Both bots announced the start and the end of the respective measurements. An example conversation is show in Figure B.1. This chatbot interlock system was fully remotely accessible.

The real-life versions of the chatbots are shown in Figure B.2. Herbert, a key member of the Erlangen IceCube group, was responsible for the announcements of LOMLogger measurements and assists with outreach activities. Additionally, his tendency to appear in unexpected places made daily work in Erlangen much less predictable. Therefore, it was natural to give him the opportunity to express himself not only by his sheer existence but also in the form of text messages.

Papp-Martin (Cardboard-Martin) has a long tradition. He was created at the RWTH Aachen and found his way to ECAP via JGU Mainz. It was definitely (not) a coincidence that he followed his namesake Martin Rongen. Papp-Martin has now evolved and is able to send text messages, announcing the mDOM measurements.

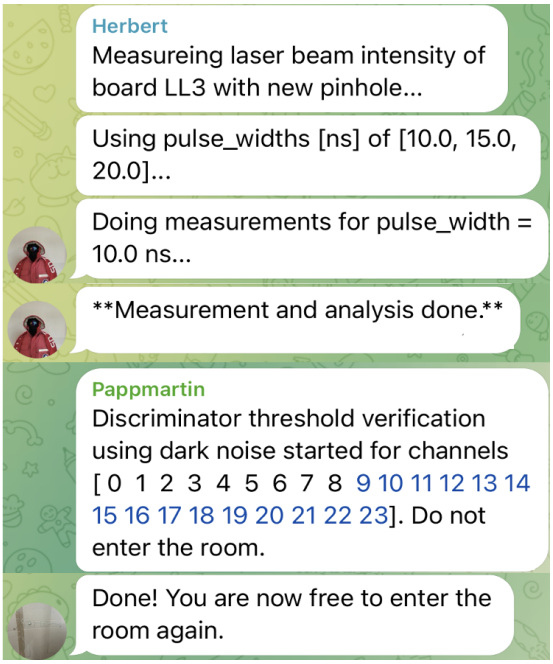

Figure B.1: Example for a typical chatbot conversation used as interlock system. Light-sensitive mDOM measurements and LOMLogger laser tests were coordinated.

Figure B.2: Real-life versions of chatbots. Left: Papp-Martin. Right: Herbert.

C Binning Study and Fit Stability for SPE Charge Spectra

In this section, the binning used for the different SPE spectra fits are motivated using measurement data of mDOM_D049_v1 at -30°C.

Maximum Likelihood Fit

For the maximum likelihood fit, different binnings were tested. This included binnings that used a fixed number of bins, either 30 or 40 bins distributed equally over the considered charge range. As described in Section 5.1.2.1, this charge range was defined in dependence on the set HV. This corresponds to bin widths of of 0.2 pC (HV below 83 V) or 0.33 pC (HV above 83 V) for 30 bins and 0.15 pC (HV below 83 V) or 0.25 pC (HV above 83 V) for 40 bins. Additionally, bin widths calculated using the Freedman-Diaconis rule were used (cf. Section 5.1.3).

The gain calibration analysis of the same charge data in one channel was performed 5 times for each binning. That means that for each of the repetitions, the SPE spectra were fitted using the Poisson likelihood fit approach. The target HV value was then extracted from a power law fit to the gain data in dependence of the set HV as described in Section 5.1.1 for each analysis run. Slight deviations in the target HV setting between the 5 repetitions were observed especially for the Freedman-Diaconis binning and the binning using a fixed amount of 30 bins. The mean values and the standard deviations of the calibration results are given in Table C.1. The values are compatible within the standard deviation. However, a binning with a fixed number of 40 bins is more stable than the other tested binnings and is therefore favored.

Table C.1: Mean and standard deviation of calibrated target HV values from 5 fit repetitions for different binnings.

Binning	Mean target HV	σ target HV
Freedman-Diaconis	81.80	0.07
Fixed 30 bins	81.78	0.08
Fixed 40 bins	81.74	0.000003

An example SPE spectrum with the corresponding maximum likelihood fit with a fixed number of 40 bins is shown in Figure 5.4 the corresponding likelihood profile is shown in Figure 5.6. In this fit, the higher PE contribution is described by the exponential function that models the poorly amplified electrons on the left hand side of the spectrum. From a physical point of view, this is not intended. Thus, the fit would profit from including further nPE contributions and an additional penalty term constraining the slope of the exponential function.

Convolutional Fit

The fit stability for the convolutional fit was tested similarly to the stability of the maximum likelihood approach. Thus, the same data with different binnings was fitted 5 times each using the convolutional fit. For this approach, 6 different numbers of fixed bins were tested between 150 and 650 bins. Here, the number of bins is distributed evenly between 0 and 50 pC. Thus, bin widths between approximately 0.08 pC and 0.3 pC were tested. The tested bin widths therefore overlap between the fit procedures. Unlike the results from the maximum likelihood fit, the calibration results for each binning were consistent and no deviations were observed. Thus, the convolutional fit is considered to be stable independent of the binning.

As the binning does not influence the fit stability, the goodness of fit was determined for the convolutional fit. Thus, one full data set consisting of 5 SPE spectra at different HV settings was considered for two channels. The fit was performed for each spectrum using the binnings described above and the corresponding reduced χ^2 value was determined. The results for this metric for the goodness of fit in dependence of the high voltage setting is shown in Figure C.1 for channels 0 and 9 which is an arbitrary choice.

For channel 0, a binning with a number of 250 bins leads to the best reduced χ^2 values, closest to an ideal fit for all HV values above 80 V. However, for 78 V 250 bins perform worst. For channel 9, the binning of 350 bins performs best for all HV values, even though the reduced χ^2 value is quite large at 78 V. Thus, there is not one binning that accommodates ideally for all channels and HV values. In this thesis, binnings of 250 and 350 bins are chosen as a compromise.

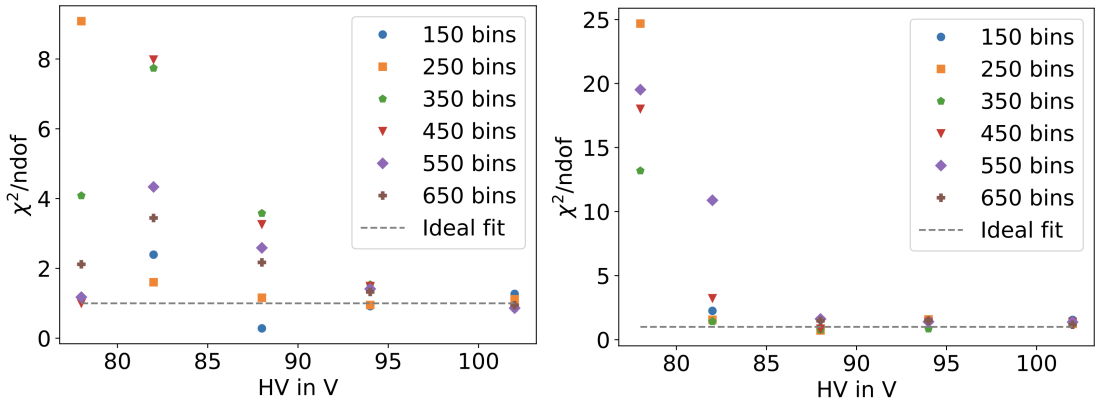

(a) Channel 0 (b) Channel 9

Figure C.1: Reduced χ^2 values at different HV settings of convolutional fit for different bin numbers in two different channels.

In Figure 5.7, an example SPE spectrum with a bin width of 0.2 pC, i.e. 250 bins up to 50 pC, and the fit result of the convolutional fit is shown. In addition to the overall fit result, the individual components of the fit are displayed. The residuals in the lower part are given by the absolute distance between the data points and the fit. The feature in the residuals where the data points deviate from the fit in the lower charge region is observed in almost

all fits independent of the channel and the high voltage settings. This might be a result of the mathematical uncertainties of the SPE model at low charges. Thus, the fit would profit from an improved description of the low charge region, i.e. the contribution of the under-amplified electrons.

D Jeffreys Interval

There are several approaches to describe the uncertainties of a binomial distribution. In [80], it is suggested to use Jeffreys intervals, especially for smaller sample sizes due to its good coverage properties. The advantage of this credible interval is that it is derived from Bayesian theory but can also be justified from a frequentist's point of view [80]. Furthermore, the resulting interval is equal-tailed, reducing systematic bias.

Jeffreys interval is based on the Jeffreys prior [81]. This prior is closely connected to the Fisher information. Calculating the Fisher information for a binomial distribution leads to the functional form of a Beta distribution with parameters 1/2, 1/2, i.e., Beta$(1/2, 1/2)$. This distribution can then be interpreted as the noninformative Jeffreys prior. Additionally, this prior is a conjugate prior for the binomial distribution, meaning that the posterior, i.e., the product of the binomial distribution and the prior is again a Beta distribution. The resulting posterior has the form of Beta$(X + 1/2, n - X + 1/2)$ [80]. Here, X is the number of successes and n is the sample size, i.e. the number of trials.

The limits of Jeffreys interval are then calculated based on this distribution and it's respective $\alpha/2$ and $1 - \alpha/2$ quantiles [80]. These quantiles p of the Beta distribution with parameters a and b will be denoted with $\mathrm{B}(p; a, b)$. Thus, the lower limit L of the Jeffreys interval is given by:

$$L(X) = \mathrm{B}(\alpha/2; X + 1/2, n - X + 1/2) \tag{D.1}$$

Whereas the upper limit U is calculated as:

$$U(X) = \mathrm{B}(1 - \alpha/2; X + 1/2, n - X + 1/2) \tag{D.2}$$

In edge cases like $X = 0$ or $X = n$, the limits are adjusted to be $L(0) = 0$, respectively $U(n) = 1$. Otherwise, the coverage probability would go to zero.

From a frequentist's point of view, the Jeffreys interval can be interpreted as modification of the Clopper-Pearson interval that can directly be derived from the binomial distribution [80]. The Clopper-Pearson interval is known for its tendency to overestimate uncertainties. The Jeffreys interval corrects for this while maintaining sufficient coverage probability important for the usage in a frequentist's framework.

E Front-end Pulser Based Threshold Calibration

A further alternative for the discriminator threshold calibration relying on the flasher LEDs is investigated in this chapter. Instead of PMT signals, the front-end test pulser described

in Section 3.3.2 is used.

E.1 Methods and Procedure

This section provides an overview of the threshold calibration approach using the front-end test pulser. This includes the descriptions of the individual steps used for this method. The general idea for this calibration routine was developed during the "DESY Summer School 2024" [74] and was refined and investigated in more detail in the scope of this thesis.

E.1.1 General Calibration Approach

The goal for the calibration is to find the discriminator threshold at which the trigger efficiency is 50 % for PMT pulses with a charge of 0.2 P.E. In this approach, the front-end test pulser is used to model such PMT pulses. The width of the test pulses is fixed due to the constant capacity of the underlying capacitor. The pulse height can be adjusted using the test pulser DAC. Instead of calibrating the threshold to a certain pulse charge, the threshold calibration is based on the observed pulse height of an average 0.2 P.E. pulse described in Section E.1.2. The following routine is performed in each channel:

1. Find the test pulser DAC setting to generate pulses with the target ADC pulse height. This target corresponds to the pulse height obtained for an average 0.2 P.E. PMT pulse.
2. Use the obtained target to adjust the pulser DAC settings and generate pulses of fixed height. Then, sweep the discriminator threshold through several discriminator DAC settings to obtain a trigger efficiency curve.
3. Fit the curve with an error function and extract the discriminator DAC value at 50 % efficiency level.
4. Verify the calibration setting by measuring the trigger efficiency at the target threshold in DAC.

The details of the individual steps are explained in the following.

E.1.2 Modeling PMT Pulses using the Front-end Test Pulser

As described above, the threshold calibration routine using the test pulser is based on a target pulse height instead of a target charge. This relies on the linear relation between the PMT pulse height observed in the ADC and the corresponding charge shown in Figure E.1. The individual data points are obtained by extracting both the pulse height and the corresponding charges of recorded PMT waveforms. Following the linear fit, a pulse with a charge of 0.2 P.E. has a pulse height of (8.26 ± 0.02) ADC counts. This should therefore be the target pulse height. Due to an issue with the initial charge conversion, the target pulse height used in this thesis is 10 ADC counts, corresponding to a target charge of approximately 0.24 P.E.

An example for pulses generated by the test pulser and the PMT are shown in Figure E.2. The charge contained in each pulse is approximately 0.24 P.E.

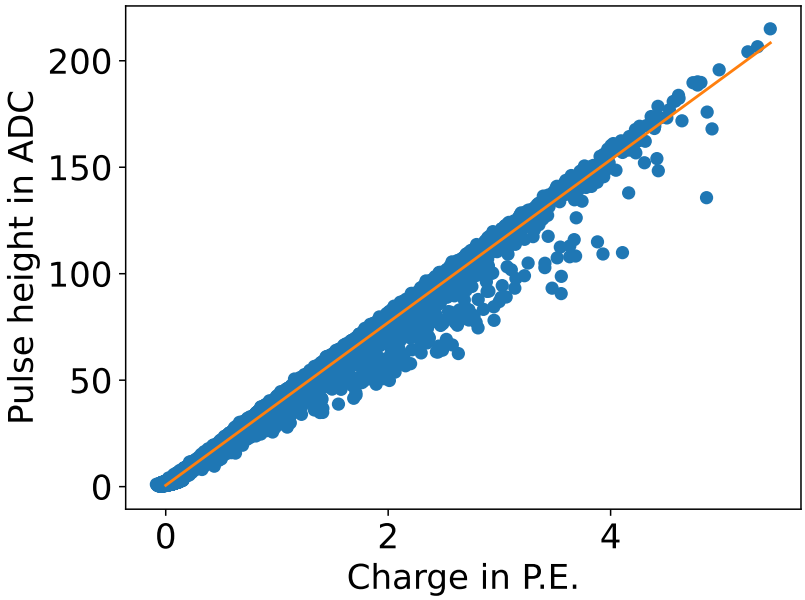

Figure E.1: Dependence of pulse charge on the ADC pulse height for flasher pulses with linear fit.

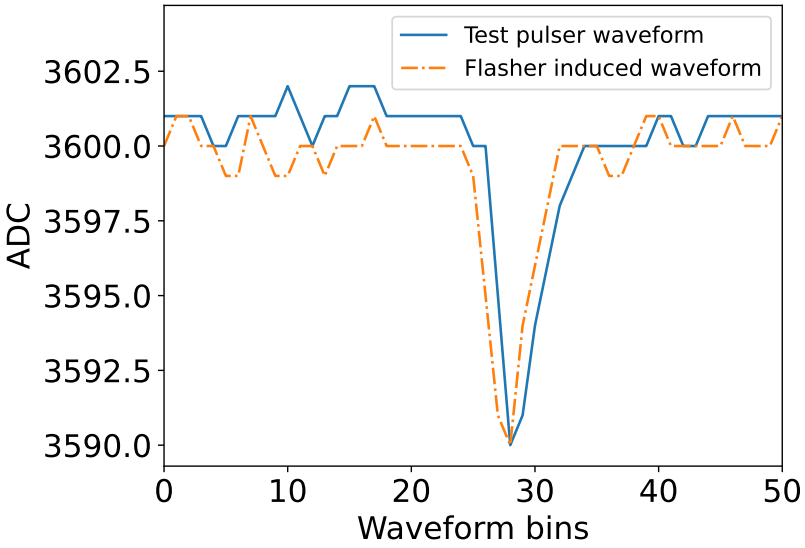

Figure E.2: Examples for test pulser and PMT generated pulses with a charge of approximately 0.25 P.E.

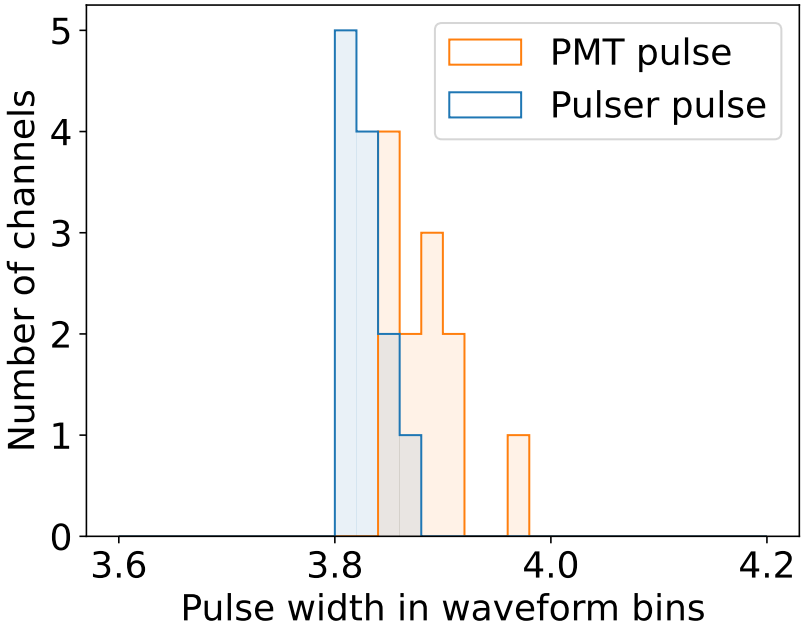

Figure E.3: Pulse width comparison of PMT and test pulser pulses.

The widths of the PMT and test pulser pulses are investigated in more detail as described in Section 4.2.3. The pulses were fitted using a Gaussian function and the FWHM was calculated using Equation 4.4. The average pulse widths for 12 investigated channels are shown in Figure E.3. The mean pulse width of the test pulser pulses is (3.88 ± 0.04) waveform bins and (3.83 ± 0.02) waveform bins. The widths are compatible within the corresponding standard deviations. However, to avoid a bias in the charge integration, the thresholds are only investigated in terms of the ADC pulse height in the following.

E.1.3 ADC Pulse Height to Test Pulser DAC Conversion

Before the discriminator threshold can be calibrated, the pulser DAC setting corresponding to the target pulse height in ADC must be determined. This is done by sweeping through 10 different test pulser DAC settings between 700 and 5200 DAC. At each DAC setting, a fixed number of test pulser pulses is recorded. The mean observed pulse height is calculated as described in Section 4.2.3. The target DAC is obtained from a linear fit to the pulse height values in dependence of the corresponding pulser DAC. A corresponding example is shown in Figure E.4.

E.1.3.1 Threshold Scan

Test pulses with the target pulse height are generated and a trigger efficiency curve of the discriminator is recorded. This means that the discriminator threshold is swept through an interval of 120 DACs around the expected target threshold. For each threshold DAC, the trigger efficiency is determined by the number of observed threshold crossings and generated test pulser pulses. This procedure is repeated five times per channel and error functions are fitted to the curves. An example for such trigger efficiency curves with corresponding fits is

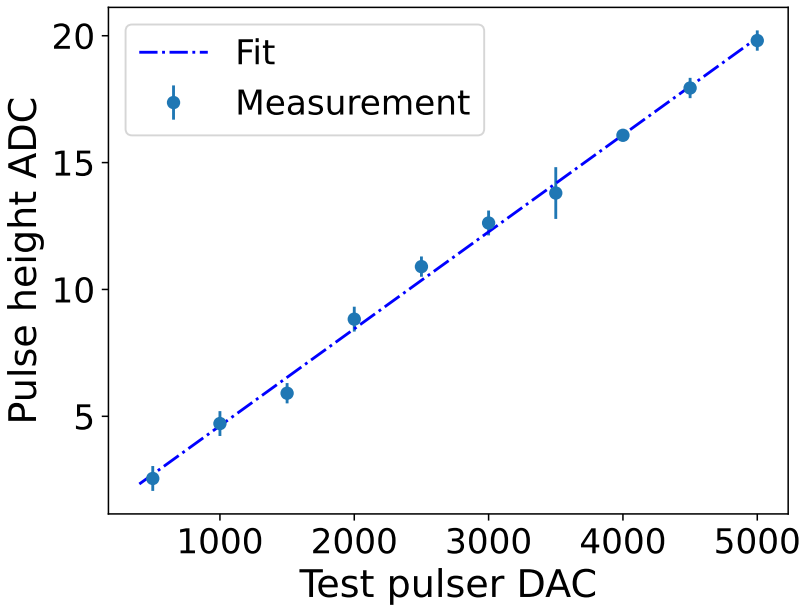

Figure E.4: Example data set with linear fit used for the conversion of target ADC pulse height to test pulser DAC value.

shown in Figure E.5. The threshold at the 50 % trigger efficiency level is extracted from each fit and the mean value is used as calibrated threshold in DAC.

E.1.3.2 Calibration Verification Procedure

As described for the gain calibration and the threshold calibration using dark noise, the calibration must also be verified before it is used in-situ.

In the case of the discriminator threshold calibration using the test pulser, a pulse height spectrum is recorded at the target threshold. Test pulser generated pulses with different pulse heights are collected together with the information if the discriminator was triggered or not. Similar to the verification using dark noise, two spectra are created (cf. Figure E.6 (left)). One spectrum contains all recorded pulse heights and the other one only contains pulse heights that were triggered by the discriminator. A trigger efficiency curve is obtained by the ratio of these spectra (cf. Figure E.6 (right)). The uncertainties are described by Jeffrey's intervals as explained in Section 6.1.4. The threshold in ADC pulse height is obtained from an error function fit.

E.2 Analysis and Results

In this section, the results of the test pulser based threshold calibration are presented. The precision of the calibration is obtained. In addition, the calibration results are verified both using the test pulser and the flasher LEDs.

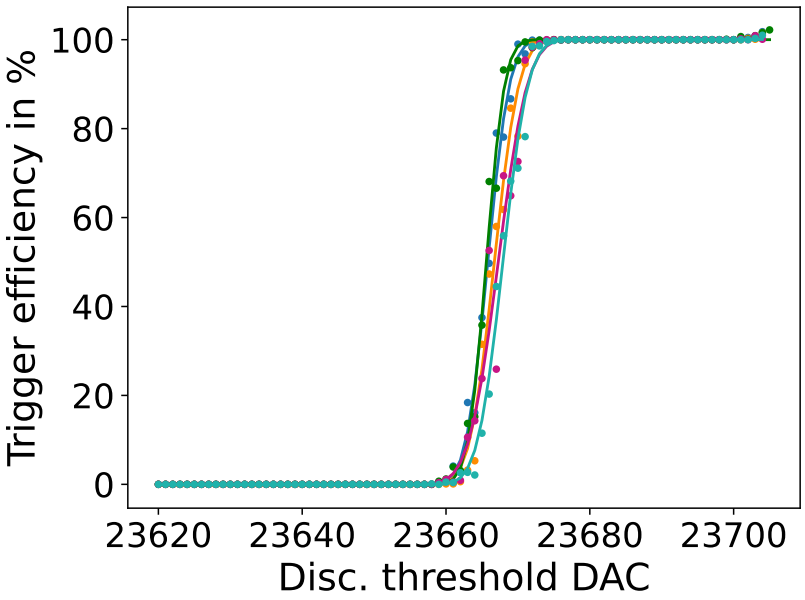

Figure E.5: Threshold scan used for test pulser based calibration. The test pulser is set to a fixed pulse height and the scan is repeated five times. Error functions are fitted to the data sets.

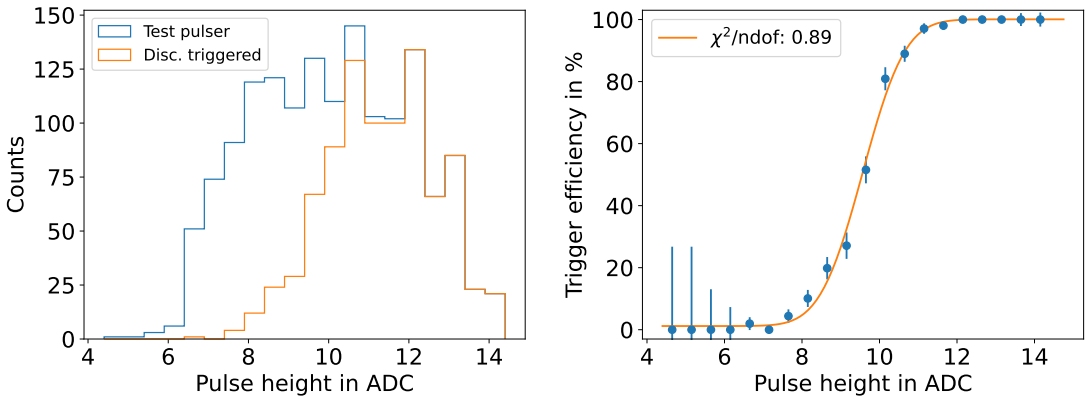

Figure E.6: Verification procedure. Left: Histograms of recorded pulses and discriminator triggered pulses. Right: Trigger efficiency curve obtained from the ratio of the histograms. An error function fit is included.

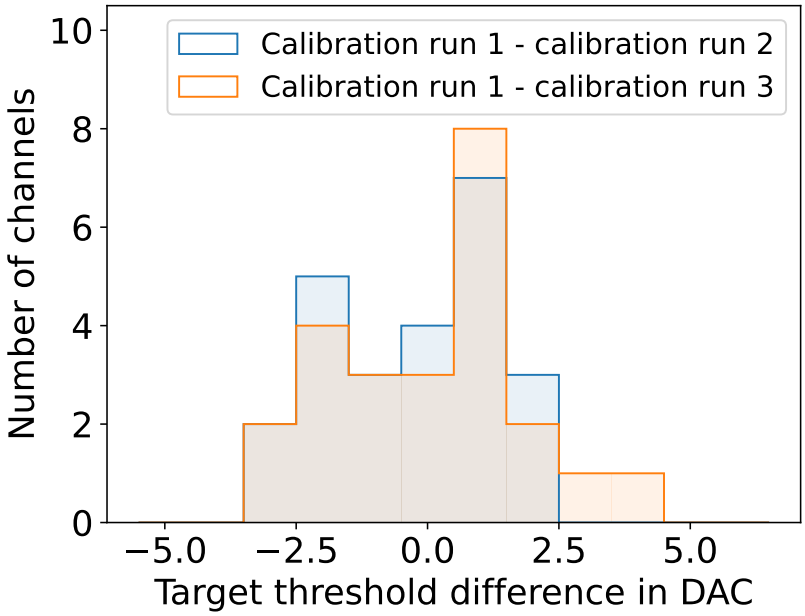

Figure E.7: Difference of target thresholds in DAC between 3 calibration runs

E.2.1 Test Pulser Calibration Results

The test pulser calibration was repeated three times for mDOM_D115_v1 at room temperature to investigate the reproducibility of the calibration result. The individual repetitions will be referred to as calibration run 1, 2 and 3. The obtained thresholds in DAC counts for the repetitions are shown in Figure E.7 in reference to run 1. The mean difference between the results from run 1 and 2 is (-0.25 ± 0.32) DAC counts. For run 1 and 3, the mean difference is (0.08 ± 0.37) DAC counts. The calibrations can therefore be interpreted as consistent and reproducible.

E.2.2 Test Pulser Verification Results

The obtained thresholds from all three calibration runs are verified once using the approach explained in Section E.1.3.2. The results are shown in Figure E.8. Both, absolute values and relative deviations from the target are included. The means, standard deviations and medians of all distributions are provided in Table E.1. On average, the obtained thresholds are compatible with the target. However, larger deviations between the pulse heights in the channels are observed.

The verification failed for one channel in all measurements. This means that the 50 % trigger efficiency was not reached in the trigger efficiency curve of this channel. The corresponding data point is therefore missing in the histograms. The verification of run 1 failed in an additional channel. Furthermore, this channel lead to the outlier observed in verification run 3 with a deviation of more than 75 % from the target threshold. No irregularities were observed in the calibration of these channels using a fixed pulse height. In addition, the channels were well-behaved in the dark noise based threshold calibration and verification described in Section 6.2.3. Therefore, it is unlikely that the discriminator is causing the

Table E.1: Statistical measures for the verification of three threshold calibration runs using the front-end test pulser.

Calibration run	Type of distribution	Mean	Median	σ
1	Absolute values in ADC	9.9	9.8	0.6
1	Relative deviation in %	-0.8	-2.0	5.6
2	Absolute values in ADC	9.6	9.6	0.6
2	Relative deviation in %	-4.3	-3.9	5.6
3	Absolute values in ADC	9.5	9.6	1.9
3	Relative deviation in %	-4.9	-3.8	18.9

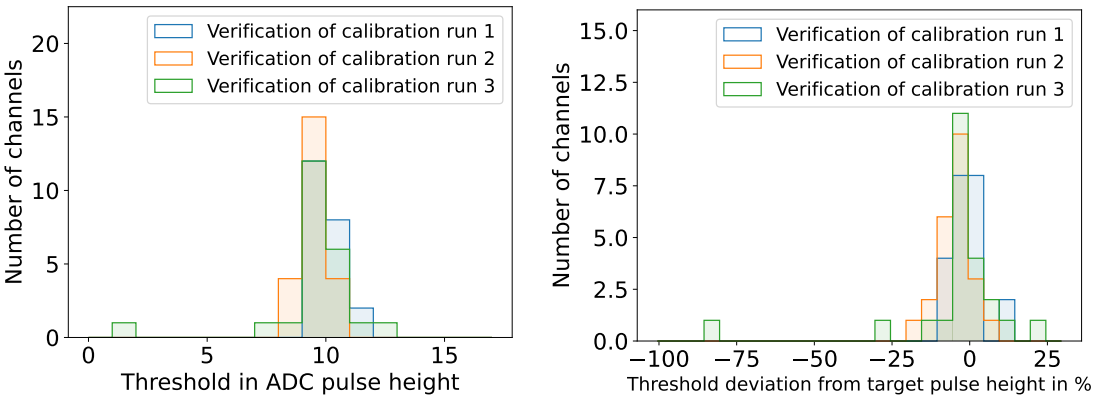

Figure E.8: Verification for the discriminator threshold values obtained in three different calibration runs using the test pulser. Left: Absolute values of the verification in terms of pulse height. Right: Relative deviations from the target pulse height. The measurements were conducted at room temperature.

issues observed in the particular channels. Instead, it is expected that this is an artifact of the raw test pulser signals.

The discriminator triggers on the raw pulser generated signal, while only a smoothed pulse is observed in the ADC readout (cf. Section 3.3.2). Thus, it is possible that the pulse shaping chain introduces a discrepancy between the height of the pulse picked up by the discriminator and the signal height obtained in the ADC readout. In the outlier channels, the raw pulse might contain a contribution that causes the discriminator to detect a signal with nearly the same rising edge regardless of the pulser DAC setting. This additional contribution might then be smoothed out completely before the signal is recorded in the ADC. Thus, pulses with low apparent heights in the ADC will still be defined as triggered by the discriminator. This leads to the trigger efficiency not reaching 50 %. Since the mDOM used in these measurements is fully integrated, it was not possible to access the raw pulser generated signals directly. Therefore, this hypothesis could not be confirmed using the mDOM. An alternative is to investigate raw pulser pulses using an mDOM mainboard. However, this was not done within this thesis.

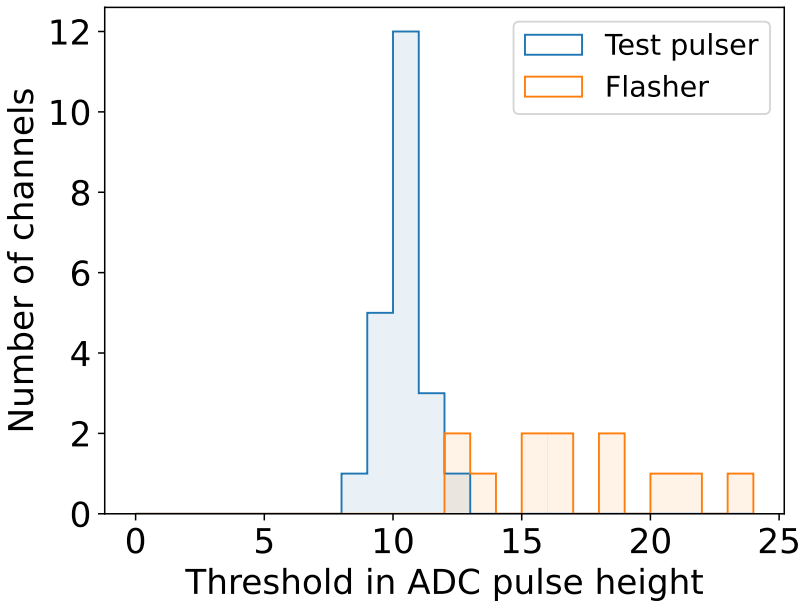

Figure E.9: Verification comparison of test pulser and flasher measurements at the same threshold DAC settings.

E.2.3 Test Pulser - LED Threshold Comparison

The compatibility of the test pulser and flasher based methods is investigated. For this, the target threshold DAC obtained in the pulser based calibration is selected. Then, the threshold is measured using the flasher LEDs. The discriminator trigger response is filtered to avoid excess false triggers described in Section 6.2.4. The results for the test pulser and the LED measurements are shown in Figure E.9. All 24 channels are considered for the test pulser measurement. The flasher measurement was only performed in the bottom hemisphere of the mDOM due to a broken flasher chain in the upper hemisphere. Therefore, only 12 channels are included for the flasher based verification.

The observed mean threshold for the test pulser measurement is (10.4 ± 0.1) ADC counts. The flasher based measurement yields a mean threshold of (17.0 ± 1.0) ADC. These thresholds are therefore not compatible with each other.

In the mDOM, the PMT is DC-coupled while the test pulser is AC-coupled [52], [82]. This may lead to a baseline deviation between the PMT and the test pulser. Such a deviation might introduce the observed discrepancy in the thresholds for the test pulser and the PMT at the same discriminator setting. To investigate this, the noise level of the pulser and the PMT is obtained using the `Iceboot` function `mDOMSetDiscriminatorThresholds()` and Equation 6.1. The results are shown in Figure E.10. The mean baseline difference is (1.0 ± 2.0) DAC for all investigated channels. This deviation is comparable to the deviations observed between the different calibration runs using the test pulser. Thus, this baseline deviation might contribute to the discrepancy between the verification methods but is not sufficient to fully explain the differences.

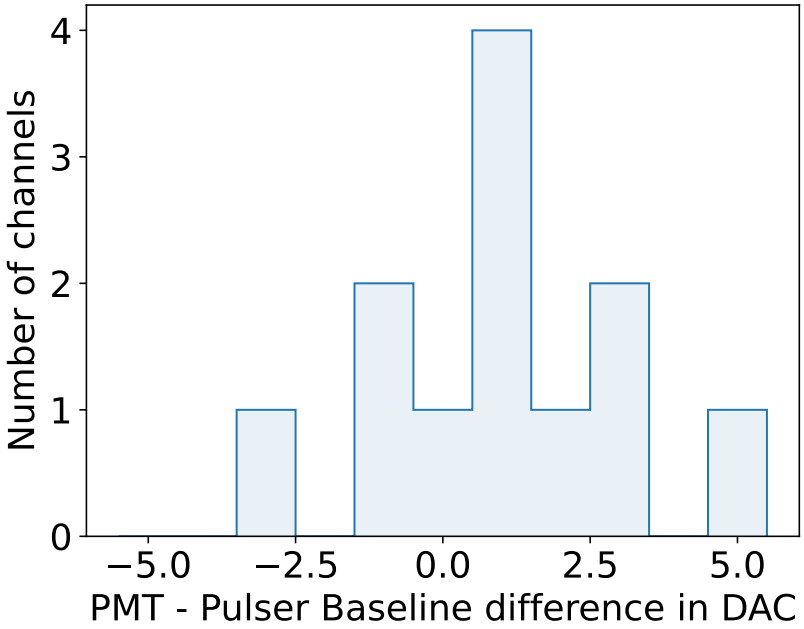

Figure E.10: Comparison of baseline values of PMT and test pulser.

It is likely that the deviation in the observed thresholds is again due to the pulse shaping chain before the ADC readout. Some contributions of the raw pulser signal picked up by the discriminator might be smoothed out during pulse shaping. Thus, the signal in the ADC appears to be smaller than the pulse that is fed into the discriminator. In this case, the ADC-DAC conversion described in Section E.1.3 would not be suitable to select the target test pulser DAC setting. For this conversion, only ADC signals are considered, neglecting effects introduced by the pulse shaping.

Thus, in case that the test pulser should be used for the discriminator threshold calibration, the approach to select a suitable pulser DAC value must be adjusted. The impact of the pulse shaping chain on the pulser signal must be included. This was not done within this thesis as the calibration approach using dark noise presented in Chapter 6 showed promising results.

Bibliography

[1] S. F. Mason, K. M. Meyer-Abich, and B. Sticker. *Geschichte der Naturwissenschaft in der Entwicklung ihrer Denkweisen*. de. Diepholz, Germany: GNT-Verlag, 1997.

[2] M. Ahlers, K. Helbing, and C. Pérez de los Heros. "Probing particle physics with IceCube". In: *The European Physical Journal C* 78.11 (Nov. 2018). ISSN: 1434-6052. DOI: 10.1140/epjc/s10052-018-6369-9. URL: http://dx.doi.org/10.1140/epjc/s10052-018-6369-9.

[3] A. Ishihara. *The IceCube Upgrade – Design and Science Goals*. 2019. arXiv: 1908.09441 [astro-ph.HE]. URL: https://arxiv.org/abs/1908.09441.

[4] S. Mechbal and N. Feigl. "Characterization and testing of the IceCube Upgrade mDOM". In: *PoS* ICRC2023 (2023), p. 1183. DOI: 10.22323/1.444.1183.

[5] S. Fukami. *Status and performance of mass-produced IceCube Upgrade mDOMs*. 2025. arXiv: 2507.07273 [astro-ph.HE]. URL: https://arxiv.org/abs/2507.07273.

[6] N. Schmitz. *Neutrinophysik*. Vieweg+Teubner Verlag, 1997. ISBN: 9783322801142. DOI: 10.1007/978-3-322-80114-2. URL: http://dx.doi.org/10.1007/978-3-322-80114-2.

[7] U.F. Katz and Ch. Spiering. "High-energy neutrino astrophysics: Status and perspectives". In: *Progress in Particle and Nuclear Physics* 67.3 (July 2012), 651–704. ISSN: 0146-6410. DOI: 10.1016/j.ppnp.2011.12.001. URL: http://dx.doi.org/10.1016/j.ppnp.2011.12.001.

[8] C. Grupen. *Einstieg in die Astroteilchenphysik: Grundlagen, Messungen und Ergebnisse aktueller Forschung*. Springer Berlin Heidelberg, 2018. ISBN: 9783662552711. DOI: 10.1007/978-3-662-55271-1. URL: http://dx.doi.org/10.1007/978-3-662-55271-1.

[9] C. Patrignani et al. "Review of Particle Physics". In: *Chinese Physics C* 40.10 (2016). (Particle Data Group), p. 100001. DOI: 10.1088/1674-1137/40/10/100001.

[10] C. Giunti and C. W. Kim. *Fundamentals of Neutrino Physics and Astrophysics*. 2007. ISBN: 978-0-19-850871-7. DOI: 10.1093/acprof:oso/9780198508717.001.0001.

[11] A. Bulmahn and M. H. Reno. "Secondary atmospheric tau neutrino production". In: *Physical Review D* 82.5 (Sept. 2010). ISSN: 1550-2368. DOI: 10.1103/physrevd.82.057302. URL: http://dx.doi.org/10.1103/PhysRevD.82.057302.

[12] M. Ahlers and F. Halzen. "IceCube: Neutrinos and multimessenger astronomy". In: *Progress of Theoretical and Experimental Physics* 2017.12 (Nov. 2017). ISSN: 2050-3911. DOI: 10.1093/ptep/ptx021. URL: http://dx.doi.org/10.1093/ptep/ptx021.

[13] L. Pyras. "Cosmic Rays and the Radio Neutrino Observatory Greenland (RNO-G)". en. In: (2024). DOI: 10.25593/OPEN-FAU-957. URL: https://open.fau.de/handle/openfau/31649.

[14] S. Biagi. "Results of the first detection units of KM3NeT". In: *Nuclear Instruments and Methods in Physics Research Section A: Accelerators, Spectrometers, Detectors and Associated Equipment* 876 (2017). The 9th international workshop on Ring Imaging Cherenkov Detectors (RICH2016), pp. 181–184. ISSN: 0168-9002. DOI: https://doi.org/10.1016/j.nima.2017.02.073. URL: https://www.sciencedirect.com/science/article/pii/S0168900217302735.

[15] IceCube Collaboration. "Observation of High-Energy Astrophysical Neutrinos in Three Years of IceCube Data". In: *Physical Review Letters* 113.10 (Sept. 2014). ISSN: 1079-7114. DOI: 10.1103/physrevlett.113.101101. URL: http://dx.doi.org/10.1103/PhysRevLett.113.101101.

[16] IceCube Collaboration. "Observation of high-energy neutrinos from the Galactic plane". In: *Science* 380.6652 (June 2023), 1338–1343. ISSN: 1095-9203. DOI: 10.1126/science.adc9818. URL: http://dx.doi.org/10.1126/science.adc9818.

[17] M. Nakahata. *History of Solar Neutrino Observations*. 2022. arXiv: 2202.12421 [hep-ex]. URL: https://arxiv.org/abs/2202.12421.

[18] A. Bellerive et al. "The Sudbury Neutrino Observatory". In: *Nuclear Physics B* 908 (July 2016), 30–51. ISSN: 0550-3213. DOI: 10.1016/j.nuclphysb.2016.04.035. URL: http://dx.doi.org/10.1016/j.nuclphysb.2016.04.035.

[19] Y. Oyama. "Toward the confirmation of atmospheric neutrino oscillations". In: *Progress of Theoretical and Experimental Physics* 2024.5 (July 2023). ISSN: 2050-3911. DOI: 10.1093/ptep/ptad097. URL: http://dx.doi.org/10.1093/ptep/ptad097.

[20] C. Giganti, S. Lavignac, and M. Zito. "Neutrino oscillations: The rise of the PMNS paradigm". In: *Progress in Particle and Nuclear Physics* 98 (Jan. 2018), 1–54. ISSN: 0146-6410. DOI: 10.1016/j.ppnp.2017.10.001. URL: http://dx.doi.org/10.1016/j.ppnp.2017.10.001.

[21] C. R. Das et al. "Determination of the octant in long baseline neutrino experiments within and beyond the standard model". In: *Physical Review D* 97.3 (Feb. 2018). ISSN: 2470-0029. DOI: 10.1103/physrevd.97.035023. URL: http://dx.doi.org/10.1103/PhysRevD.97.035023.

[22] KATRIN Collaboration. "Direct neutrino-mass measurement based on 259 days of KATRIN data". In: *Science* 388.6743 (Apr. 2025), 180–185. ISSN: 1095-9203. DOI: 10.1126/science.adq9592. URL: http://dx.doi.org/10.1126/science.adq9592.

[23] IceCube Collaboration. "Development of an analysis to probe the neutrino mass ordering with atmospheric neutrinos using three years of IceCube DeepCore data: IceCube Collaboration". In: *The European Physical Journal C* 80.1 (Jan. 2020). ISSN: 1434-6052. DOI: 10.1140/epjc/s10052-019-7555-0. URL: http://dx.doi.org/10.1140/epjc/s10052-019-7555-0.

[24] KM3NeT Collaboration. "Letter of intent for KM3NeT 2.0". In: *Journal of Physics G: Nuclear and Particle Physics* 43.8 (June 2016), p. 084001. ISSN: 1361-6471. DOI: 10.1088/0954-3899/43/8/084001. URL: http://dx.doi.org/10.1088/0954-3899/43/8/084001.

[25] H. Kolanoski and N. Wermes. *Teilchendetektoren*. de. 1st ed. Berlin, Germany: Springer, Mar. 2016.

[26] M. F. L'Annunziata. "Chapter 16 - Cherenkov Radiation". In: *Radioactivity (Second Edition)*. Ed. by M. F. L'Annunziata. Second Edition. Boston: Elsevier, 2016, pp. 547–581. ISBN: 978-0-444-63489-4. DOI: https://doi.org/10.1016/B978-0-444-63489-4.00016-2. URL: https://www.sciencedirect.com/science/article/pii/B9780444634894000162.

[27] L. Rädel and C. Wiebusch. "Calculation of the Cherenkov light yield from low energetic secondary particles accompanying high-energy muons in ice and water with Geant4 simulations". In: *Astroparticle Physics* 38 (Oct. 2012), 53–67. ISSN: 0927-6505. DOI: 10.1016/j.astropartphys.2012.09.008. URL: http://dx.doi.org/10.1016/j.astropartphys.2012.09.008.

[28] Hamamatsu Photonics K.K. *Photomultiplier Tubes: Basics and Applications*. Technical handbook, Hamamatsu Photonics. Accessed: 05.10.2025. 2017. URL: https://www.hamamatsu.com/content/dam/hamamatsu-photonics/sites/documents/99_SALES_LIBRARY/etd/PMT_handbook_v4E.pdf.

[29] Jkrieger and Dietzel65. *Scheme of a Photomultiplier Tube (PMT)*. Wikimedia Commons. Accessed: 05.10.2025. 2007. URL: https://en.wikipedia.org/wiki/File:Photomultiplier_schema_en.png..

[30] S.-O. Flyckt and C. Marmonier. *Photomultiplier Tubes: Principles and Applications*. Accessed: 05.10.2025. Photonis, 2002. URL: https://lmu.web.psi.ch/docu/manuals/bulk_manuals/PMTs/Photonis_PM-Handbook.pdf.

[31] L. Classen. "The mDOM – a multi-PMT digital optical module for the IceCube-Gen2 neutrino telescope". Accessed: 05.10.2025. PhD thesis. Friedrich-Alexander-Universität Erlangen-Nürnberg (FAU), 2017. URL: https://nbn-resolving.org/urn:nbn:de:bvb:29-opus4-86782.

[32] W. R. Leo. *Techniques for nuclear and particle physics experiments*. Berlin: Springer, 1994. DOI: 10.1007/978-3-642-57920-2. URL: https://cds.cern.ch/record/302344.

[33] M. Rongen. *Private communication*. 2025.

[34] A. G. Wright. *The Photomultiplier Handbook*. London, England: Oxford University Press, July 2017.

[35] IceCube Collaboration. *Acceptance Tests of more than 10 000 Photomultiplier Tubes for the multi-PMT Digital Optical Modules of the IceCube Upgrade*. 2024. arXiv: 2404.19589 [astro-ph.IM]. URL: https://arxiv.org/abs/2404.19589.

[36] L. Lin et al. "Work Function: Fundamentals, Measurement, Calculation, Engineering, and Applications". In: *Phys. Rev. Appl.* 19 (3 2023), p. 037001. DOI: 10.1103/PhysRevApplied.19.037001. URL: https://link.aps.org/doi/10.1103/PhysRevApplied.19.037001.

[37] N. Feigl. "Noise characterization and performance evaluation of new optical sensors for the IceCube Upgrade". PhD thesis. Humboldt-Universität zu Berlin, 2025.

[38] B. Povh et al. "Stabilität der Kerne". In: *Teilchen und Kerne: Eine Einführung in die physikalischen Konzepte*. Berlin, Heidelberg: Springer Berlin Heidelberg, 2014. ISBN: 978-3-642-37822-5. DOI: 10.1007/978-3-642-37822-5_3. URL: https://doi.org/10.1007/978-3-642-37822-5_3.

[39] J. Pradler, B. Singh, and I. Yavin. "On an unverified nuclear decay and its role in the DAMA experiment". In: *Physics Letters B* 720 (Oct. 2012). DOI: 10.1016/j.physletb.2013.02.033.

[40] M. Unland. "Studies on dark rates induced by radioactive decays of the multi-PMT digital optical module for future IceCube extensions". Master's Thesis. Westfälische Wilhelms-Universität Münster, 2017. URL: https://www.uni-muenster.de/imperia/md/content/physik_kp/agkappes/abschlussarbeiten/masterarbeiten/1712-ma_munland.pdf.

[41] M. Dittmer. "Characterisation of scintillation light induced by radioactive excitation in the mDOM glass pressure vessel". Master's Thesis. Westfälische Wilhelms-Universität Münster, 2020. URL: https://www.uni-muenster.de/imperia/md/content/physik_kp/agkappes/abschlussarbeiten/masterarbeiten/dittmer.pdf.

[42] E.H. Bellamy et al. "Absolute calibration and monitoring of a spectrometric channel using a photomultiplier". In: *Nuclear Instruments and Methods in Physics Research Section A: Accelerators, Spectrometers, Detectors and Associated Equipment* 339.3 (1994), pp. 468–476. ISSN: 0168-9002. DOI: https://doi.org/10.1016/0168-9002(94)90183-X. URL: https://www.sciencedirect.com/science/article/pii/016890029490183X.

[43] IceCube Collaboration. "In-situ calibration of the single-photoelectron charge response of the IceCube photomultiplier tubes". In: *Journal of Instrumentation* 15.06 (June 2020), P06032–P06032. ISSN: 1748-0221. DOI: 10.1088/1748-0221/15/06/p06032. URL: http://dx.doi.org/10.1088/1748-0221/15/06/P06032.

[44] Yt. Wei, My. Guan, Wx. Xiong, et al. "Consistency test of PMT SPE spectrum from dark-noise pulses and LED low-intensity light". In: *Radiation Detection Technology and Methods* 2 (2018), p. 11. DOI: 10.1007/s41605-018-0042-6. URL: https://doi.org/10.1007/s41605-018-0042-6.

[45] IceCube Collaboration. "The IceCube Neutrino Observatory: instrumentation and online systems". In: *Journal of Instrumentation* 12.03 (Mar. 2017), P03012–P03012. ISSN: 1748-0221. DOI: 10.1088/1748-0221/12/03/p03012. URL: http://dx.doi.org/10.1088/1748-0221/12/03/P03012.

[46] IceCube Collaboration. "In situ estimation of ice crystal properties at the South Pole using LED calibration data from the IceCube Neutrino Observatory". In: *The Cryosphere* 18.1 (2024), pp. 75–102. DOI: 10.5194/tc-18-75-2024. URL: https://tc.copernicus.org/articles/18/75/2024/.

[47] University of Wisconsin–Madison Physical Sciences Laboratory. *IceCube Gen1 Drill Project*. Accessed: 19.10.2025.

[48] IceCube Collaboration. "The design and performance of IceCube DeepCore". In: *Astroparticle Physics* 35.10 (May 2012), 615–624. ISSN: 0927-6505. DOI: 10.1016/

j . astropartphys . 2012 . 01 . 004. URL: http : / / dx . doi . org / 10 . 1016 / j . astropartphys.2012.01.004.

[49] IceCube Collaboration. "IceTop: The surface component of IceCube". In: *Nuclear Instruments and Methods in Physics Research Section A: Accelerators, Spectrometers, Detectors and Associated Equipment* 700 (Feb. 2013), 188–220. ISSN: 0168-9002. DOI: 10.1016/j.nima.2012.10.067. URL: http://dx.doi.org/10.1016/j.nima.2012.10.067.

[50] IceCube Collaboration. *Physics potential of the IceCube Upgrade for atmospheric neutrino oscillations*. 2025. arXiv: 2509.13066 [hep-ex]. URL: https://arxiv.org/abs/2509.13066.

[51] P. Eller et al. *Sensitivity of the IceCube Upgrade to Atmospheric Neutrino Oscillations*. 2023. arXiv: 2307.15295 [astro-ph.HE]. URL: https://arxiv.org/abs/2307.15295.

[52] IceCube Collaboration. "Design and Performance of the mDOM Mainboard for the IceCube Upgrade". In: *PoS* ICRC2023 (2023), p. 967. DOI: 10.22323/1.444.0967.

[53] IceCube Collaboration. *mDOM - Design, Status, and Notes (DSN)*. IceCube internal presentation.

[54] T. Anderson et al. *Design and performance of the multi-PMT optical module for IceCube Upgrade*. 2021. arXiv: 2107.11383 [astro-ph.IM]. URL: https://arxiv.org/abs/2107.11383.

[55] J. Schneider. "Characterization of the mDOM light detection and signal processing system for the IceCube Upgrade". Accessed: 26.10.2025. PhD thesis. Friedrich-Alexander-Universität Erlangen-Nürnberg (FAU), 2024. URL: https://open.fau.de/items/75c314f9-82b0-4952-873f-b8daab771ed9.

[56] IceCube Collaboration. *Upgrade MCU mDOM Python-Iceboot Interface*. IceCube Internal, Accessed: 27.11.2025. URL: https://wiki.icecube.wisc.edu/index.php/Upgrade_MCU_mDOM_Python-Iceboot_Interface.

[57] S. Blot and K.-H. Sulanke. *Private communication*. 2025.

[58] S. Blot. *Private communication*. 2025.

[59] K. Sulanke and M. Kossatz. *mini_Fieldhub Status*. 2019. URL: https://www.zeuthen.desy.de/~sulanke/Projects/ICECUBE/mini_Fieldhub/presentation/mini_fieldhub_201908_KS.pdf.

[60] A. Wohlfahrt. *Idea via private communication*. 2025.

[61] S. Mechbal et al. *T-mDOM*. Private GitHub repository. 2025. URL: https://github.com/WIPACrepo/T-mDOM.

[62] IceCube Collaboration. "Energy reconstruction methods in the IceCube neutrino telescope". In: *Journal of Instrumentation* 9.03 (Mar. 2014), P03009–P03009. ISSN: 1748-0221. DOI: 10.1088/1748-0221/9/03/p03009. URL: http://dx.doi.org/10.1088/1748-0221/9/03/P03009.

[63] IceCube Collaboration. *FAT - Interactive Plots*. IceCube internal. URL: https://convey.icecube.wisc.edu/data/exp/IceCubeUpgrade/commissioning/mDOM_FAT/summary_interactive2/run_205/mDOM_D115_v1.html.

[64] Wolfram Research. *Full Width at Half Maximum*. MathWorld. [Accessed: 25.01.2025]. n.d. URL: https://mathworld.wolfram.com/FullWidthatHalfMaximum.html.

[65] IceCube Collaboration. *mDOM PMT ERD*. IceCube internal document (Sharepoint).

[66] L. Halve. *PMT TACO*. 2020.

[67] A. Kristia. *Understanding the Convolution of a Gaussian with a Probit Model*. https://agustinus.kristia.de/blog/conv-probit/. Accessed: 28.07.2025. 2021.

[68] S. Baker and R. D. Cousins. "Clarification of the use of CHI-square and likelihood functions in fits to histograms". In: *Nuclear Instruments and Methods in Physics Research* 221.2 (1984), pp. 437–442. ISSN: 0167-5087. DOI: https://doi.org/10.1016/0167-5087(84)90016-4. URL: https://www.sciencedirect.com/science/article/pii/0167508784900164.

[69] G. Cowan. *Statistical Data Analysis*. Oxford, England: Clarendon Press, Mar. 1998.

[70] S. Axani. *Private communication*. 2025.

[71] D. W. Scott. "Scott's rule". In: *WIREs Computational Statistics* 2.4 (2010), pp. 497–502. DOI: https://doi.org/10.1002/wics.103. eprint: https://wires.onlinelibrary.wiley.com/doi/pdf/10.1002/wics.103. URL: https://wires.onlinelibrary.wiley.com/doi/abs/10.1002/wics.103.

[72] P. B. Price et al. "Temperature profile for glacial ice at the South Pole: Implications for life in a nearby subglacial lake". In: *Proceedings of the National Academy of Sciences* 99.12 (June 2002), 7844–7847. ISSN: 1091-6490. DOI: 10.1073/pnas.082238999. URL: http://dx.doi.org/10.1073/pnas.082238999.

[73] M. A. Unland Elorrieta. "Development, simulation, and characterisation of a novel multi-PMT optical module for IceCube Upgrade with emphasis on detailed understanding of photomultiplier performance parameters". PhD thesis. WWU Münster, 2023.

[74] C. Klein. *Refining the Discriminator Threshold Calibration Routine for IceCube Upgrade mDOMs*. DESY Summer Student project. 2024.

[75] D. Casadei. "Estimating the selection efficiency". In: *Journal of Instrumentation* 7.08 (Aug. 2012), P08021–P08021. ISSN: 1748-0221. DOI: 10.1088/1748-0221/7/08/p08021. URL: http://dx.doi.org/10.1088/1748-0221/7/08/P08021.

[76] S. Blot, M. Rongen, and L. Fischer. *Using mDOM flashers for the mDOM FAT - SPE Update*. Internal communication. IceCube internal document. 2020.

[77] Hamamatsu Photonics K.K. *Photomultiplier Tube R12199*. "Accessed: 23.11.2025". URL: https://hamamatsu.su/files/uploads/pdf/1___/$\mu\mu\mu\mu$_/μ/r12199_tpmh1356e.pdf.

[78] In: *The Concise Encyclopedia of Statistics*. Springer New York, 336–337. ISBN: 9780387328331. DOI: 10.1007/978-0-387-32833-1_250. URL: http://dx.doi.org/10.1007/978-0-387-32833-1_250.

[79] Nautilus MARINE SERVICE GmbH. *Vitrovex - Deep sea floatation and instrument housings*. https://www.esonetyellowpages.com/datasheets/datasheet-h432_1257883845.pdf. Accessed: 24.09.2025.

[80] L. D. Brown, T. T. Cai, and A. DasGupta. "Interval Estimation for a Binomial Proportion". In: *Statistical Science* 16.2 (2001), pp. 101 –133. DOI: 10.1214/ss/1009213286. URL: https://doi.org/10.1214/ss/1009213286.

[81] M. I. Jordan and K. McLoughlin. *Lecture 7: Jeffreys Priors and Reference Priors*. https://people.eecs.berkeley.edu/~jordan/courses/260-spring10/lectures/lecture7.pdf. Stat260: Bayesian Modeling and Inference, University of California, Berkeley; February 17, 2010. 2010.

[82] K.-H. Sulanke. *Private communication*. 2025.

Acknowledgments

I want to thank Claudio Kopper for giving me the opportunity to join his group for the course of this Masters thesis. Thanks to his support, I was able to attend the IceCube Collaboration meeting in Uppsala. This experience provided valuable insight into life as a researcher in a large collaboration. In addition, I am grateful that Claudio made it possible for me to spend a couple of weeks working in person at DESY Zeuthen.

Many thanks to Summer Blot for the supervision of both my DESY Summer Student project and my Masters thesis. I am thankful for the excellent guidance and support she offered at any time, whether in person or remotely. Her extensive knowledge helped me to continuously deepen my understanding of the mDOM system and the bigger picture of the IceCube Upgrade.

I would also like to thank Martin Rongen for his support and valuable advice throughout the last year. I am grateful that he took the time to proofread my entire thesis. His vast expertise significantly improved the quality of my work.

Writing a thesis without amazing office mates is possible, but pointless. Therefore, I am thankful that I did indeed have amazing colleagues who supported me at any time, answered questions and established frequent tea breaks. Thus, many thanks to every member of the Erlangen Tea Party (ETAP) Office[1]: Anna Bucket, Anke Moosbruger, Oliver Yannick, Lukas Henning and Andrei Kubarov.

Many thanks to everyone else in Erlangen and Zeuthen who helped make this thesis possible, either by technical or emotional support[2]. I am grateful for all of you who made the past year such an enjoyable experience.

Last but not least, I would like to thank my whole family for always being there for me. Without them, I would never have come so far.

[1] The order of the names was generated randomly. All of the names mentioned are spelled correctly, as this thesis was definitely written by Karolin Clein.

[2] Special thanks to Simon Köppel at this point.

Declaration of Originality

I, Carolin Annika Klein, hereby confirm that I wrote this thesis by myself. Artificial intelligence in form of DeepL and ChatGPT was used in the following way:

- AI was used to improve the style and readability of this thesis. This includes corrections of grammar and spelling. AI was not used to generate full text passages or change the content of the text.
- AI was used to improve and verify the functionality of some code that was written in the scope of this thesis. Code snippets that were generated by AI were reviewed carefully before usage.

I confirm that I only used the indicated sources and tools.

Place, Date

Signature